



In-Hand Pose Estimation Through Purely Tactile Perception and In-Hand Manipulation

A Master Thesis

written by

Victor Melbye Staven
vista17@student.sdu.dk

The code for this project is available at
https://github.com/vmstavens/in_hand_pose_estimation

University of Southern Denmark
The Technical Faculty

Word Count : 962
May 27, 2023

Abstract

Some abstract text explaining the goal, methods and conclusion of the project.

Contents

Acknowledgments	iii
Acronyms and Terms	iv
1 Introduction	1
1.1 Context	1
1.2 Problem Description	1
1.3 Thesis Overview	3
2 System Setup	5
2.1 Simulation Setup	5
2.2 Software Setup	7
2.2.1 Provided Software	7
2.2.2 Produced Software	9
3 State of the Art	10
3.1 Problem 1 - Tactile Perception	10
3.2 Problem 2 - Pose Estimation	12
3.3 Problem 3 - In-Hand Manipulation	14
4 Modeling	16
5 Tactile Perception	20
5.1 Methods	20
5.1.1 Recursive Least Squares	20
5.1.2 Network Architecture	22
5.1.3 Network Training Procedure	22
5.2 Experimental Setup	24
5.2.1 Contact Normal Estimation	24
5.2.2 Skew Force Estimation	25
5.3 Results	26
5.3.1 Contact Normals	26
5.3.2 Skew Forces	26
5.3.3 Physics Engine Comparison	29
5.4 Discussion & Conclusion	31
6 Pose Estimation	32
6.1 Problem	32
6.2 Method	34
6.2.1 Graduated Non-Convexity	34
6.2.2 Relaxed Convex Quadratic Programming	36
6.3 Experimental Setup	38
6.4 Results	40
6.4.1 Pose Estimation Performance Data	40
6.4.2 Weight Convergence Data	41

6.5	Discussion & Conclusion	44
7	In-Hand Manipulation	45
7.1	Method	45
7.1.1	Demo Augmented Policy Gradient	45
7.1.2	Data Collection Procedure	46
7.2	Experimental Setup	47
7.3	Results	47
7.4	Discussion & Conclusion	48
8	Discussion	49
9	Conclusion	50
A	Shadow Dexterous Hand - Technical Specifications	61
B	Tactile Perception - Simulated Electrode Activations	63
C	Pose Estimation Weight Convergence	65

Acknowledgements

I would like to express my sincere gratitude to those who have supported and guided me throughout my thesis project.

First and foremost, I would like to extend my deepest appreciation to my thesis supervisor, Christoffer Sloth, Lector at SDU Robotics, for his exceptional guidance and support throughout the entire process. His expertise and knowledge in the field of robotics have been invaluable in shaping this project.

I would also like to thank Yitaek Kim for his invaluable support and sparring in solving key aspects of this project. His insights and advice have been critical to the successful completion of this thesis.

Furthermore, I would like to extend my thanks to Shadow Robotics for providing the underlying software for the project to build upon along with technical support, enabling this project. Their contribution has been essential in the successful completion of this project.

Finally, I would like to thank my family and friends for their unwavering support and encouragement throughout this journey. Their love and support have been a constant source of motivation and inspiration.

Once again, I express my deepest gratitude to all those who have played a significant role in this project.

Acronyms

AEBM analytical elasticity-based models.	OMPL The Open Motion Planning Library.
AH Adroit Hand.	PC point cloud.
BR Black-Rangarajan.	PCR point cloud registration.
CAD Computer Aided Design.	PD Proportional-Derivative.
cGAN conditional Generative Adversarial Network.	PE pose estimation.
cobots collaborative robots.	PID Proportional-Integral-Derivative.
CP correspondence problem.	PnP pick-and-place.
CPD Coherent Point Drift.	PnP Perspective-n-Point.
CSGM Cross-Source Graph Matching.	PRM Probabilistic Roadmap Method.
CV computer vision.	PSD Positive Semidefinite.
DAPG Demo Augmented Policy Gradient.	PwoF point-contact-without-friction.
DeepGMR Deep Gaussian Mixture Registration.	QAP Quadratic Assignment Problem.
DL deep learning.	QCQP Quadratically Constrained Quadratic Programming.
DOF degrees of freedom.	QP Quadratic Programming.
EAA Equivalent Angle Axis.	RANSAC Random Sample Consensus.
EE end effector.	RCQP Relaxed Convex Quadratic Programming.
EFM elastic foundation models.	ReLU Rectified Linear Unit.
FEM finite element models.	RL Reinforcement Learning.
FGM Factorized Graph Matching.	RLS Recursive Least Squares.
FIM Fisher Information Matrix.	ROM Range of Motion.
FMT Fast Marching Tree.	ROS Robot Operating System.
FPFH Fast Point Feature Histograms.	RPY Roll-Pitch-Yaw.
GK grasp kinematics.	RRT Rapidly-exploring Random Tree.
GM Geman McClure.	SDH Shadow Dexterous Hand.
GMM Gaussian Mixture Model.	SDP Semi-Definite Programming.
GNC Graduated Non-Convexity.	SE Special Euclidean.
GT Ground Truth.	SF soft finger.
HF hard finger.	SLSQP Sequential Least-Squares Quadratic Programming.
ICP Iterative Closest Point.	SOCP Second Order Cone Programming.
IEP Inverse Elasticity Problem.	TCP Tool Center Point.
IHM In-Hand Manipulation.	TLS Truncated Least Squares.
IL Imitation Learning.	TP Tactile Perception.
JRMPC Joint Registration of Multiple Point Sets.	TSV Task Space Vector.
MIM Matrix Inversion Method.	UR Universal Robots.
ML machine learning.	
MLP Multi Layered Perceptron.	
NPG Natural Policy Gradient.	

Terms

collaborative robots (cobots) are robots which facilitate human-robot collaboration [1].

computer vision (CV) is a field of artificial intelligence (AI) that enables computers and systems to derive meaningful information from digital images, videos and other visual inputs - and take actions or make recommen-

dations based on that information [2].

correspondence problem (CP) is the problem where one aims at finding correspondences between the pixels in two (or more) images [3].

deep learning (DL) are methods that allow computational models that are composed of multiple processing layers to learn representations of data with multiple levels of abstraction [4].

end effector (EE) is a generic term for all functional units involved in direct interaction of the robot system with the environment or with a given object [5].

manipulator : A serial robot mechanisms. The robot manipulator is represented by a serial chain of rigid bodies, called robot segments, connected by joints [6].

point cloud registration (PCR) is a generic term for all functional units involved in direct interaction of the robot system with the environment or with a given object [5].

pose estimation (PE) A particular instance of feature-based alignment, which occurs very often, is estimating an object's 3D pose from a set of 2D point projections. This pose estimation problem is also known as extrinsic calibration [7].

Robot Operating System (ROS) is a set of open-source software libraries and tools that help build robot applications. [8].

Chapter 1

Introduction

1.1 Context

As of 2022 most of the industrialized world has developed tools for unprecedented growth in wealth and technology on a global scale [9, Chapter 4]. In such times a great deal of consumerism and interconnection is present with people needing products produced faster and more consistently than ever before [9, Chapter 4]. As one would expect, this creates a high demand for manufacturers to reliably and consistently provide products, while also remaining flexible as the demand for different product change rapidly. To accommodate the need for ever-greater volumes of products, consistent, reliable and flexible labor is essential in assembly, transport and manipulation processes in the production pipeline. Due to these types of manual labor being largely done by unskilled workers, automation alternatives are being adopted which provide benefits [9, Chapter 4]. This different approach to manufacturing has been labeled the fourth industrial revolution or i4.0 for short. The beneficiaries are the employer and employee, with the employer having the benefits: Avoid paying monthly salaries to unskilled laborers doing manual tasks, here the automation alternative only requires electrical energy and potential supervision by a few qualified individuals. Potential risks are also involved when hiring humans as the workforce can be inconsistent due to human error [10] or left out due to illness etc. Considerations about workers' rights such as working conditions and wages also need not be considered. Workers furthermore cause production limitations in the form of stand-still hours, such as bathroom and lunch breaks along with after-work hours and holidays. This replacement of manual labor also potentially benefits the employee, as boring and physically wearing work is automated, enabling the employees to take on different and less wearing and potentially dangerous roles. While the issue of labor unemployment becomes apparent solutions that provide support to already hired workers have been developed, such as collaborative robots (cobots) [11] which would negate this problem.

When implementing automation of production lines using robotics, certain categories of problems are revealed. These include assembly, alteration and pick-and-place (PNP), the last being the one of interest in this project.

1.2 Problem Description

Pick-and-place manipulators are used in a wide variety of different fields such as sorting of waste [12] handling of food [13, 14] and factory bin picking [15, 16, 17]. The solutions in these industries are examples of subcategories under the PNP problem, namely sorting and bin picking. Since both of these are subcategories of the PNP problem, they fundamentally follow the same sequential four phases from start to end. These phases are pre-grasping, grasping, transport, and placement [16] for traditional implementations of the PNP pipeline. The pre-grasp phase involves localizing the object(s), potentially estimating their pose and executing the trajectory to move the end effector (EE) grasp, collision-free to said object(s). Here different potential grasps can be considered to determine the best pose for the EE. In the grasping phase, the EE grasps the object in such a manner that the object's entire weight is supported by the EE, and ends when the object no longer is in contact with the environment, which often is the container holding the object. The transportation phase involves the motion of the manipulator to move from the pose achieved after the grasping phase, to a pose ready for placement of the object in the desired placing area or fixture. Here considerations may be needed about how much force and torque the EE's grasp can tolerate while moving without losing the object. Finally, the goal of the placing phase is to place the object within the placing

area or fixture in a desired end pose. Here the constraints on the end pose might differ significantly based on the application, as the pose of greens in a crate might need less precision than if the manipulator hands a bolt to another robotics system in the pipeline.

While these phases make up a traditional PNP system, certain assumptions are made regarding the objects of interest for this pipeline to function. Specifically, the localization and pose estimation (PE) of the pre-grasp phase are assumed possible due to either ensured object poses or estimated poses through computer vision (CV) sensory system. Due to CV being a mature research field a wide range of solution proposals to these problems have been generated [18]. These include classic vision [19, 20], deep learning (DL) based [21] and combinations of these [22]. However, while these may be sufficient for certain tasks they fundamentally suffer from the weaknesses introduced by vision techniques. These are a great number of outliers caused by: occlusions, reflecting, transparent or homogeneous surfaces, and repetitive structures when solving the correspondence problem (CP). Within factory settings, the common ones are transparent and reflective objects, due to metallic, plastic and glass products often being the materials used. While DL solutions have been developed for both reflective [23] and transparent [24] objects, these are use case specific and show limited results in a wider range of applications.

This project suggests a different PNP pipeline for cases where the object's starting pose is unknown. In this PNP pipeline the PE is moved from the pre-grasping phase to a new phase between the grasping and transportation phase, called the PE phase. The specific goal of this project is to develop a solution to this phase using tactile sensors in the EE to determine the object's pose. By using tactile sensing rather than visual the problems presented above will be eliminated. This will be done using a humanoid gripper as the EE with tactile sensors in each finger, more specifically a Shadow Dexterous Hand (SDH) [25] with 24 joints and 20 degrees of freedom (DOF).

The alternative pipeline this project will enable can be seen in the upper row of Fig. 1.1 compared to the traditional pipeline in the lower row.

In Fig. 1.1(a) the pre-grasping phase can be seen for both pipelines. Here the traditional pipeline in cases of multiple objects often will employ custom fingertips or grippers entirely to facilitate form closure grasps, due to the grippers not having the flexibility to perform reliable force closure. On the contrary force closure can be performed with a humanoid gripper on a wide range of objects with no need for changing gripper equipment.

In Fig. 1.1(b) the grasping phase can be seen which introduces a greater level of complexity when using the suggested pipeline due to the humanoid gripper being a more complex physical system to represent and control. This is compared to the simplicity of executing potential binary commands in the traditional pipeline e.g. open and close.

In Fig. 1.1(c) the transportation phase can be seen, which introduces one of the benefits of using the suggested pipeline. Here tactile sensors in a humanoid gripper can pose and estimate the object and manipulations can be performed to change the object's pose such that easier placement can be performed in the following phase. This form of object manipulation is not feasible for the simple pneumatic grippers used in a traditional pipeline.

In Fig. 1.1(d) the placement phase can be seen, which demonstrates the result of the previous phase, as the traditional pipeline now has to change the grip on the object to properly place it in the socket, while the humanoid gripper simply can insert the part, as it is already oriented properly.

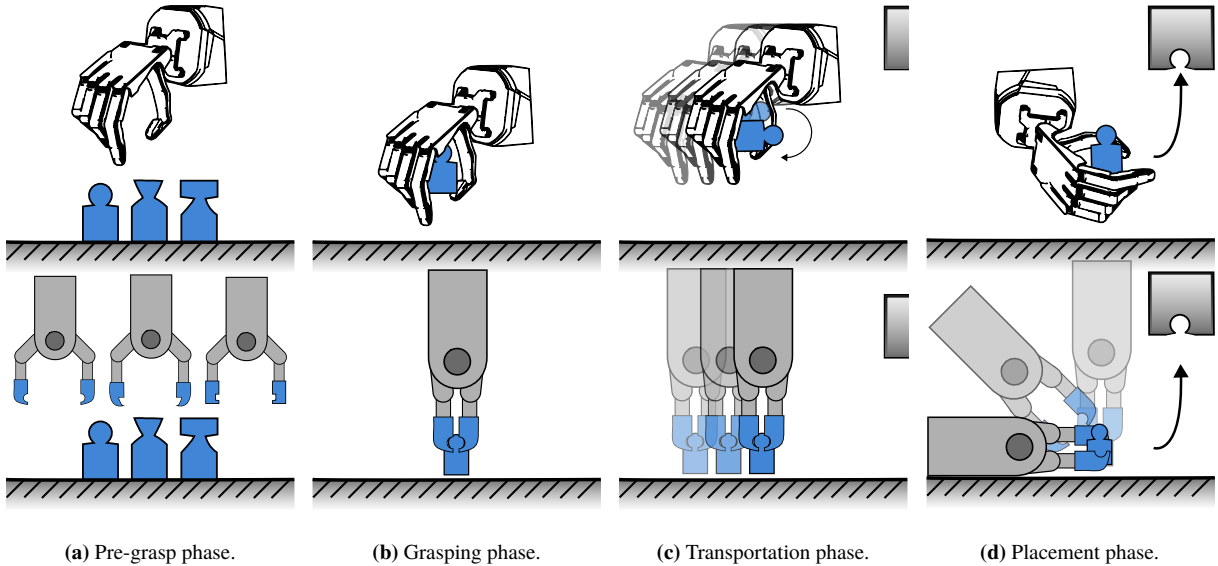


Fig. 1.1: A comparison between the traditional and suggested PNP pipeline.

To solve this PE problem, three sub-problems are identified and labeled problems 1, 2 and 3.

Problem 1 involves modeling the contact between the gripper's tactile sensors and the object, also referred to as tactile perception.

Problem 2 is to convert the collected data from problem 1 to estimated pose candidates.

Problem 3 involves in-hand manipulation. Since the initial grasp of the object might not be oriented in a manner where the recognizable features make context with the tactile sensors, manipulating the object within the EE's grasp will enable further information gathering. Thus the final problem is to control the EE in such a manner that the tactile sensors make context with the object in intelligently decided areas for a better pose estimate.

To test if the developed system successfully solves the PE problem, it is hypothesized that the intelligent probing method provides a statistically significant faster average PE convergence, along with a statistically significant greater success rate when determining the correct pose. A correct pose is here defined as a pose with an angle error less than 5° and a positional error less than 1 cm. This hypothesis will be referred to as H_1 , while the null hypothesis H_0 being that there is no statistically significant difference between intelligent and random probing's PE performance as described above.

1.3 Thesis Overview

This project is composed of 9 chapters, each listed below with an associated description.

Chapter 1: The introduction presents the historical context of the project along with a problem description and thesis overview. The problem description contains the decomposition of the project into sub-problems which will be addressed in the following chapters.

Chapter 2: The system setup presents an overview of the practical details of the project in the form of the system setup along with the code developed to execute the project.

Chapter 3: The literature review addresses the three problems identified in Chapter 1 by providing a thorough literature review on older as well as newer methods for solving each of the identified problems. To end each section, groups are compared and a method is chosen among the ones presented.

Chapter 4: The modeling chapter presents the physical modeling of the system and defines important mathematical notations and quantities as used in the following chapters.

Chapter 5: The Tactile Perception (TP) chapter addresses the method chosen in Chapter 3 to solve the first problem. This chapter expands on the method chosen and its functionality, followed by an evaluation of said method through experiments and their results. Finally, the functionality of the method is concluded.

Chapter 6: The PE chapter addresses the method chosen in Chapter 3 to solve the second problem. This chapter follows the same structure as Chapter 5.

Chapter 7: The In-Hand Manipulation (IHM) chapter addresses the method chosen in Chapter 3 to solve the third problem. This chapter follows the same structure as Chapter 5 and Chapter 6.

Chapter 8: The discussion chapter goes over the combined system and addresses problems, improvements, shortcomings and potential for future development.

Chapter 9: The conclusion chapter addresses the success of the project.

Chapter 2

System Setup

The SDH [25] is a sophisticated robotic hand with a wide range of sensory feedback capabilities. To develop and test algorithms for this complex system, simulation is an invaluable tool. In this chapter, the practical setup of the project is presented, which involves simulating the SDH within the dynamic simulator, Gazebo [26].

This simulation is based on the Shadow Robot Company's [27] Robot Operating System (ROS) [8] packages [28], which provide a flexible and customizable framework for controlling the hand. This project uses Gazebo, a popular robot simulation environment, to simulate the physics of the hand and its interaction with the environment. To ensure reproducibility and portability, the development framework which encapsulates the simulation environment is built within a Docker container, which allows for easily distributing the code and dependencies to other researchers. Simulating the system additionally enables Ground Truth (GT) values to be easily available, and safety is less of a concern, as a broken simulated hand, and additional equipment including sensors cost are potentially easier available in the form of simulated sensor inputs.

This simulation is based on the ROS packages developed by the Shadow Robot Company [27, 8, 28]. These packages offer a flexible and customizable framework for controlling the hand. The simulation utilizes Gazebo, a widely-used robot simulation environment, to accurately model the hand's physics and its interactions with the environment. To ensure reproducibility and ease of distribution, the development framework, including the simulation environment, is encapsulated within a Docker container. This containerized approach allows for seamless sharing of the code and its dependencies with other researchers, promoting collaboration and portability.

Simulating the system provides the added benefit of readily accessible GT values, ensuring accurate analysis and evaluation of algorithms. Moreover, safety concerns are mitigated in the simulation as the risk of damaging physical hardware or incurring additional costs for equipment and sensors is eliminated. Instead, these aspects can be readily simulated through virtual sensor inputs and virtual components.

In this chapter, a detailed description of the hardware and software used in this project's simulation setup is provided, which includes the software architecture of the simulation, including the ROS packages and Gazebo setup.

2.1 Simulation Setup

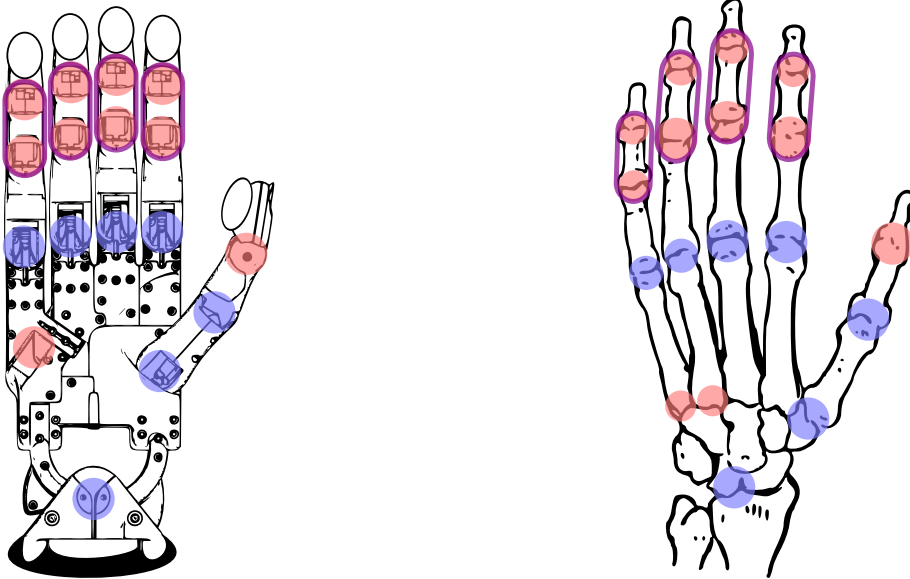
The Computer Aided Design (CAD) model of the SDH is a highly detailed and accurate representation of the physical hand. The model is based on the original design of the real-world hand, which was developed by the Shadow Robot Company. The CAD model includes precise geometry for all of the hand's components, including the finger joints, tendons, and simple tactile sensors. The model also includes detailed material properties for each component, which are used to simulate the hand's physical behavior in the simulation.

The SDH's joints are labeled based on joint location according to Appendix A.3 and placement from the fingertip i.e. the outermost joint on the middle finger is labeled MF1 while the innermost is MF4. The wrist joints are labeled WR1 and WR2, where WR1 is responsible for the hand's yaw and WR2 is responsible for the hand's pitch rotation.

The structure of the hand can be seen in Fig. 2.1(a) compared to a human hand in Fig. 2.1(b). Here each joint is marked with a color, labeling the DOF for that particular joint. The red labels refer to joints with 1 DOF, blue refers to joints with a DOF equal to 2 and purple refers to two joints that are coupled. The coupling between joints is such that, a flexion of joint 1 imposes a constraint on joint 2. If joint 1 exceeds a certain angle, it enforces joint

2 to flex accordingly to maintain the established constraint. Both joints are mechanically linked to a single motor, functioning as a combined joint denoted as joint 0 for control purposes.

As seen here the SDH provides human-like dexterity due to its similar kinematics, see Fig. A.1, and the comparable Range of Motion (ROM) of each joint, see Table A.1 and Table A.2.



(a) SDH with joints color coded depending on the degrees of freedom. The total number of degrees of freedom can here be seen as 24. This figure is based on [29].

(b) SDH with joints color coded depending on the degrees of freedom. The total number of degrees of freedom can here be seen as 25 [30]. This figure is based on [31].

Fig. 2.1: The SDH and a human hand red here marks a joint with 1 degree of freedom, while blue marks a joint with 2.

The hand's geometry is modeled using a combination of standard shapes and custom-designed components. For example, the finger joints are modeled using a series of cylinders and spheres, which are connected by virtual tendons to simulate the motion of the real-world hand. The tactile sensors on the simulated hand, at the writing of this thesis, are purely aesthetical as representative simulated tactile sensors are yet to be supported as a standard component. To generate representative tactile data additional software is therefore required. The tactile sensors can be seen in Fig. 2.1(a) as the ellipsoids mounted at each fingertip.

Multiple hand configurations are available including a left hand, right hand, and both configurations mounted on Universal Robots (UR) manipulators [32]. The configuration chosen for this project is a Shadow Dexterous right hand without being mounted on a manipulator. Fig. 2.2 shows the CAD model of the SDH in simulation.

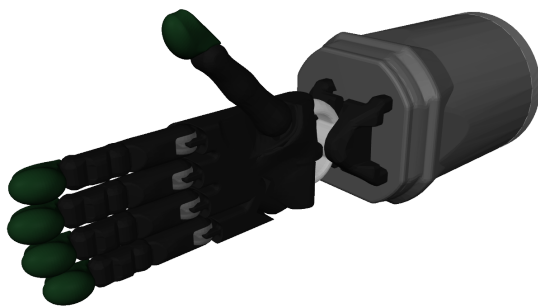


Fig. 2.2: A cutout of the simulated SDH.

2.2 Software Setup

The software for this project consists of two parts the software provided and the software produced.

2.2.1 Provided Software

The simulation environment is shipped in a custom Ubuntu-based docker container [33, 34] with the necessary libraries to communicate and develop applications on the simulated as well as the physical hand, wrapped within a catkin workspace [35]. Additionally, the container comes with common-use libraries for Python and C++ development in ROS including numpy[36], OpenCV [37] and `dynamic_reconfiguration` [38]. The development environment can be seen illustrated in Fig. 2.3. The communication between the provided ROS packages and the Gazebo simulator is achieved through the ROS-Gazebo framework.

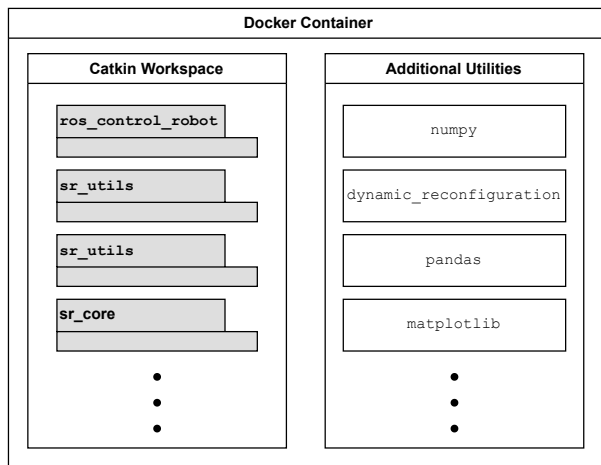


Fig. 2.3: The boxes marked with grey are ROS packages, while the white are modules.

When communicating with the SDH, the primary interface provided is the hand commander i.e. `SrHandCommander` which enables functionalities such as retrieving the current state of the hand, executing given path plans etc. To plan and execute a high-resolution path $\mathbf{Q}_{\text{full}} \in \mathbb{R}^{m \times 24}$, where m is the number of joint configurations and 24 is the number of joints in the hand, a sequence of waypoints \mathbf{Q} form a low-resolution path of $\mathbf{q}_i = [q_0, q_1, \dots, q_n]^T \in \mathbb{R}^{24}$ where $i \in \{0, 1, \dots, m_w\}$ with m_w being the number of waypoints. \mathbf{Q} can thus be written as

$$\mathbf{Q} = \begin{bmatrix} \mathbf{q}_1^T \\ \mathbf{q}_2^T \\ \vdots \\ \mathbf{q}_{m_w}^T \end{bmatrix} \in \mathbb{R}^{m_w \times 24}. \quad (2.1)$$

`SrHandCommander` parses the path to the `move_group` handled by MoveIt [39]. After receiving the plan, MoveIt first checks the validity of the start and goal states concerning the robot's joint limits, collision constraints, and other constraints like self-collision avoidance. This helps to ensure that the planned path is feasible and safe for the robot to execute. Once validated, the validated path $\mathbf{Q}_{\text{valid}} \in \mathbb{R}^{m_q \times 24}$ is parsed to The Open Motion Planning Library (OMPL) [40] where a safe high-resolution path is built using some chosen sample-based single- or multi-query path planning method. Some examples of these methods include Probabilistic Roadmap Method (PRM), Fast Marching Tree (FMT) and Rapidly-exploring Random Tree (RRT)-Connect, the last of which is the default used in the provided software and the one chosen for this project. To execute the path the development environment provides `SrJointPositionController` i.e. a joint space position controller by default, which is the one chosen for this project.

The controller is built using the `ros_control` [41] framework. The `ros_control` package provides a hardware-agnostic interface, to enable the same controllers on multiple different robotics platforms, along with the same controller being applicable on real hardware as well as simulated hardware. Finally, the hardware interface communicates with a 20 Proportional-Integral-Derivative (PID) controllers, one for each independent joint to ensure control. The software architecture for communicating with the robotic hand can be seen in Fig. 2.4, which was inspired by figures from [42, 43, 44].

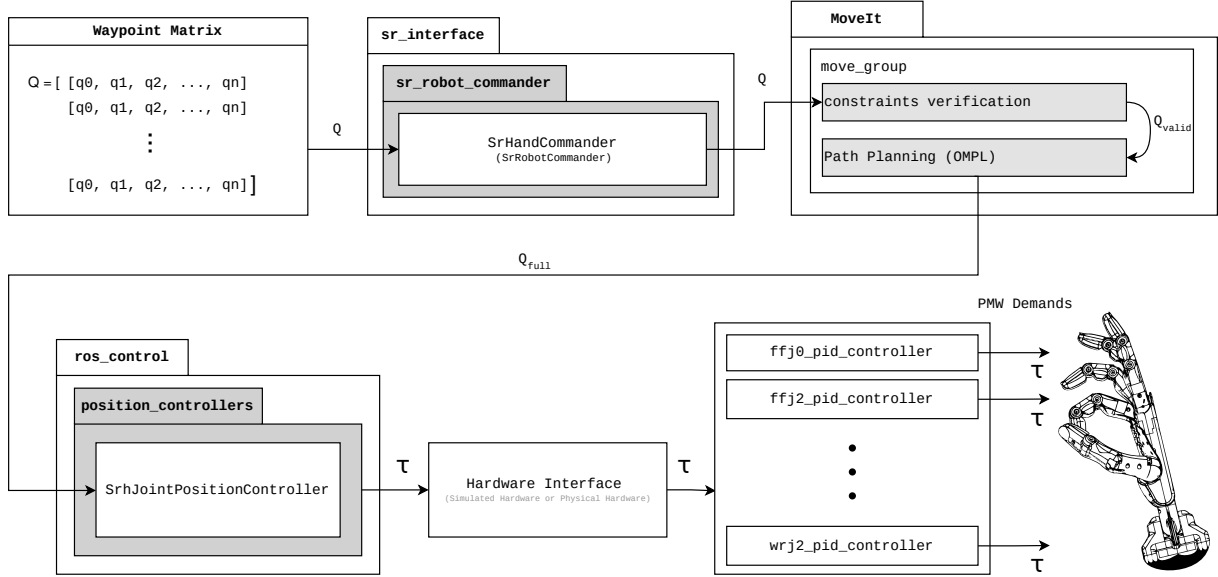


Fig. 2.4: Diagram showing the communication and control flow of interacting with the SDH.

When executing an example path Fig. 2.5 shows joint angles during execution on the simulated hand throughout 15 s. The path here consists of five waypoints for FFJ2 and FFJ3, whereas none is set for FFJ1. This is to demonstrate the coupling as FFJ1 still follows the motion of FFJ2 even though no motion is commanded.

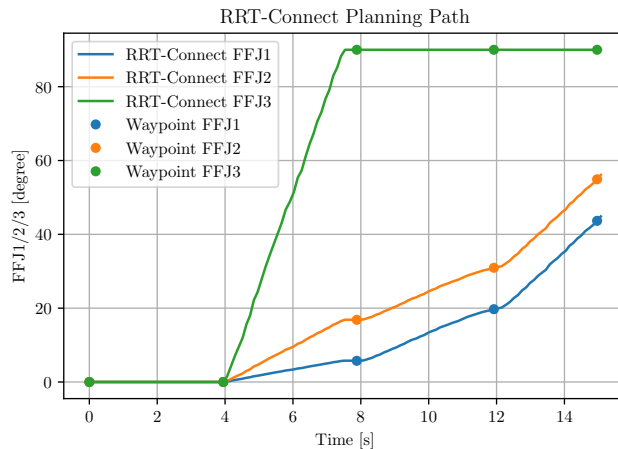


Fig. 2.5: Showing the joint trajectory of the first finger's joints FFJ1 to FFJ3, where the coupling between FFJ1 and FFJ2 is shown.

2.2.2 Produced Software

To execute this project, software was developed to communicate with and extract data from the simulated SDH. The software is structured semantically in a similar way as the hand itself, as a `ShadowHand` contains five fingers, each labeled as one of TH,FF,MF,RF or LF and a `ShadowWrist`. Each finger is equipped with a reader that samples the tactile data provided by Gazebo's physics engine at 100 Hz. This wrapper is written to an easy-to-use interface to the hand which provides reliable bookkeeping of sensor data. The structure can be seen illustrated in Fig. 2.6. This code is provided in a ROS package `shadow_hand` at [45]. Additionally, custom tools for easy launching and execution of experiments with live plotting of tactile data are provided with additional utilities such as base64 encoding and decoding at `ros_utils` [46].

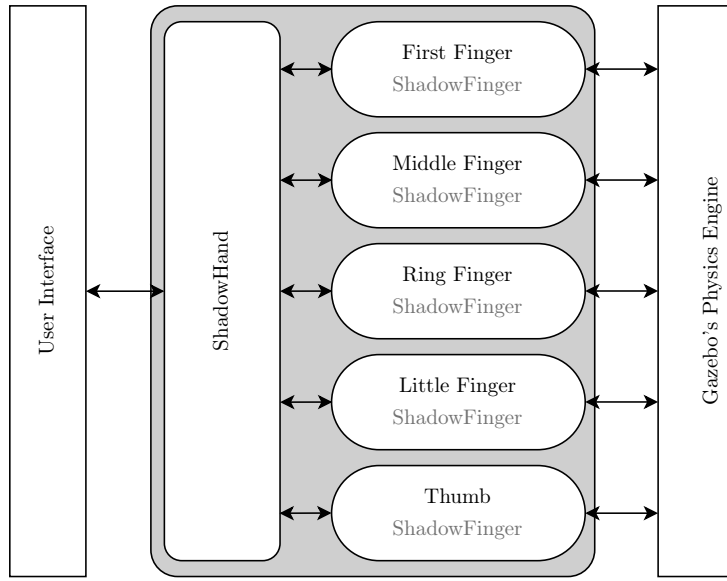


Fig. 2.6: Produced software architecture showing the wrapper and API structure.

Chapter 3

State of the Art

3.1 Problem 1 - Tactile Perception

Based on the contact model categories described in Chapter 4, the most representative was chosen to be soft finger (SF) models. Within the category of SF models, a method fit for this project's use case is to be chosen to solve problem 1. SF models can furthermore be divided up into three different categories: analytical elasticity-based models (AEBM), elastic foundation models (EFM), finite element models (FEM) [47] and machine learning (ML) models. The different categories can be seen organized in Fig. 3.1

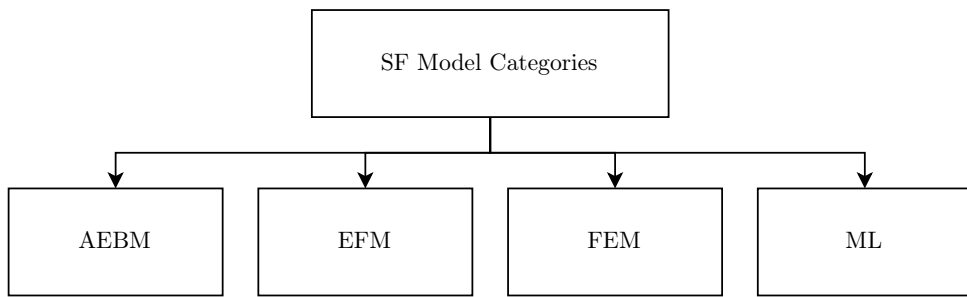


Fig. 3.1: Tree of methods for tactile perception.

AEBM are theoretical formulations of elastic contact areas and the stresses on both the surfaces and the sub-surfaces of the contacting bodies. The first of such models was introduced by Heinrich Rudolf Hertz in 1882 [48] and is still used for simple contact cases. In the formulation of the Hertzian contact model, two assumptions are made: Objects in contact are made of linear elastic materials and only small contact deformations occur compared to the dimension of an object. However, robotic EE fingertips are often made of non-linear elastic materials and for that reason, the Hertzian contact model does not represent the type of contact in this project [49, Chapter 37]. To improve on the Hertzian model, a more general formulation can be made which extends the model from linear to nonlinear elastic contacts [50, 51]. This power-law formulation subsumes the Hertzian contact theory while assuming a circular contact area. Other models have been proposed that combine the descriptions of both friction-contact and the shear-torsion as experienced by the bodies [52].

However, to more accurately describe the contacts involving robot fingers, viscoelastic soft contact model appear more relevant due to such fingers often being made of materials that show viscoelastic properties e.g., rubber, silicone and polymers. Simple models such as Kelvin-Voigt's [53] and Maxwell's [54] models describe the interaction between strain and stress as a spring-damper system in a serial or in a parallel configuration respectively. Models which expand on this idea describe the reacting force as the product of the temporal and the elastic response while incorporating previous stress responses [55]. To simplify this formulation alternatives have been developed to assume no past stress [56, 57, 58]. Upon these, more modern techniques have been developed which have seen use in similar use cases as the ones of interest in this project. One method attempts to expand the description of contacts between rigid indentors and elastic half-spaces, using the Matrix Inversion Method (MIM) as introduced by Kalker [59], to viscoelastic half-spaces as well. Assuming the surfaces are frictionless, the relationship is described in terms of the pressure distribution, the resultant force on the indenter and the penetration [60]. Attempts involving solutions to Boussinesq's problem for polynomial pressures acting over polygonal domains [61]

have also been developed and modernized by combining it with Cerruti's solution [62]. However due to numerical singularities being present, modifications are made to threshold the model. For a more complete description without singularities, Love's formulation has been added leading to a more accurate analytical representation but with the cost of an increased computational complexity [63]. For these Boussinesq-based approaches to be representative two assumptions are made 1) There exists a linear relationship between stress and strain, referred to as deformation, and 2) strains are infinitesimal [64, Chapter 6].

EFM are methods developed to build upon AEBM by allowing a simple discrete contact calculation in more general surface geometries. Here the deformable part of the contact is modeled as a layer over a rigid base with a series of discrete and independent springs in the contact normal. A widely used example of this method is Winkler's elastic foundation model [65], which has been used in structural engineering for modeling different properties of beams such as stability [66], vibrations and buckling [67]. Other EFM methods have shown accurate modeling performance when applied within the field of medical engineering. Here a comparative study between AEBM, EFM and FEM demonstrate the suggested modified EFM performs better than the alternatives in 3D knee models when predicting prosthetic knee performance [47]. A different method attempts to attain vivo contact pressure predictions for improved knee replacement designs [68] Within the field of robotics EFM have provided solutions to problems such as slip [52], compliance, sliding [69, 70], stiffness and contact mechanics [71] of anthropomorphic grippers. One such method derives friction constraints based on general expressions for non-planar contacts of elastic bodies, where the local geometry and structure of the objects in contact are taken into account. Using these, a linear complementary problem is formulated and solved, resulting in the normal and frictional forces applied at each contact, as well as the relative velocity of the bodies involved [72].

FEM are popular general tools for solving PDE [73] and have seen contact applications in a wide range of engineering disciplines due to the assumptions made in AEBM and EFM not being applicable in these cases. A great number of these cases exist within the manufacturing industry [74] whereas one example is the metal forming processes. Specifically, the estimation of wheel-rail profiles [75] has been addressed using FEM due to the estimation of contacts over a greater surface is needed than what is assumed in AEBM and EFM. Other applications such as quality control through sliding wear estimation [76], analysis of the responses of fully coupled thermo-elasto-plastic solids in contact [77] and performing diagnostics of failures in induction motors [78]. Due to the complexity of modeling the contacts within robotics, FEM have become a popular choice and enabled tactile applications such as cobots tactile skin for ensuring collaborative behavior when in contact [79], performance estimation of new tactile sensor technologies [80] and evaluating complex contact types by extending simulations and analysis systems [81]. The modeling complexity has furthermore inspired using FEM as ground truth results when synthesizing ML data in simulations for deep learning models, which has enabled execution speeds 75 times greater than simply evaluating FEM [82, 83, 84].

The use of these ML models has enabled realistic simulations of tactile sensor data. Current literature applies DL-based approaches to simulate tactile sensor data for various tasks [85, 86]. For instance, simulating realistic tactile images from simulated contact depth to bridging the reality gap for vision-based tactile sensing using a diffusion model [87]. Similarly, a conditional Generative Adversarial Network (cGAN) has been used to simulate realistic tactile sensory data for use in tactile tasks [87]. Solutions using DL models purely based on Multi Layered Perceptron (MLP) have been applied to enable real-time simulated realistic tactile data [88].

Given the methods presented above, the AEBM Boussinesq-Cerruti approach is considered along with the MLP based DL model.

Although the Boussinesq-Cerruti approach can produce precise tactile data and can be tailored to suit a particular case, it faces certain challenges. The model relies on certain assumptions regarding the materials in contact, including linear deformation and infinitesimal strains. Furthermore, evaluating the model requires complex calculations, such as multidimensional integrals, which significantly increase computation time and hinder real-time

performance. In contrast to the transparency offered by the Boussinesq-Cerruti approach, the MLP based approach is limited by the black-box nature of DL models. Despite this drawback, MLP based DL models offer several benefits, such as low execution time and high adaptability to complex systems. Due to the high adaptability and option for real-time performance, the DL model presented in [88] is chosen to solve the tactile perception problem i.e. problem 1.

3.2 Problem 2 - Pose Estimation

PE, which involves determining the position and orientation of an object in 3D space, has been the subject of many research studies. The literature has identified two main categories of methods for solving this problem: those based on DL, and those based on point cloud registration.

These can along with their subcategories be seen in Fig. 3.2 as inspired by [89].

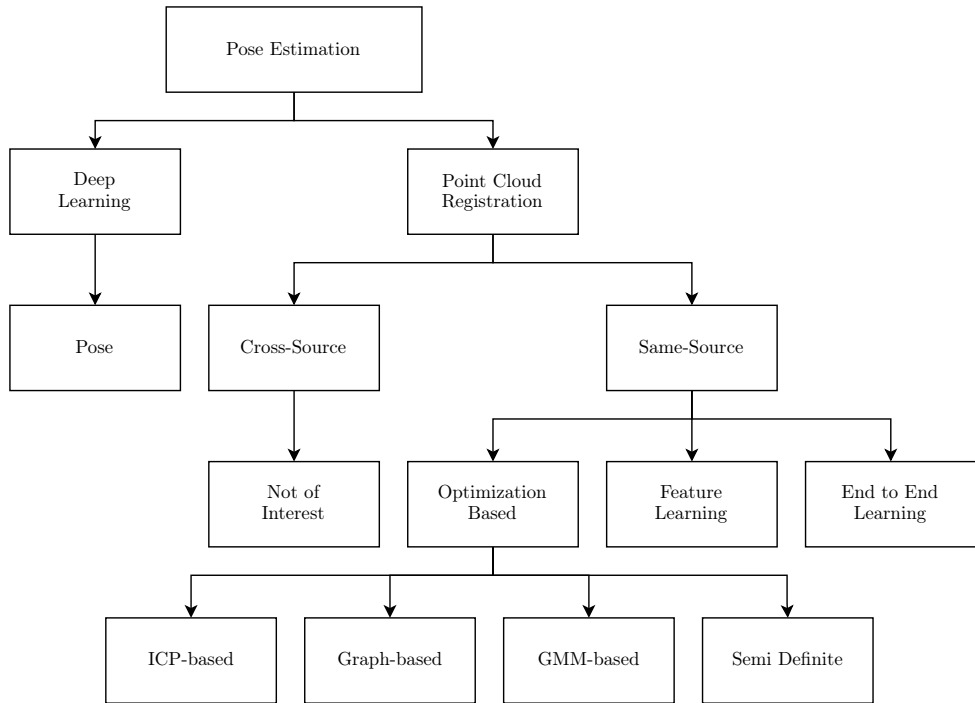


Fig. 3.2: Tree of methods for solving the point cloud registration problem. The categorization is inspired by [89].

Purely DL based methods learn feature representations of input data, often in the form of images, and use them to estimate the subject's pose. This is commonly done in the context of human pose estimation [90, 91, 92]. While these methods have shown extensive use in these cases, their applicability in this project is limited and thus excluded from consideration.

The other method group i.e. point cloud registration (PCR) methods are separated into two subgroups: cross-source and same-source point cloud (PC)s. Here cross-source refers to a PC produced by combining information from sensors of different kinds e.g. visual- and tactile sensors, while same-source methods only produce PCs based on information from the same kind of sensors e.g. only tactile sensors. While cross-source approaches have shown utility in an extensive range of applications [93, 94, 89] their applicability in this project is minimal, as purely tactile pose estimation is the problem of interest as presented in Chapter 1.

PCR methods from the same source data can be categorized into three sub-categories: end-to-end learning, feature-learning, and optimization-based methods. End-to-end learning-based methods use a neural network to estimate

the transformation matrix that aligns two point clouds. Proposed solutions include using neural networks for scene completion to estimate the relative pose between RGB-D scans [95], learning registration patterns as parametric functions through a scan completion module and pairwise matching module [96], and a fast feature-metric point cloud registration framework to minimize the feature-metric projection error without correspondences [97].

In contrast, feature-learning methods use deep neural networks to learn robust feature correspondence searches, which are then used in estimation algorithms such as Random Sample Consensus (RANSAC). In the literature, models have been developed to extract local geometric descriptors from RGB-D reconstructions [98], to learn globally informed 3D local feature descriptors [99], and to use siamese deep learning architectures with convolutional layers through a voxelized smoothed density value (SDV) representation [100].

Lastly, registration methods based on optimization are employed to estimate the transformation matrix through two stages: correspondence searching and transformation estimation. Their goal is to minimize a cost function that gauges the dissimilarity between two point clouds. Within this category, there are four sub-categories identified: Iterative Closest Point (ICP)-based, graph-based, Gaussian Mixture Model (GMM)-based, and semi-definite programming-based methods.

Since the original proposal in 1992 [101] using point-to-point correspondences, ICP-based methods have evolved and incorporated different types of correspondences to improve performance. Examples include point-to-plane [102] and plane-to-plane [103]. Modern approaches also employ complementary methods such as point cloud filtering, adaptive fireworks algorithms, and KD-Trees [104].

The main idea of graph-based registration methods is to use a non-parametric model [105]. In this method, correspondences between two graphs are found by considering both the vertices and edges, making it an optimization problem [105]. To solve this optimization problem, there are two categories of graph-matching methods based on the objective functions' constraints: second-order and high-order methods [106]. Second-order methods include Cross-Source Graph Matching (CSGM) [93], which uses a linear program to solve the graph-matching problem and apply it to solve the cross-source point cloud registration task, Factorized Graph Matching (FGM) [107] factorizes the large pairwise affinity matrix into smaller matrices and solves the graph-matching problem with a simple path-following optimization algorithm. Spectral graph [108] uses a spectral relaxation method to approximate the Quadratic Assignment Problem (QAP), and Semi-Definite Programming (SDP) relaxation is used to relax the non-convex constraint using a convex semi-definite. While higher-order graph matching provide methods for [109] design a probabilistic approach to solve the high-order graph-matching problem, while [110] design a triangle similarity and convert the graph-matching problem into a tensor optimization problem. More recent work, such as [111] suggests an elastic net to control the trade-off between the sparsity and accuracy of the matching results by incorporating the Elastic-Net constraint into the tensor-based graph matching mode.

GMM-based methods commonly tackle the point cloud registration problem by transforming it into a likelihood maximization problem for the input data. This has resulted in the development of several optimization strategies aimed at maximizing the likelihood and optimizing the transformation matrix. For instance, a motion drift idea was introduced into the GMM framework by [112] in the form of Coherent Point Drift (CPD) which imposes constraints on transformation estimation. In another approach,[113] combines GMM with the convex hull to reduce computation complexity. Furthermore, Joint Registration of Multiple Point Sets (JRMPC) [114] cast registration as a clustering problem where the transformation is optimized by solving the GMM. Recently, Deep Gaussian Mixture Registration (DeepGMR) [115] employed DL to learn the correspondences between GMM components and points, enabling the estimation of both the transformation and GMM parameters in a single forward step.

Lastly, within semidefinite programming different optimization groups exist, such as Second Order Cone Programming (SOCP), Quadratic Programming (QP) and Quadratically Constrained Quadratic Programming (QCQP). Due to the subject of interest being a rotation in $\text{SO}(3)$, the constraints of the rotation matrix, i.e. quadratic constraints,

must be respected. Because of this, the methods of QCQP are of interest. One such example provides estimates which are insensitive to a large fraction of spurious correspondences through decoupling the scale, rotation, and translation estimation. This decoupling enables the solving of these in cascade for the three transformations. The method is referred to as TEASER (Truncated least squares Estimation And SEmidefinite Relaxation), which solve large SDP relaxations, and additionally comes with a second fast and certifiable algorithm, named TEASER++. To decrease execution time this method uses Graduated Non-Convexity (GNC) to solve the rotation subproblem and applies Douglas-Rachford Splitting to enable efficiently certify global optimality [116]. Secondly, Invariant-based Highly Robust Point Cloud Registration (IRON) applies a similar methodology as to TEASER, but instead applies RANSIC (RANdom Samples with Invariant Compatibility) to robustly estimates the scale between two sets of point clouds [117]. Finally, Relaxed Convex Quadratic Programming (RCQP) formulates a QCQP problem with a full set of quadratic rotational constraints and obtains a Lagrangian dual relaxation, which empirically recovered a globally optimal solution in 100 % of the tested cases, although why strong relaxation seems to hold has yet to be shown [118].

Among the categories presented above, the ones of particular interest are optimization-based techniques due to their mature mathematical foundation and possible certifiable optimality and outlier rejection capabilities, and DL-based techniques due to their adaptability and low execution time. While DL-based methods can learn feature representations of point clouds and estimate the transformation between two point clouds, optimization-based approaches with outlier rejection can effectively handle noise and outliers in the data, which is a common problem within the PCR problem. Due to this, the chosen method is the optimization based RCQP method with GNC outlier rejection [119].

3.3 Problem 3 - In-Hand Manipulation

Motion planning is a critical aspect of robot applications as it involves finding a path without collisions between two configurations. However, when it comes to dexterous manipulation, where the object may not always be fully constrained, a more advanced approach called kinodynamic motion planning becomes necessary. Kinodynamic motion planning presents significant challenges, particularly in high-dimensional spaces, and is known to be PSPACE-hard [120], indicating its computational complexity.

To address these challenges, researchers have proposed probabilistic complete sampling-based kinodynamic motion planners like SST and SST* [121]. These planners utilize sampling-based techniques and probabilistic methods to generate collision-free paths in complex environments. Despite their effectiveness, the complexity of the motion planning problem has led to the integration of motion planning algorithms with model predictive control. By combining these two techniques, it becomes possible to avoid solving a boundary value problem [122], reducing the computational burden associated with kinodynamic motion planning.

Furthermore, to further enhance performance, researchers have explored the combination of kinodynamic motion planning algorithms with reinforcement learning. This integration leverages the capabilities of reinforcement learning algorithms to learn from experience and improve the efficiency and quality of the generated motion plans [123]. By incorporating the knowledge acquired through reinforcement learning, the kinodynamic motion planning process can adapt and optimize its solutions over time, resulting in more refined and effective paths for dexterous manipulation tasks.

Immitation Learning (IL) has additionally seen a rise in popularity as a Reinforcement Learning (RL) based dexterous manipulation method. One such example [124] applies

Overall, the field of motion planning has witnessed the development of various approaches to address the challenges posed by kinodynamic motion planning in high-dimensional spaces. From probabilistic complete sampling-based planners to the integration of model predictive control and reinforcement learning, these advancements aim to

enhance the efficiency, reliability, and adaptability of motion planning algorithms in order to support complex robot applications.

Chapter 4

Modeling

To model the contact between the EE's tactile sensors, eight different categories exist as identified in [125]. The three most common ones within the field of robotics [49, Chapter 37] are point-contact-without-friction (PwoF), hard finger (HF) and the SF model as shown in Fig. 4.1.

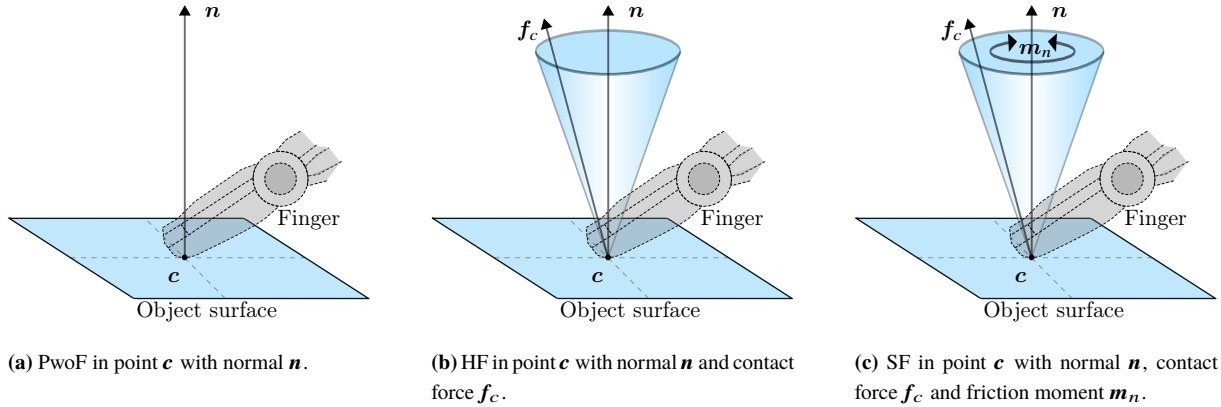


Fig. 4.1: The three most commonly used contact models.

The PwoF model, as shown in Fig. 4.1(a), can only represent forces along the surface normal $\mathbf{n} \in \mathbb{R}^3$ at the point of contact $\mathbf{c} \in \mathbb{R}^3$ and thus the model does not support surface deformations between the two contacting objects. This model is applied in cases where very little deformation is present, along with the contact having a friction coefficient approximately equal to zero [49, Chapter 38].

The HF model, as shown in Fig. 4.1(b), is representative when the friction between objects is significant, while the contact deformation is small enough to ignore friction moments and deformations [49, Chapter 38]. To model the friction acting on the contact point a great number of methods exist, a common one being the Coulomb friction with different modifications depending on the use case [126]. This model states that the frictional force acting on an object can be formulated as

$$f_f = f_N \mu, \quad (4.1)$$

with f_f being the magnitude of the Coulomb friction, f_N being the magnitude of the normal force in the point of contact and $\mu \in [0, 1]$ being the friction coefficient. One visualization of this linear relationship can be seen in the cones illustrated in Fig. 4.1(b) and Fig. 4.1(c). These cones are referred to as friction cones, which for a hard finger model can be formulated as

$$C_{f,\text{HF}} = \{ f_c \mid f_t \leq \mu f_z, \mu f_z \geq 0 \} \quad , \quad f_t = \sqrt{f_x^2 + f_y^2}. \quad (4.2)$$

Here f_c is the magnitude of the contact force and f_t is the magnitude of the tangential force. f_x , f_y and f_z are the magnitudes of the x , y and z components of the contact force ($f_c \in \mathbb{R}^3$) and μ is the friction coefficient [49, Chapter 37]. By applying a contact force that ensures the friction stays greater than the magnitude of the tangential force, neither object slips i.e. f_z must ensure that $f_z \mu$ stays greater than f_t for the objects not to slip. Visually this is the case when the contact force f_c stays within the friction cone, which enables a friction-based grasp type referred to as force closure. Specifically, force closure refers to when the composite wrench cone contains the entire wrench space so that any external wrench w_{ext} on the body can be balanced by contact forces [127]. A force that commonly contributes significantly to the external wrench, and thus to the tangential force, is gravity.

The SF model, as shown in Fig. 4.1(c), is used to represent scenarios where both friction and surface deformations are significant. Due to deformations of the finger, an additional torsional moment about the contact normal will be present [49, Chapter 38]. While an analytical formulation of the SF relation depends on the pressure distribution inside the contact, and can only be derived for a limited number of special cases, the general case can be approximated using

$$\mathcal{E}_{f,SF} = \left\{ f_c \mid f_t^2 + \frac{m_n^2}{e_n^2} \leq \mu^2 P^2 \right\} , \quad f_t = \sqrt{f_x^2 + f_y^2}. \quad (4.3)$$

This formulation forms a contact ellipsoid $\mathcal{E}_{f,SF}$ which describes the relationship between the tangential force $f_t \in \mathbb{R}^3$ and friction moment $m_n \in \mathbb{R}^3$. The friction parameters in this expression remain the same as for the friction cone, with the additional m_n being the magnitude of the frictional moment, e_n being the eccentricity parameter i.e. the height of the aforementioned ellipsoid and P being the magnitude of the pressure applied from the contact point along the contact normal \mathbf{n} [70, 72].

Based on the model categories described above, the most representative for this project's case, are the SF models since these can provide information about the contact surface's shape, thus enabling the reconstruction of the contact shape from the application of a force distribution [128] i.e. the Inverse Elasticity Problem (IEP). Additionally, these models support descriptions of friction which is crucial to manipulate objects in hand. Illustrations of the system as a SF with friction cone, pressure distribution and the enabling of force closure can be seen in Fig. 4.2 and Fig. 4.3 respectively.

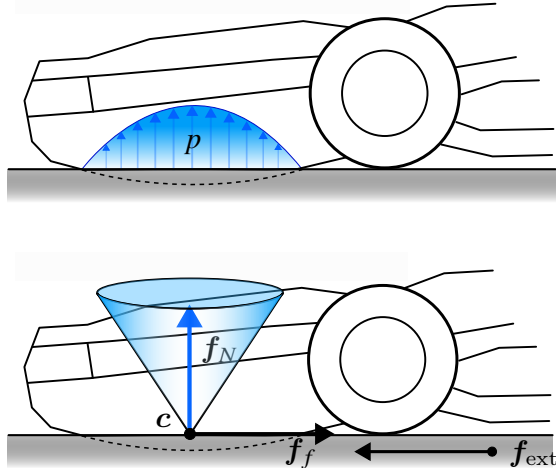


Fig. 4.2: The pressure distribution p and friction cone of a SF model experiencing an external force f_{ext} .

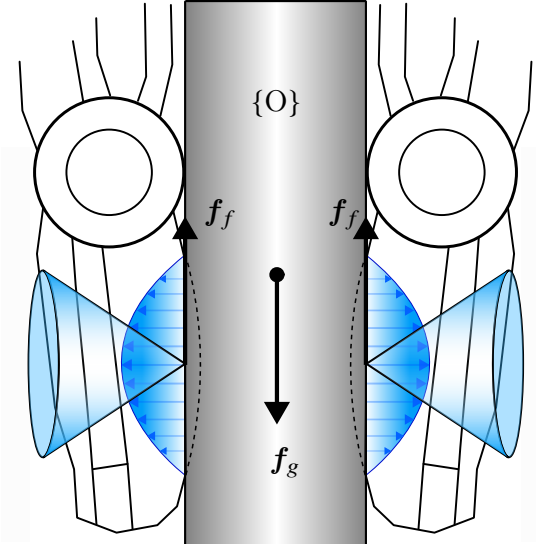


Fig. 4.3: the pressure distribution and friction cone causing force closure to prevent the object $\{O\}$ from falling due to the gravitational force f_g .

When modeling the kinematics of an anthropomorphic gripper with frame $\{H\} \in \mathbb{R}^{4 \times 4}$ in world frame $\{W\} \in \mathbb{R}^{4 \times 4}$ interacting with an object with frame $\{O\} \in \mathbb{R}^{4 \times 4}$ the relevant parameters must be addressed. In this system the object with position $\mathbf{p} \in \mathbb{R}^3$ and pose $\mathbf{u} \in \mathbb{R}^6$, with the orientation either being represented as a four-dimensional quaternion or a three-dimensional Euler angle, makes contact with the gripper in points $\mathbf{c}_i \in \mathbb{R}^3$. These contact points have frames $\{C_i\} \in \mathbb{R}^{4 \times 4}$ with axes $\{\mathbf{n}_i, \mathbf{t}_i, \mathbf{o}_i\} \subset \mathbb{R}^3$, where $\mathbf{n}_i \in \mathbb{R}^3$ points perpendicular to the contact plain towards the object, while the remaining are contained within the contact plane. For each of these parameters $i = 1, 2, \dots, n_c$, where n_c is the number of contact points. The twist of $\{O\}$ described in $\{W\}$ is denoted $\mathbf{v} = [\mathbf{v}^\top \ \boldsymbol{\omega}^\top]^\top \in \mathbb{R}^6$ while the non-contact wrench i.e. the wrench caused by external forces such as collisions with the environment and gravity, is $\mathbf{w} = [\mathbf{f}^\top \ \mathbf{m}^\top]^\top \in \mathbb{R}^6$. The gripper's state is described in terms of its

joints, of which it has n_q , named $\mathbf{q} = [q_1 \ q_2 \ \dots \ q_{n_q}]^\top \in \mathbb{R}^{n_q}$ each of which is revolute and can exert a torque $\boldsymbol{\tau} = [\tau_1 \ \tau_2 \ \dots \ \tau_{n_q}]^\top \in \mathbb{R}^{n_q}$. These parameters can be seen illustrated in Fig. 4.4 showing the system model. While only a single finger here is illustrated the naming conventions and representations simply scale to all the

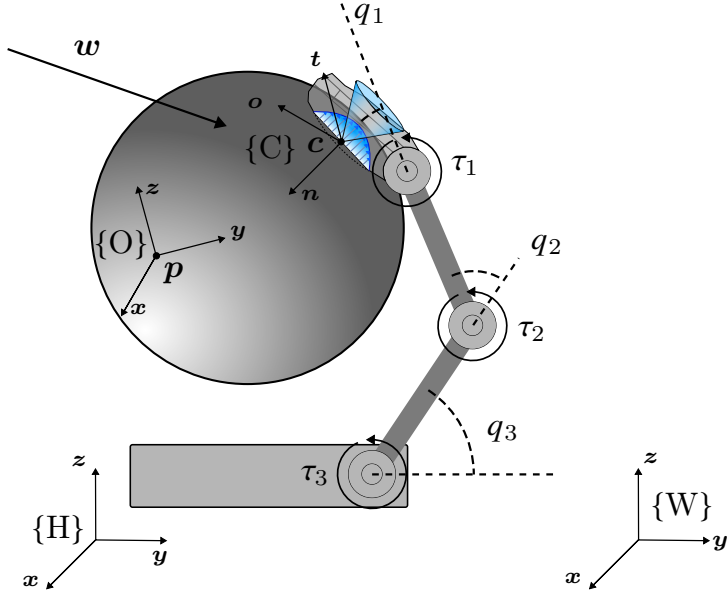


Fig. 4.4: The model of the world representation for this project.

EE's DOFs.

In this system, the twists and wrenches of a contact point c_i on the object and hand, given in contact frame $\{C\}_i$ is referred to as $\mathbf{v}_{i,\xi} \in \mathbb{R}^6$ and $\mathbf{w}_{i,\xi} \in \mathbb{R}^6$, with $\xi = \{\text{obj}, \text{hnd}\}$. Given multiple contact points, complete vectors of twist and wrench can be expressed by appending each contact point's twist and wrench vector. These contain all twists and wrenches of the grasp, one for the object and one for the hand. These vectors are referred to as

$$\mathbf{v}_{c,\xi} = [\mathbf{v}_{1,\xi}^\top \ \mathbf{v}_{2,\xi}^\top \ \dots \ \mathbf{v}_{n_c,\xi}^\top]^\top \in \mathbb{R}^{6 \cdot n_c} \quad (4.4)$$

and

$$\mathbf{w}_{c,\xi} = [\mathbf{w}_{1,\xi}^\top \ \mathbf{w}_{2,\xi}^\top \ \dots \ \mathbf{w}_{n_c,\xi}^\top]^\top \in \mathbb{R}^{6 \cdot n_c} \quad (4.5)$$

respectively.

These definitions are used to describe and analyze the kinematics of grasping and the parameters involved in holding and manipulating objects in hand, also referred to as grasp kinematics (GK). Within GK two matrices are of special interest: the grasping matrix \mathbf{G} and the hand Jacobian \mathbf{J} . The grasping matrix describes the transformation between the twist or wrench of the object in world frame $\{W\}$ to the twists or wrenches of the object in contact frames $\{C\}_i$. The grasp matrix thus can be expressed as

$$\mathbf{G} = [\mathbf{G}_1 \ \mathbf{G}_2 \ \mathbf{G}_3 \ \dots \ \mathbf{G}_{n_c}], \quad (4.6)$$

where $\mathbf{G}_i \in \mathbb{R}^{6 \times 6}$ describes the transformation from $\{W\}$ to the individual $\{C\}_i$, and thus $\mathbf{G} \in \mathbb{R}^{6 \times 6 \cdot n_c}$ describes the transformations for all contact points. Using this grasp matrix, the object wrench and twist can be computed in all contact frames as

$$\mathbf{v}_{c,\text{obj}} = \mathbf{G}^\top \mathbf{v} \quad \text{and} \quad \mathbf{w}_{c,\text{obj}} = \mathbf{G}^\top \mathbf{w}. \quad (4.7)$$

While the grasp matrix describes the transformation from $\{W\}$ to object contact frames, the hand Jacobian relates the joint velocities and torques to the contact twists and wrenches on the hand. The hand Jacobian can thus be

expressed as

$$\mathbf{J} = [\mathbf{J}_1^\top \mathbf{J}_2^\top \mathbf{J}_3^\top \cdots \mathbf{J}_{n_c}^\top]^\top, \quad (4.8)$$

for all contact points. Here $\mathbf{J}_i \in \mathbb{R}^{6 \times n_q}$ for $i = 1, 2, \dots, n_c$ are the individual contact point's hand Jacobians and thus $\mathbf{J} \in \mathbb{R}^{6 \cdot n_c \times n_q}$ is the complete. Using the complete hand Jacobian, the contact twists and wrenches on the hand can be related to the joint velocities and torques as

$$\boldsymbol{\nu}_{c,\text{hnd}} = \mathbf{J}\dot{\boldsymbol{q}} \quad \text{and} \quad \boldsymbol{\tau} = \mathbf{J}^\top \boldsymbol{w}_{c,\text{hnd}}. \quad (4.9)$$

The modeling described above will enable the use of methods for solving the presented problems. These methods will be determined in Chapter 3.

Chapter 5

Tactile Perception

To solve problem 2 and 3, the tactile perception solution must provide estimates of contact positions, contact normals and skew forces.

This chapter presents an analysis of the performance of different techniques to solve these problems, including a DL model for simulating realistic tactile skew forces, Recursive Least Squares (RLS) for estimating contact normals and the contact positions from the grasping \mathbf{G} . Contact normals are essential for accurately estimating the pose of an object in contact, while skew forces are critical for predicting the behavior of an object when it is grasped and manipulated by the SDH.

Firstly, the RLS methodology is presented for normal estimation $\mathbf{n}_{c,i} = [n_{i,x}, n_{i,y}, n_{i,z}]^\top \in \mathbb{R}^3$, where $i \in \{0, 1, \dots, n_c\}$ and n_c is the number of contact points, followed by the experimental setup and result representation.

Secondly, the technique behind estimating the skew forces $\mathbf{f}_{c,i} = [f_{i,x}, f_{i,y}, f_{i,z}]^\top \in \mathbb{R}^3$, where i goes from 1 to n_c as with the contact normals, is presented, which includes the DL models architecture as well as the methodology used to test the network. The testing methodology involves the use of various input data, and the output is analyzed for accuracy and realism. The findings are presented and discussed, including the strengths and weaknesses of the network in simulating tactile data. Finally, an assessment is made of the network's ability to produce tactile data that is realistic.

Finally, the contact positions $\mathbf{c}_i = [c_{i,x}, c_{i,y}, c_{i,z}]^\top \in \mathbb{R}^3$, which has the same bounds as the skew forces and contact normals are found and evaluated from the grasping matrix \mathbf{G} provided by [88].

The skew force and normal estimates are compared to the ones provided by Gazebo's physics engine, and the known GT from where conclusions are drawn.

The software used in this chapter is a regression neural network implemented as a Gazebo ModelPlugin [129] in C++. However, the DL model plugin used in the original publication [88] has not been updated since 2018, making the code incompatible with the current version of Gazebo API. Moreover, the licensing issues with the files in the `xmlrpc++` library, which were used for base64 encoding and decoding, necessitated their removal [130]. To address these issues, each has been resolved and the plugin has been reorganized and repackaged for compatibility with the current version of Gazebo. The original version of the plugin can be found in [131], while the fixed and updated version is available at [132].

The availability of the updated plugin ensures that the project can continue to benefit from the capabilities of the MLP based DL model for simulating realistic tactile data in the current version of Gazebo.

5.1 Methods

5.1.1 Recursive Least Squares

To use RLS to estimate the contact normal, we require the estimated linear velocity $\hat{\mathbf{v}} \in \mathbb{R}^3$. However, since the contact points may not be consistent across the surface during motion, some points may be missing at certain time steps. To address this issue, the centroid of the contact points $\bar{\mathbf{c}}_t \in \mathbb{R}^3$ at time t is used as a representative value for each time step. Therefore, we can compute the estimated linear velocity as

$$\hat{\mathbf{v}} = \frac{\bar{\mathbf{c}}_t - \bar{\mathbf{c}}_{t-1}}{\Delta t}, \quad (5.1)$$

where $t - 1$ is the previous time step and $\Delta t \in \mathbb{R}$ is the time between samples, which in this case is 0.01 s as the sampling frequency is 100 Hz. The velocity at the fingertip in contact will then be computed as

$$\mathbf{v}_{tip} = \hat{\mathbf{v}} + [\boldsymbol{\omega}]_{\times} \mathbf{R}_{tcp}^{base} \mathbf{r}, \quad (5.2)$$

where $\hat{\mathbf{v}}$ is the estimated linear velocity computed from 5.1, $[\boldsymbol{\omega}]_{\times} \in \mathbb{R}^{3 \times 3}$ is the skew-symmetric matrix of the angular velocity $\boldsymbol{\omega} \in \mathbb{R}^3$ i.e.

$$[\boldsymbol{\omega}]_{\times} = \begin{bmatrix} 0 & -\omega_z & \omega_y \\ \omega_z & 0 & -\omega_x \\ -\omega_y & \omega_x & 0 \end{bmatrix}, \quad \boldsymbol{\omega} = [\omega_x, \omega_y, \omega_z], \quad (5.3)$$

$\mathbf{R}_{tcp}^{base} \in \mathbb{R}^{3 \times 3}$ is the rotation matrix from the hand's base to its Tool Center Point (TCP), and $\mathbf{r} \in \mathbb{R}^3$ is the position of the contact point in the robot's base frame.

To compute the normal estimate, additionally, an initial guess is needed which is computed by

$$\hat{\mathbf{n}}_0 = \frac{\hat{\mathbf{v}}_1 \times \hat{\mathbf{v}}_0}{\|\hat{\mathbf{v}}_1 \times \hat{\mathbf{v}}_0\|_2}, \quad (5.4)$$

where $\hat{\mathbf{n}}_0 \in \mathbb{R}^3$ is the initial estimate, $\hat{\mathbf{v}}_0$ and $\hat{\mathbf{v}}_1$ are the linear velocity estimates for time step 0 and 1, and $\|\cdot\|_2$ is the ℓ_2 -norm.

Using the quantities above, the two main components $\mathbf{L}_n^1 \in \mathbb{R}^{3 \times 3}$ and $\mathbf{L}_n^2 \in \mathbb{R}^{3 \times 3}$ of the desired estimate $\hat{\mathbf{n}}_{new} \in \mathbb{R}^3$ can be found. Firstly, \mathbf{L}_n^1 is computed as

$$\mathbf{L}_n^1 = \mathbf{L}_n^1 - \beta \Delta t \mathbf{L}_n^1 + \frac{\Delta t K_L}{1 + \|\mathbf{v}_{tip}\|_2^2} \mathbf{v}_{tip} \mathbf{v}_{tip}^T, \quad (5.5)$$

with $\beta \in \mathbb{R}$ being a decay factor, $K_L \in \mathbb{R}$ is a gain and $\|\cdot\|_2^2$ is the squared ℓ_2 -norm.

The second component \mathbf{L}_n^2 is computed by

$$\mathbf{L}_n^2 = \mathbf{L}_n^2 - \beta \Delta t \mathbf{L}_n^2 + \frac{\Delta t K_L}{1 + \|\boldsymbol{\nabla}\|_2^2} \boldsymbol{\nabla} \boldsymbol{\nabla}^T, \quad (5.6)$$

where $\boldsymbol{\nabla} \in \mathbb{R}^3$ is the cross product between the contact force \mathbf{f}_c and the velocity of the tip \mathbf{v}_{tip} i.e.

$$\boldsymbol{\nabla} = \mathbf{f}_c \times \mathbf{v}_{tip}. \quad (5.7)$$

Using these components a Proportional-Derivative (PD) controller is used to compute the change in normal $\dot{\mathbf{n}} \in \mathbb{R}^3$ as

$$\dot{\mathbf{n}} = -(\gamma_1 \mathbf{L}_n^1 + \gamma_2 \mathbf{L}_n^2) \mathbf{n}, \quad (5.8)$$

where $\gamma_1 \in \mathbb{R}$ is the proportional gain, $\gamma_2 \in \mathbb{R}$ is the derivative gain and \mathbf{n} is the current estimate. By computing the cross product between \mathbf{n} and $\dot{\mathbf{n}}$, the angular velocity $\boldsymbol{\omega}$ is computed

$$\boldsymbol{\omega} = \mathbf{n} \times \dot{\mathbf{n}}. \quad (5.9)$$

Finally, the new normal estimate $\mathbf{n}_{new} \in \mathbb{R}^3$ can be computed as

$$\mathbf{n}_{new} = e^{\left[\frac{\Delta t}{2} [\boldsymbol{\omega}]_{\times}\right]} \mathbf{n}, \quad (5.10)$$

where $e^{\left[\frac{\Delta t}{2} [\boldsymbol{\omega}]_{\times}\right]} \in \mathbb{R}^{3 \times 3}$ is the exponential map of the skew-symmetric matrix represents the rotation due to the angular velocity over the time step.

5.1.2 Network Architecture

In [88] two different architectures were built, where architecture B is chosen due to its better greater accuracy and lower execution time. The network architecture B can be seen in Fig. 5.1. As inputs, the network takes one contact position $\mathbf{c} = [c_x, c_y, c_z]$ along with three skew force vector samples $f_1 = [f_{1,x}, f_{1,y}, f_{1,z}]$, $f_2 = [f_{2,x}, f_{2,y}, f_{2,z}]$ and $f_3 = [f_{3,x}, f_{3,y}, f_{3,z}]$, and a temperature input $T \in \mathbb{R}$, which makes the input $[\mathbf{c}, f_1, f_2, f_3, T] \in \mathbb{R}^{13}$. The contact point and forces are extracted from Gazebo's physics engine. The outputs of the network are the data format produced by the physical sensor i.e. an output vector of $[pdc, pac, tdc, tac, e_1, \dots, e_{19}] \in \mathbb{R}^{23}$, where pdc is the pressure DC signal, pac is the pressure AC signal, tdc is the temperature DC signal, tac is the temperature AC signal and e_1 to e_{19} are the electrode activations. The electrode activations can, according to SynTouch [**biotac-syntouch-manual**], can be related to physical quantities by equations which take raw 12-bit integer sensor readings in [0, 4095] those values depend on the skin deformation and require individual calibration.

The network architecture consists of four MLPs, one for interpreting the position input, one for interpreting the force inputs, one for interpreting the temperature input, and one for combining the interpretations of force and position inputs. MLP 1, is responsible for interpreting the position data, consists of four hidden layers, three of which contain 512 neurons and uses Rectified Linear Unit (ReLU) as the activation function, while the last uses a linear activation function with 64 neurons. The activation functions can be seen marked red if they are ReLU, green if they are linear activation functions and blue if they are sigmoid activation functions in Fig. 5.1.

MLP 2 interprets the force inputs but rather than using 512, uses 256 for its hidden layers, while still having the linear activation function and the 64 neurons in its fourth layer. This MLP further differs as the 256 neuron layers apply ℓ_1 bias regularization. The MLP 3 produces a temperature correction vector using two hidden layers, one with 256 neurons and a sigmoid activation function and one with 23 neurons and a linear activation function. The last MLP, MLP 4 takes in the element-wise product of MLP 1 and 2, parses the product through two 256 neuron layers with ReLU and one 23 neuron layer with a linear activation function.

The products of MLP 3 and 4 are summed and parsed as the model's output. All os this can be seen in Fig. 5.1.

5.1.3 Network Training Procedure

The model described in 5.1.2 Network Architecture was trained using a custom dataset collected by the authors. Instead of retraining the model, the provided weights in the paper's code were utilized. The dataset, denoted as \mathbf{D} , comprises $N_{dp} = 300,000$ readings from tactile sensors. It includes complete BioTac sensor data, as well as the corresponding reference forces and contact points. The structure of dataset D can be represented as follows

$$\mathbf{D} = \begin{bmatrix} 0 & pcd & pac & tdc & tac & e_1 & \dots & e_{19} & f_{1,x} & \dots & f_{3,z} & c_x & c_y & c_z \\ 1 & pcd & pac & tdc & tac & e_1 & \dots & e_{19} & f_{1,x} & \dots & f_{3,z} & c_x & c_y & c_z \\ \vdots & & & & & & & & \vdots & & & & & \\ N_{dp} & pcd & pac & tdc & tac & e_1 & \dots & e_{19} & f_{1,x} & \dots & f_{3,z} & c_x & c_y & c_z \end{bmatrix} \in \mathbb{R}^{N_{dp} \times 35}. \quad (5.11)$$

To ensure consistency and avoid bias, all inputs are standardized by normalizing them to have zero mean and unit variance, using the distribution of the captured data. In order to prevent overfitting and unrealistic reactions to high-frequency inputs that the physics simulator cannot accurately reproduce, the three force vectors are sampled at intervals of 100 ms. The BioTac sensor electrode values display a non-linear relationship with device temperature. Attempts to address this issue before inputting the data led to poor performance. Instead, the network was trained to independently compensate for this dependency. During simulation, a constant temperature was assumed, typically corresponding to the average temperature of the room when the data was collected. This temperature was not made public in neither [133] nor [88]. The network generates simulated electrode and pressure signals as outputs but currently does not simulate temperature outputs.

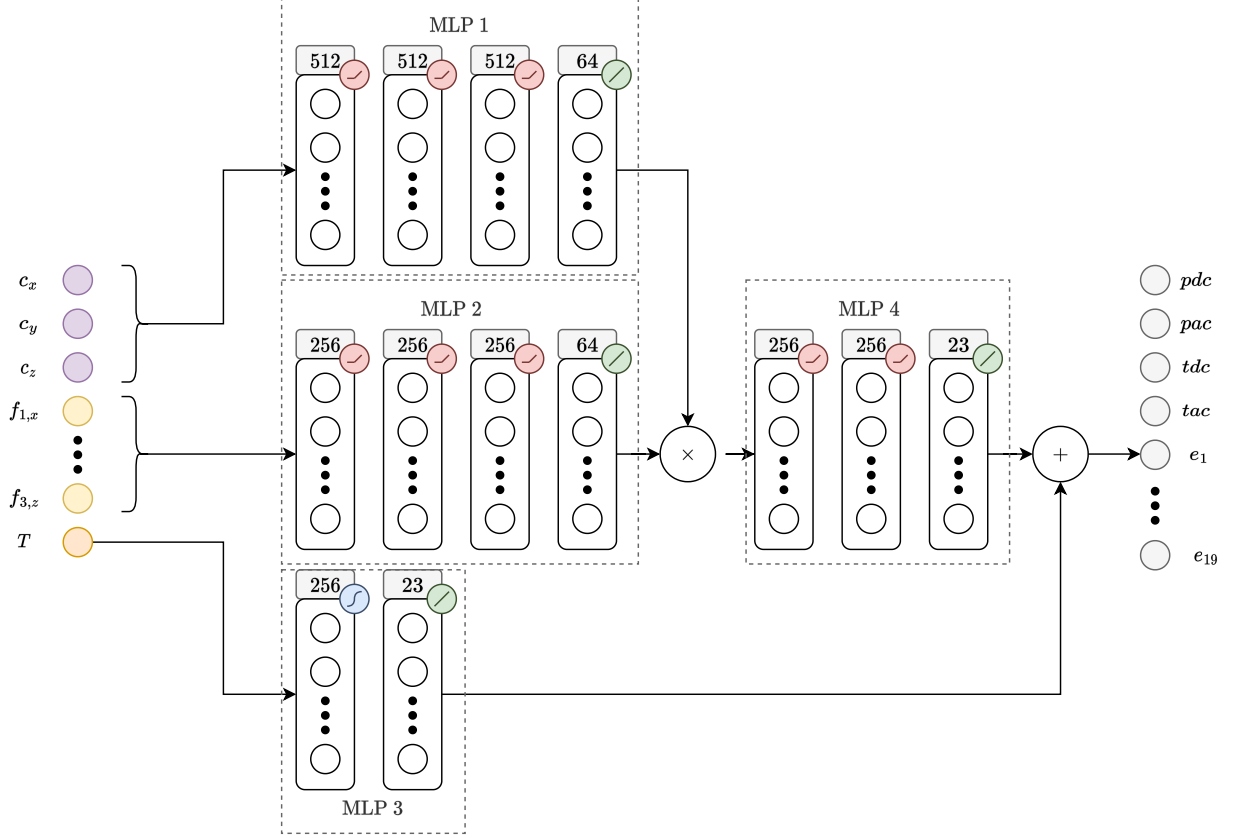


Fig. 5.1: DL model B from [88], which also has provided inspiration for this illustration.

The forces were collected using a calibrated six-axis force-torque sensor [134] with a nominal force resolution better than 0.01 N. The contact position is reconstructed optically using a calibrated HD webcam and two AprilTag markers [135], one mounted on the BioTac and one attached to the probe object. The setup for this can be seen in Fig. 5.2. Once the contact positions were collected, optimization-based calibrations were made to gain more accurate position estimates.

The data set has been made publicly available and can be found in [133].

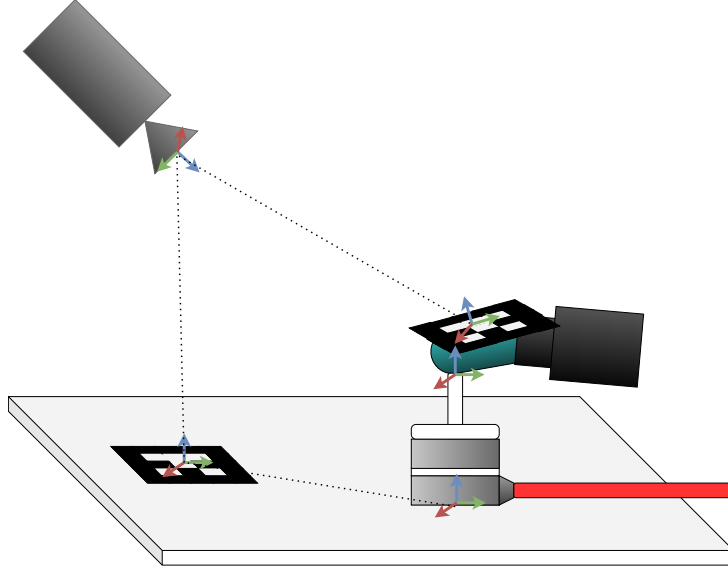


Fig. 5.2: Experimental setup for gathering data to train DL model B, as inspired by [88].

5.2 Experimental Setup

5.2.1 Contact Normal Estimation

To test the RLS method's ability to estimate contact normals the index finger makes contact with a flat surface as shown in Fig. 5.3(a), through flexion and ulnar deviation a contact path is created as shown in Fig. 5.3(b). The motion is done throughout 14 s, and due to a significant presence of noise in the simulated tactile sensors, the contact position data is filtered using a rolling low pass filter with window size 100. The experiment was conducted with the finger on the surface facing $-y$, meaning the GT normal is $\mathbf{n}_{gt} = [0, -1, 0]$ as shown in Fig. 5.3(a).

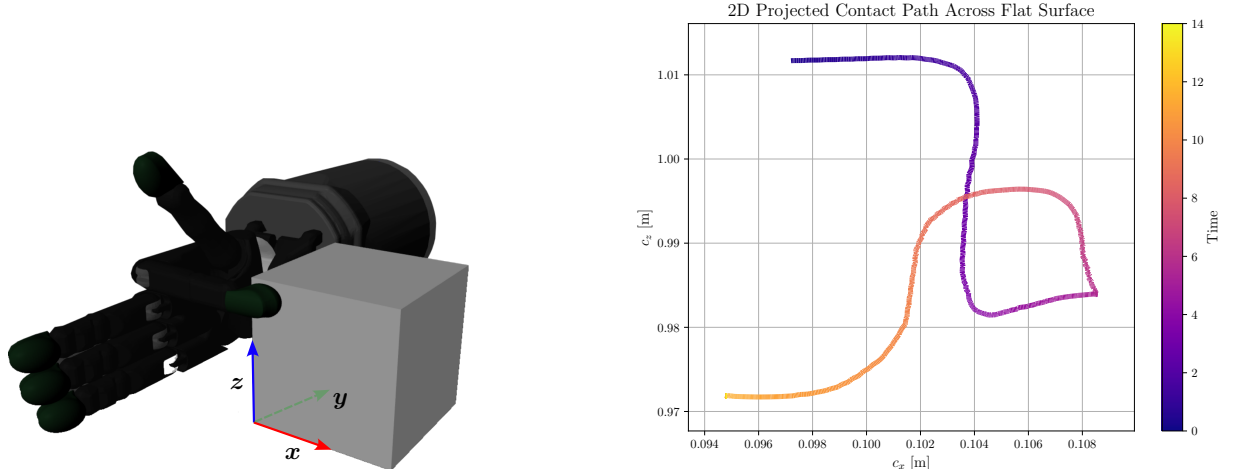
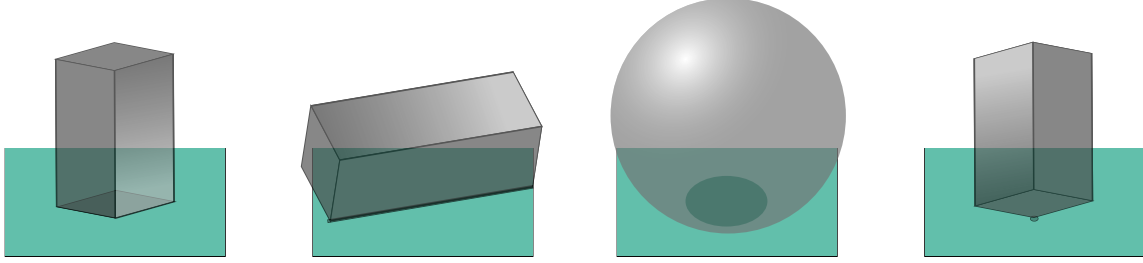


Fig. 5.3: Experimental setup and index finger's contact path when sampling contact data for normal estimation.

5.2.2 Skew Force Estimation

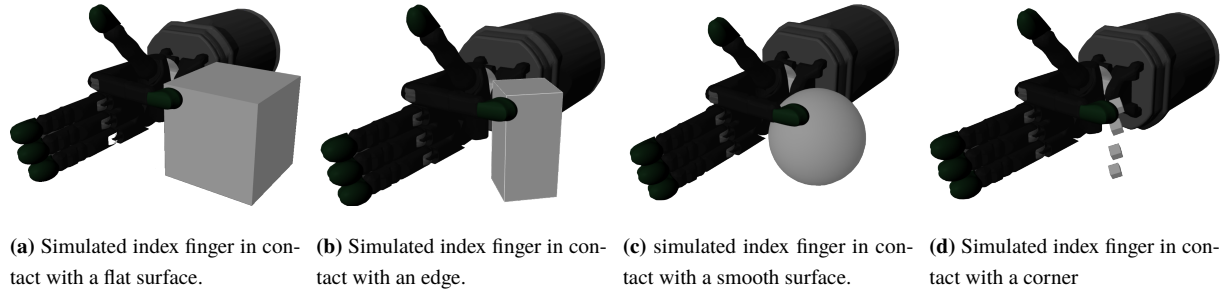
To test the performance of the DL model, four objects surfaces were used with known normals. These can be seen in Fig. 5.4 as a flat surface, an edge, a smooth surface and a corner.



(a) Finger in contact with a flat surface. (b) Finger in contact with an edge. (c) Finger in contact with a smooth surface. (d) Finger in contact with a corner.

Fig. 5.4: The four surfaces used to test the performance of the DL model's ability to represent surfaces.

Within the simulation, the index finger is set to make contact with each surface, as shown in Fig. 5.5.



(a) Simulated index finger in contact with a flat surface. (b) Simulated index finger in contact with an edge. (c) simulated index finger in contact with a smooth surface. (d) Simulated index finger in contact with a corner

Fig. 5.5: The simulated SDH in contact with the four surfaces used to test the performance of the DL model's ability to represent surfaces. In each case, the contact is made by the index finger.

When contact is made the inputs and outputs of the DL model are recorded over 30 s, which with a sampling frequency of 100 Hz results in 3000 samples. As inputs are collected, the contact positions and forces are given by Gazebo in $\{W\}$, which then is transformed into the contact frame $\{C\}$ using the grasping matrix G . Due to contact data in Gazebo being prone to noise, an exponential decay filter is additionally applied.

5.3 Results

5.3.1 Contact Normals

Upon estimating the linear velocities Fig. 5.6 was produced, which shows the three velocity components. Due to the great presence of noise, a rolling low pass filter was applied with a window size of 100. As one would expect v_y shows a negligible magnitude.

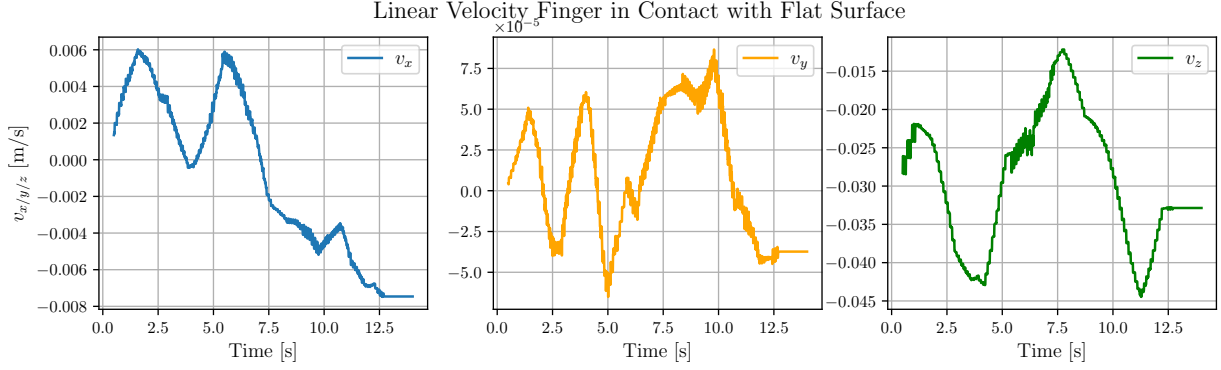


Fig. 5.6: Linear velocities of the contact points when the index finger moves across a flat surface.

Based on these the contact normals were estimated using RLS, which results in Fig. 5.7, which show great consistency and accuracy over the 14 s the experiment was performed.

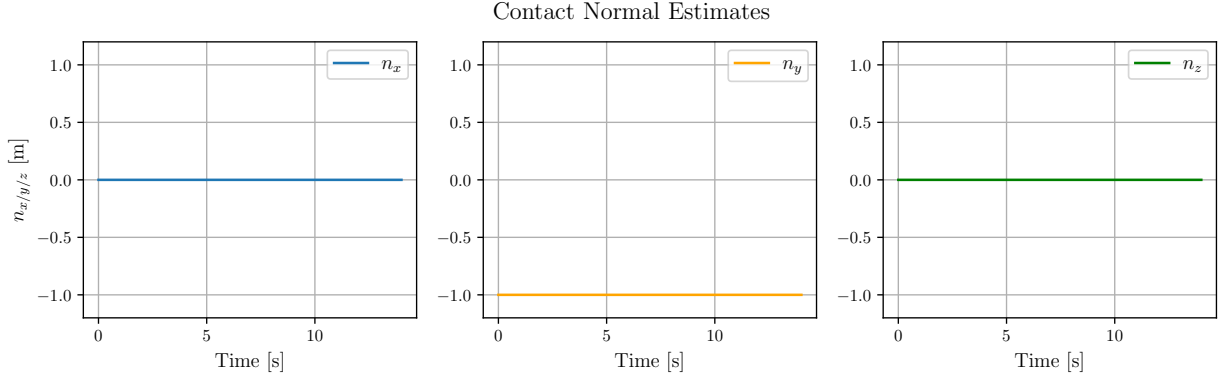


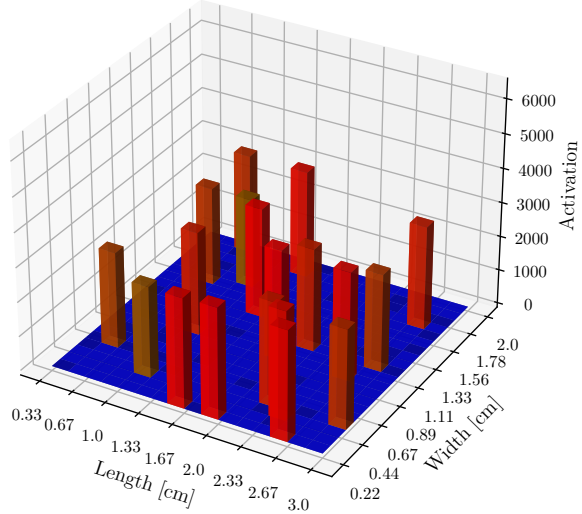
Fig. 5.7: The normal estimates across time as the experiment was executed.

5.3.2 Skew Forces

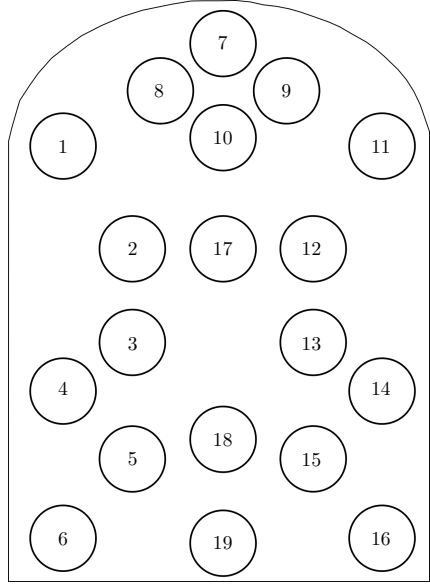
After executing the DL model on all cases, the resulting simulated electrode activations were discovered to be infinite. Consequently, efforts were undertaken to address this issue. It was determined that the model does not include layer-wise normalization to establish limits on feature responses. The addition of this normalization procedure resulted in the network outputting values within the expected range. Fig. 5.8(a) shows a 3D plot of the electrode activations after layer-wise normalization, while Fig. 5.8(b) shows a 2D projection of the finger tip with its electrodes labeled.

Fig. 5.9 illustrates the inputs and outputs of the DL model when the SDH's index finger makes contact with a flat surface. As seen here the output of the model is independent of the input. In an attempt to isolate a potential cause for this behavior, data from the custom data set on which the model had been trained, is applied and similar results

Simulated Electrode Measurements - Flat Surface



(a) 3D plot of electrode activations when the SDH's index finger makes contact with a flat surface.



(b) Map showing a 2D projection of the electrodes' positions and numbers.

Fig. 5.8: 3D plot of electrode activations and 2D electrode map with labels.

were found as seen in Fig. 5.10. The missing elements from this graph are value responses from the network of `inf`, which is a reference to the highest representable value by the system and is therefore not included.

Due to this independence of input, the electrodes, and by extension the DL model is not judged to be able to accurately simulate skew forces for a BioTac sensor in contact. The contact data from the remaining experiments can be found in Appendix B, which show a similar pattern.

Contact Forces and Electrode Activations - Flat Surface

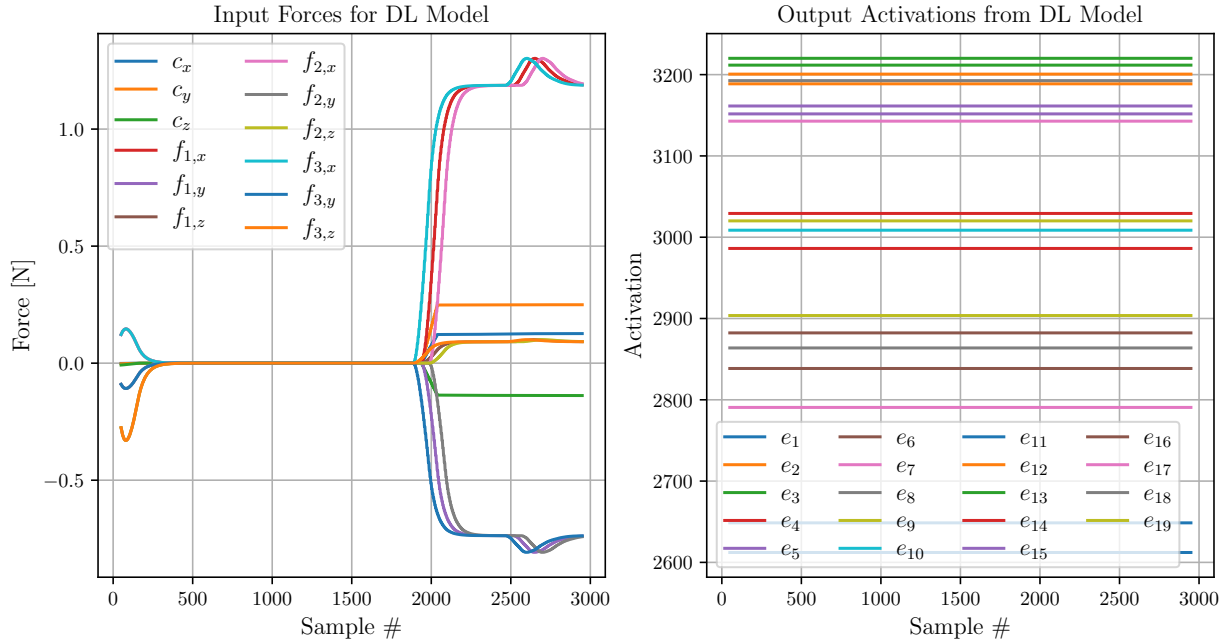


Fig. 5.9: The simulated tactile electrode activations the index finger is in contact with a flat surface.

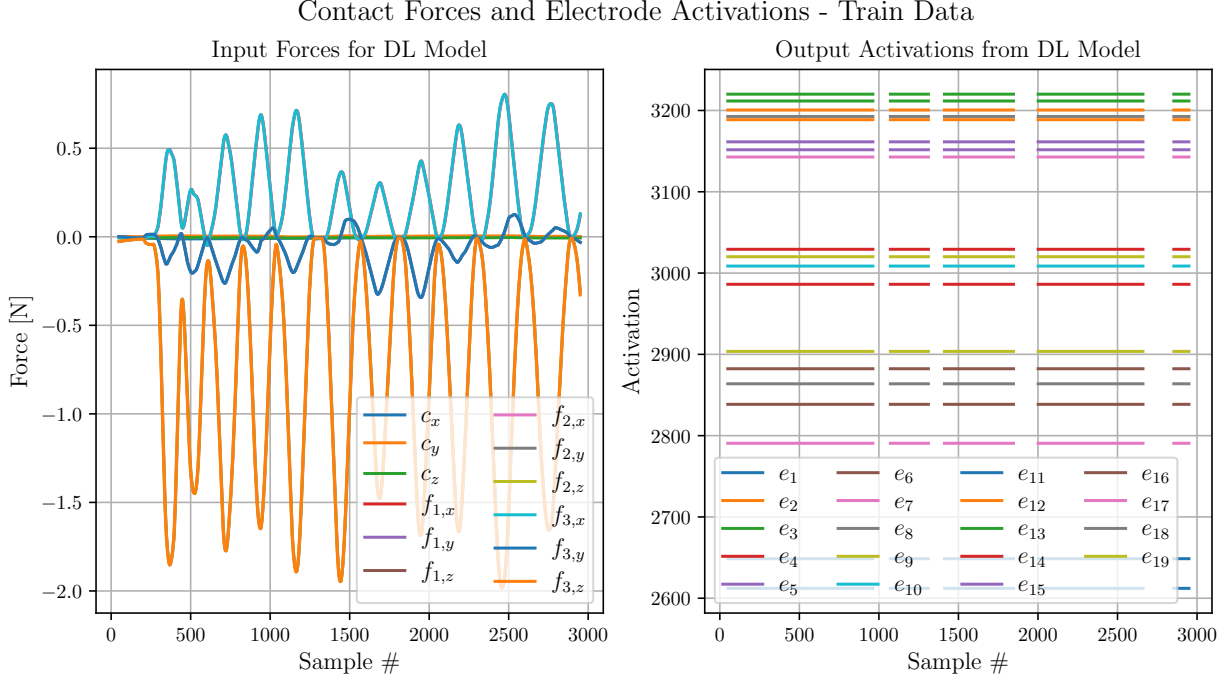
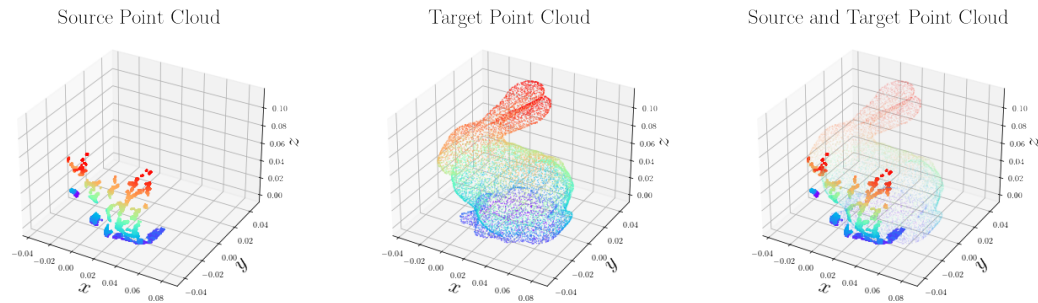


Fig. 5.10: The simulated tactile electrode activations when data the DL model was trained on is applied.

Contact Positions

The contact positions were determined by utilizing the grasping matrix \mathbf{G} and the transformation matrices for each taxel, as provided by [131]. The points in the world frame $\{\mathbf{W}\}$ were generated using Gazebo's physics engine, and the transformations were applied accordingly. In order to assess the engine's capability to represent contact points, a 3D mesh of the Stanford bunny [136] was used. The contact points were recorded during the sampling process, as depicted in Fig. 5.11. In Fig. 5.11(a), the contact points obtained by moving the fingers across the 3D mesh are shown. Fig. 5.11(b) displays the 3D mesh sampled to consist of 10.000 points, and Fig. 5.11(c) illustrates both the contact points and the sampled 3D mesh.



(a) The source PC generated from simulated contact points. (b) The target PC generated by sampling the model mesh with 10.000 points. (c) The source PC overlaid the target PC, showing their fit.

Fig. 5.11: 3D plots showing the sampled source and target PCs along with a plot showing both of them overlaid.

5.3.3 Physics Engine Comparison

Gazebo's physics engine provides interpretations of tactile contacts for models containing a contact sensor model plugin. The data comes in the form of a `ContactState` which contain the contact points in $\{W\}$, wrenches, depth and more. As a replacement for the lacking skew forces from the DL method and a possible extension of the normal estimation, Gazebo's physics engine is considered a potential supplement to the methods presented. The data sampling in this section is restricted to 100 Hz over 100 s.

The contact forces and torques generated by the engine are shown in Fig. 5.13(a) and Fig. 5.13(b), for the Shadow Dexterous finger's being in contact with an edge. The vectors here are projected into the xy-plane due to the z-component showing a negligible magnitude due to being parallel with the edge, as shown in Fig. 5.12.

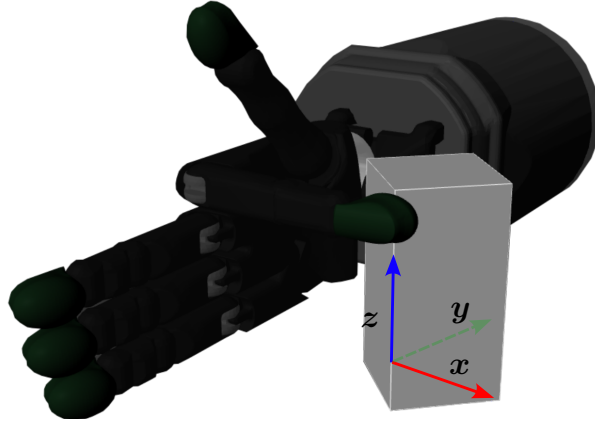
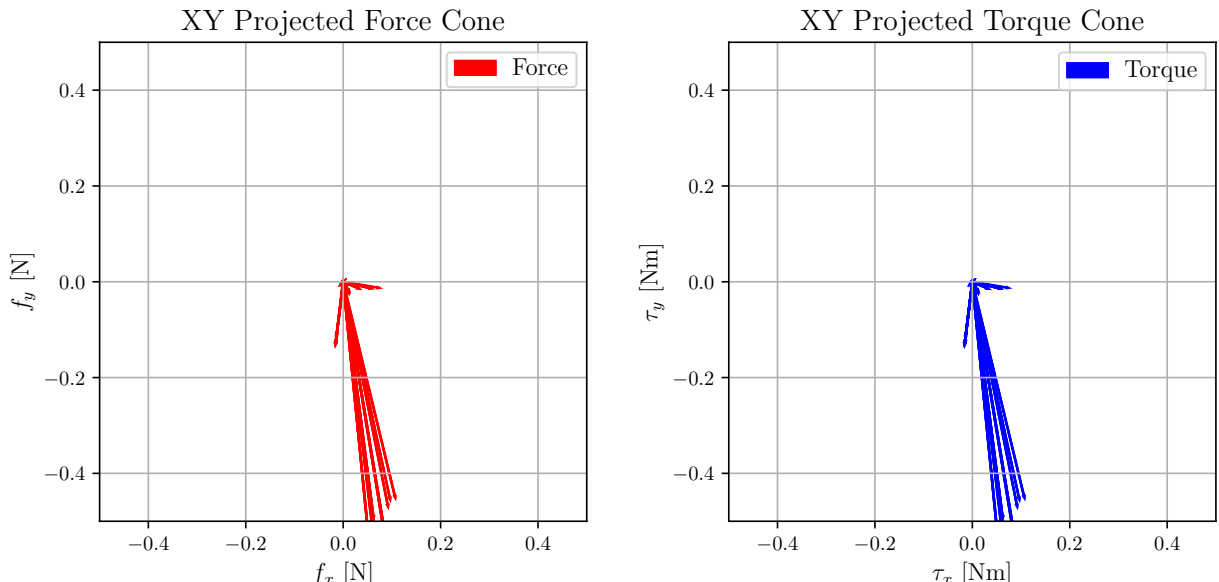


Fig. 5.12: Simulated SDH when in contact with an edge with the coordinate system.



(a) XY projected force cone produced by Gazebo's physics engine when the SDH is in contact with an edge.

(b) XY projected torque cone produced by Gazebo's physics engine when the SDH is in contact with an edge.

Fig. 5.13: XY projected force and torque cones produced by Gazebo's physics engine when the SDH is in contact with an edge. The normals however posed a challenge, as the colliding meshes caused a misinterpretation by the physics engine to produce contact normals which were reflected 180°. This can be seen in Fig. 5.14(a). This was solved by sampling a set of contact normals over 10 time steps, reducing the sampling frequency to 10 Hz. These were then

clustered using Euclidean clustering with an ϵ of 1 cm and 3 as the minimum number of samples to define a cluster. The centroid of each cluster was then used as the representative and the normal cones shown in Fig. 5.14(b) were achieved.

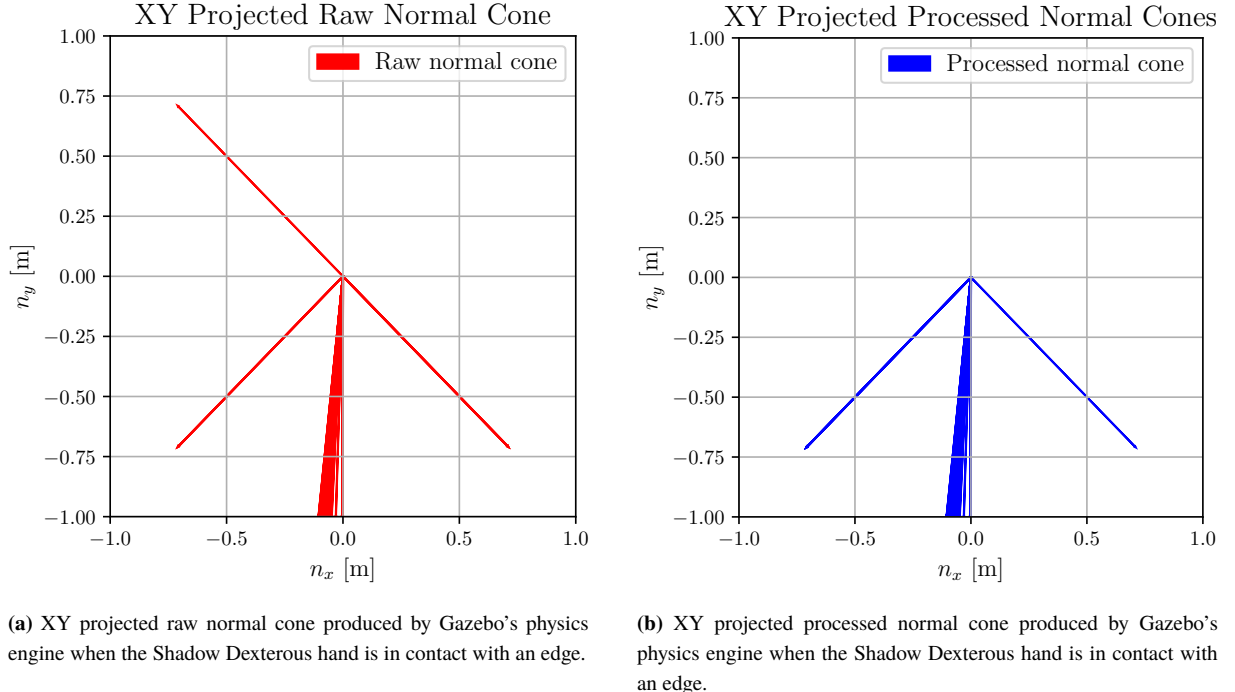


Fig. 5.14: XY projected raw and processed normal cones produced by Gazebo's physics engine when the Shadow Dexterous hand is in contact with an edge.

Finally, the angle errors θ_e between the ground truth normals \mathbf{n}_{gt} and the sampled contact normals were found for each of the four presented surfaces. The probability distributions over angle errors $P(\theta_e)$ in degrees can be seen in Fig. 5.15.

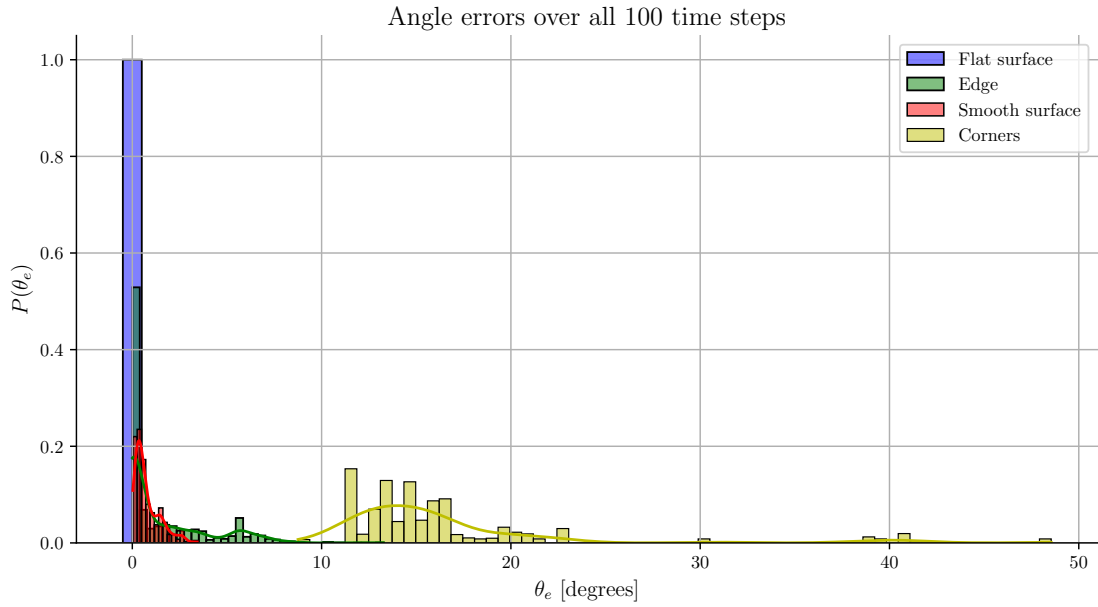


Fig. 5.15: Probability distributions $P(\theta_e)$ of the angle error θ_e between simulated and GT contact normals for each tested surface.

5.4 Discussion & Conclusion

In this study, the performance of a DL model in estimating the tactile perception of a BioTac sensor when in contact with different objects is evaluated. The findings indicate that the DL model did not provide any useful information in this study. The lack of accuracy in simulating the electrode activations limits the usefulness of the model in applications that require tactile force sensing. This finding highlights the importance of carefully evaluating the performance of DL models in specific applications and contexts, as they may not always provide the expected benefits. It was at the time of this project not possible to replicate the tactile information from the original paper [88]. Among the possible reasons for the lacking performance possible causes include non-representative weights, which due to the lack of transparency means no method exists to determine if the weights utility and Gazebo's API change may include unforeseen differences. To address these issues, the DL model could be retrained to ensure the legitimacy of the weights, given the dataset causes the performance presented in [88]. This was however not done due to the time constraint of this project.

Contact normals were found using simulated contact points and the RLS method to estimate these values. However, the contact normals produced by Gazebo's physics engine were acceptable and could be used to supplement the methods presented. For this reason, the contact points and normals produced by Gazebo's physics engine were applied in the solution to problem 2.

By estimating the contact normals, a valuable benefit is obtained as it facilitates the detection of sturdy surface characteristics. Consequently, this capability has the potential to reduce the search area for the pose estimation algorithm examined in Chapter 6. Additionally, the aforementioned chapter has successfully showcased that corners, being intricate surface features, exhibit the highest angle error, aligning with initial expectations.

In conclusion, this study provides insights into the limitations of DL models in estimating tactile perception and highlights the importance of considering alternative methods, such as physics engine simulations, to supplement or replace DL models when necessary. Future studies could explore other DL architectures or combinations of different methods to improve the accuracy and usefulness of tactile perception estimation.

Chapter 6

Pose Estimation

This chapter focuses on pose estimation, specifically addressing the optimization-based PCR problem. It introduces the RCQP and GNC methods used to solve this problem and evaluates their performance in estimating the pose of the object of interest. The primary objective is to assess the extent to which RCQP and GNC can accurately estimate the position and orientation of the object, aiming for an orientational error less than 5° and a positional error less than 1 cm as mentioned in 1.2 Problem Description. Importantly, it is assumed throughout the chapter that the object of interest is known, eliminating the need for classification.

To achieve this goal, the chapter presents the methodologies employed, the experimental setup, and the obtained results. The results obtained in this chapter encompass two main aspects 1) synthetic source data is utilized, and generated from the target data to ensure accurate correspondences. This allows for the evaluation of the methods' robustness by introducing varying percentages of outliers. 2) the methods are applied to sampled data from Chapter 5 to estimate the pose of the object based on computed correspondences.

Furthermore, in addition to solving the pose estimation problem, the chapter includes an estimation of the signal-to-outlier ratio. This is achieved by utilizing the weights produced by GNC. The estimation is conducted firstly on the synthetic source data where the ground truth is known and secondly on the sampled source data where the outlier ratio is unknown.

6.1 Problem

In this chapter, the RCQP method with GNC will be presented along with its performance in solving the PCR problem. The produced source data \mathbf{X} in Chapter 5 is a PC of the form

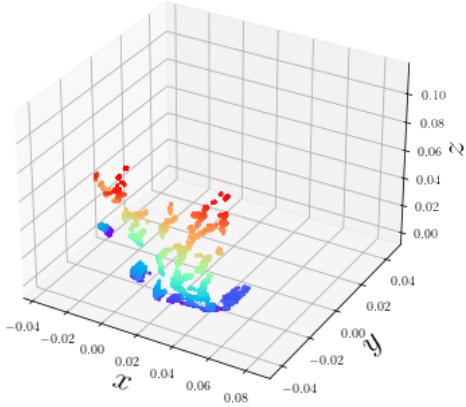
$$\mathbf{X} = \begin{bmatrix} c_x & c_y & c_z & n_x & n_y & n_z \\ c_x & c_y & c_z & n_x & n_y & n_z \\ \vdots \\ c_x & c_y & c_z & n_x & n_y & n_z \end{bmatrix} \in \mathbb{R}^{M \times 6}, \quad (6.1)$$

where $\mathbf{c} = [c_x, c_y, c_z]$ is a contact point, $\mathbf{n} = [n_x, n_y, n_z]$ is the corresponding point's normal vector and M is the number of source data points. The target data \mathbf{Y} is structured likewise, except for the number of target data points being N , where $N \geq M$. For convenience, the i 'th row in source data is referred to as \mathbf{x}_i while the i 'th row in the target data is referred to as \mathbf{y}_i .

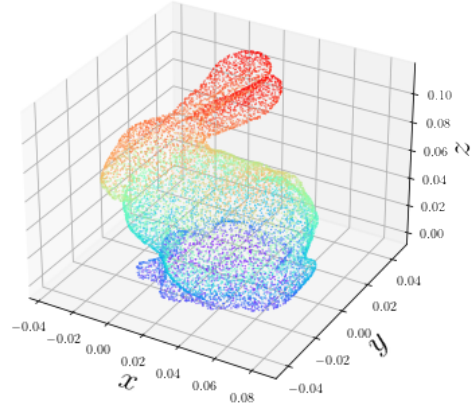
Under the assumption of already knowing the object of interest, \mathbf{Y} is generated from the mesh of the Stanford bunny model [136] with a resolution of 10.000 data points as shown in figure Fig. 6.1(b). The source data \mathbf{X} can likewise be seen in Fig. 6.1(a) as generated in Chapter 5.

To determine the transformation between the two point clouds $\mathbf{T}_\mathbf{Y}^\mathbf{X}$, correspondences must be found according to the CP. Due to \mathbf{X} being produced by local sensing with high-density sensor regions, a PC feature which exploits this is desired. The one chosen is Fast Point Feature Histograms (FPFH) which is a feature descriptor used in 3D point cloud analysis and registration tasks and provides a feature matrix $\mathbf{F} \in \mathbb{R}^{N \times 33}$. The feature descriptor calculates a histogram representation for each point by considering the local geometric properties of its neighboring points. It captures information about the distribution of surface normals and distances between points within a local neighborhood. Additionally, FPFH is computationally efficient and provides robust feature representations.

Source Point Cloud



Target Point Cloud



(a) The source data \mathbf{X} PC generated from simulated contact points, normals are also included, but not illustrated here for the sake of simplicity.

(b) The target PC generated by sampling the model mesh with 10.000 points, normals are also included, but not illustrated here for the sake of simplicity.

Fig. 6.1: 3D plots showing source and target data.

Using the correspondences found from FPFH, the pose estimation problem can be formulated as an optimization problem for determining the optimal homogeneous transformation matrix between the two point clouds $\mathbf{T}^{\star \mathbf{X}}_{\mathbf{Y}}$, which for convenience is from now on referred to as \mathbf{T}^* , by

$$\mathbf{T}^* = \arg \min_{(\mathbf{R}, \mathbf{t}) \in \text{SE}(3)} \sum_{i=1}^M d_{P_i}(\mathbf{x}_i, \mathbf{T})^2. \quad (6.2)$$

Here $\mathbf{T} = (\mathbf{R}, \mathbf{t}) \in \text{SE}(3)$ refers to the homogeneous transformation matrix $\mathbf{T} \in \mathbb{R}^{4 \times 4}$ from \mathbf{X} to \mathbf{Y} , which consists of a rotation matrix $\mathbf{R} \in \mathbb{R}^{3 \times 3}$ and a translation vector $\mathbf{t} \in \mathbb{R}^3$ as members of the Special Euclidean (SE) group in 3D, and $d_{P_i}(\cdot)$ is the distance to the matching primitive P_i . The primitives of interest in this project are point-to-point and point-to-plane, due to the presence of contact normals. The distance function will differ between primitive, and thus the ones of interest are listed as

$$\min_{\mathbf{y}' \in P} \|\mathbf{x} - \mathbf{y}'\|_2^2 = \quad (6.3)$$

$$= \|\mathbf{x} - \mathbf{y}\|_2^2 = \|\mathbf{x} - \mathbf{y}\|_{\mathbf{I}_3}^2 \quad (\text{point}) \quad (6.4)$$

$$= (\mathbf{n}^\top (\mathbf{x} - \mathbf{y}))^2 = \|\mathbf{x} - \mathbf{y}\|_{\mathbf{n}\mathbf{n}^\top}^2 \quad (\text{plane}) \quad (6.5)$$

where $\mathbf{y}' \in \mathbb{R}^3$ is the term used as a substitute for each primitive, \mathbf{x} is a 3D point, $\mathbf{I}_3 \in \mathbb{R}^{3 \times 3}$ is the identity matrix and \mathbf{n}_i is the unit normal vector for a plane. However, these are highly sensitive to outliers and noise, and thus a robust cost function $\rho(\cdot)$ is applied. Of the two presented in [119] i.e. Truncated Least Squares (TLS) and Geman McClure (GM), TLS was chosen, as it shows slightly better performance. The problem can thus be written as

$$\mathbf{T}^* = \arg \min_{(\mathbf{R}, \mathbf{t}) \in \text{SE}(3)} \sum_{i=1}^M \rho(d_{P_i}(\mathbf{x}_i, \mathbf{T})^2). \quad (6.6)$$

However solving the PCR problem globally is still a challenging endeavor, even when known correspondences are available, primarily because of the non-convex nature of the rotation constraints, where $\mathbf{R} \in \text{SE}(3)$. For this reason, global approaches are applied to deal with the problem of local minima, by starting from a convex problem, and gradually increasing the non-convexity until the original problem is retrieved, this being the purpose of GNC.

However, not all solutions when found globally are of interest, as the structure of the rotation matrix places certain quadratic constraints on the solution to be valid, such as orthonormality. From a then estimated optimal \mathbf{R}^* , the optimal translation \mathbf{t}^* can be found [118]. Thus the problem has been reduced to an orientation estimation problem to find \mathbf{R}^* .

6.2 Method

6.2.1 Graduated Non-Convexity

Rather than applying GNC for optimizing the robust cost function $\rho(\cdot)$, we fix constant μ to instead optimize

$$\mathbf{R}^* = \arg \min_{\mathbf{R} \in \text{SE}(3)} \sum_{i=1}^M \rho_\mu(d_{P_i}(\mathbf{x}_i, \mathbf{R})^2) \quad (6.7)$$

However, since this problem cannot be solved using a non-minimal solver, the Black-Rangarajan (BR) duality can be applied, given the necessary conditions are met. These conditions are as follows

$$\lim_{z \rightarrow 0} \phi'(z) = 1 \quad \text{condition 1} \quad (6.8)$$

$$\lim_{z \rightarrow \infty} \phi'(z) = 0 \quad \text{condition 2} \quad (6.9)$$

$$\phi''(z) < 0 \quad \text{condition 3} \quad (6.10)$$

Here $\phi(z)$ is defined with respect to the robust cost function ρ in the following manner

$$\phi(z) \doteq \rho(\sqrt{z}). \quad (6.11)$$

Condition 1 indicates that as the argument z approaches 0, the derivative of $\phi(z)$ approaches 1. Geometrically, it implies that near the origin, the function $\phi(z)$ grows at a similar rate as the square root function itself. This behavior ensures that small values of z are penalized appropriately by the robust cost function $\rho(\cdot)$, allowing for robustness against outliers or deviations from the assumed distribution.

Condition 2 states that as z approaches ∞ , the derivative of $\phi(z)$ tends towards 0. This implies that as the argument becomes larger, the function $\phi(z)$ approaches a plateau or a constant value. Consequently, large values of z have a diminishing effect on the robust cost function, making it less sensitive to extreme observations.

Condition 3 states that the second derivative of $\phi(z)$ is negative, indicating that the function $\phi(z)$ is concave. This concavity is crucial as it ensures that the robust cost function $\rho(\cdot)$ is monotonically increasing. In other words, as the argument z increases, the robust cost increases as well. This property is desirable in robust estimation problems, as it helps in downplaying the impact of outliers or influential points on the overall estimation.

All of these conditions are met by the TLS [119].

With these conditions fulfilled, the BR duality enables

$$\arg \min_{\mathbf{R} \in \text{SE}(3)} \sum_{i=1}^M \rho_\mu(d_{P_i}(\mathbf{x}_i, \mathbf{R})^2) = \arg \min_{\substack{\mathbf{R} \in \text{SE}(3), \\ w_i \in [0, 1]}} \sum_{i=1}^M \left[w_i d_{P_i}(\mathbf{x}_i, \mathbf{R})^2 + \Phi_{\rho_\mu}(w_i) \right], \quad (6.12)$$

whereas the rightmost side will be the problem of interest. In this expression $w_i \in [0, 1] \forall i = 1, 2, \dots, N$ are weights associated with each measurement \mathbf{x}_i and the outlier process function $\Phi_{\rho_\mu}(w_i)$, which computes a penalty based on the weight. The exact shape of $\Phi_{\rho_\mu}(w_i)$ is determined by the chosen robust cost function.

$\Phi_{\rho_\mu}(w_i)$ can simply be computed by

$$\Phi_{\rho_\mu}(w_i) = \frac{\mu(1 - w_i)}{\mu + w_i} \bar{c}^2, \quad (6.13)$$

where μ is the control parameter used to dictate to what extent the $\Phi_{\rho_\mu}(w_i)$ should be convex or non-convex. For TLS $\Phi_{\rho_\mu}(w_i)$ will become less convex as $\mu \rightarrow \infty$, while completely convex at $\mu = 0$. This effect can be seen in Fig. 6.2.

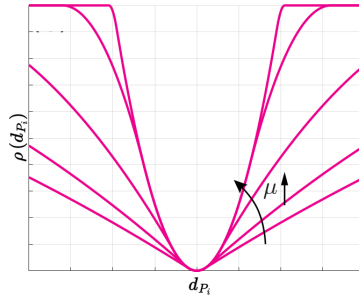


Fig. 6.2: Cost function for the TLS with

\bar{c}^2 is a given truncation threshold, which in practice is set to the maximum error expected for the inliers. Finally, w_i can be computed when using TLS by

$$w_i^{(t)} = \begin{cases} 0 & \text{if } \hat{r}_i^2 \in \left[\frac{\mu+1}{\mu} \bar{c}^2, +\infty \right] \\ \frac{\bar{c}}{\hat{r}_i} \sqrt{\mu(\mu+1)} - \mu & \text{if } \hat{r}_i^2 \in \left[\frac{\mu}{\mu+1} \bar{c}^2, \frac{\mu+1}{\mu} \bar{c}^2 \right] \\ 1 & \text{if } \hat{r}_i^2 \in \left[0, \frac{\mu}{\mu+1} \bar{c}^2 \right] \end{cases} \quad (6.14)$$

where $\hat{r}_i^2 \doteq d_{P_i}(\cdot)^2$. (6.12) can now be solved through a two-step alternating optimization. First, an outer loop is defined to which increases control parameter μ from 0 to ∞ , until a stop criterion, dictated by the cost function, is met. [119] found that an increase of μ by a factor of 1.4 provided satisfactory results. The inner loop is two-fold 1) the current estimate of $\mathbf{R}^{(t)}$ is computed by optimizing over \mathbf{R} with fixed weights w_i , also referred to as the variable update step. The variable update step can thus be written as

$$\mathbf{R}^{(t)} = \arg \min_{\mathbf{R} \in \text{SE}(3)} \sum_{i=1}^N w_i^{(t-1)} d_{P_i}(\mathbf{x}_i, \mathbf{R}) + \underbrace{\Phi_{\rho_\mu}(w_i^{(t-1)})}_{\text{constant}} \quad (6.15)$$

This optimization problem is non-convex and is solved using RCQP, which is described in 6.2.2 Relaxed Convex Quadratic Programming. 2) the found \mathbf{R} is then used to update the weights $w_i \forall i = 1, 2, \dots, N$, which typically can be solved in closed form, as formulated in (6.14), which also is referred to as the weight update step.

When executing GNC in practice, values are needed for μ_0 and $\mathbf{w}^{(0)}$, i.e. the parameters' initial values, along with an update rule for μ and a stopping criterion. In this project the initial value for μ is $\mu = 2r_{\max}^2/\bar{c}^2$ where $r_{\max}^2 \doteq \max_i(r^2(\mathbf{x}_i, \mathbf{R}^{(0)}))$, meaning the maximum residual after the first variable update, while $\mathbf{w}_i^{(0)} = 1 \forall i = 1, 2, \dots, N$. The update rule used for μ is $\mu \leftarrow 1.4\mu$, and as mentioned previously \bar{c}^2 is set to the maximum error expected for the inliers. For TLS a fitting stop criterion is chosen to be the sum weighted squared residuals, i.e.

$$\sum_{i=1}^N w_i \hat{r}_i^2. \quad (6.16)$$

These initial values, update rules and stop criterion are based on the discoveries of [119]. The GNC algorithm can be seen summarized in Algo. 1.

In Algo. 1 the stats output generally contains information about the algorithm execution such as execution time, number of iterations, and the weights \mathbf{w} .

Algorithm 1 GNC algorithm when using TLS as $\rho(\cdot)$

Input: matching pairs from (\mathbf{X}, \mathbf{Y})

Output: inliers, stats

```

1: while true do // outer loop
2:    $\mu \leftarrow 1.4\mu$ 
3:    $\mathbf{R}^{(t)} \leftarrow$  Variable Update
4:    $\mathbf{w}^{(t)} \leftarrow$  Weight Update
5:   if  $\sum_{i=1}^N w_i \hat{r}_i^2$  has converged then
6:     break
7:   end if
8: end while
9: return inliers, stats

```

6.2.2 Relaxed Convex Quadratic Programming

To compute the optimal rotation matrix \mathbf{R} , the problem definition must be expressed purely in \mathbf{R} . To do so, it will be derived from the optimization problem involving the full transformation matrix \mathbf{T} , formulated as

$$d_{P_i}^2(\mathbf{x}_i, \mathbf{T}) = (\mathbf{T} \oplus \mathbf{x}_i - \mathbf{y}_i)^\top \mathbf{C}_i (\mathbf{T} \oplus \mathbf{x}_i - \mathbf{y}_i). \quad (6.17)$$

Here $\mathbf{T} \oplus \mathbf{x}_i$ is the Euclidean transformation of \mathbf{x}_i , which is an expression linear in \mathbf{R} and t

$$\mathbf{T} \oplus \mathbf{x}_i = \mathbf{R}\mathbf{x}_i + \mathbf{t} = (\tilde{\mathbf{x}}^\top \otimes \mathbf{I}_3) \text{vec}(\mathbf{T}). \quad (6.18)$$

Here $\tilde{\mathbf{x}} = [\mathbf{x}^\top, 1]^\top$ is the homogeneous coordinate of \mathbf{x} , \otimes is the Kronecker product and $\text{vec}(\mathbf{T})$ is the vectorization of \mathbf{T} i.e.

$$\text{vec}(\mathbf{T}) = [\text{vec}(\mathbf{R})^\top, \mathbf{t}^\top]^\top \quad (6.19)$$

$$= [r_{11}, r_{12}, \dots, r_{32}, r_{33}, t_1, t_2, t_3]^\top. \quad (6.20)$$

Using this linear relationship in \mathbf{T} , (6.17) can be reformulated as

$$d_{P_i}(\mathbf{x}_i, \mathbf{T}) = \tilde{\tau}^\top \mathbf{N}_i^\top \mathbf{C}_i \mathbf{N}_i \tilde{\tau} \quad (6.21)$$

where τ is $\text{vec}(\mathbf{T})$, $\tilde{\tau}$ is the homogenized $\text{vec}(\mathbf{T})$ i.e. $[\text{vec}(\mathbf{T})^\top, 1]^\top$, and $\mathbf{N}_i = [\tilde{\mathbf{x}}_i^\top \otimes \mathbf{I}_3 | -\mathbf{y}_i] \in \mathbb{R}^{3 \times 10}$. Due to the quadratic nature of (6.21), it is possible to organize the observations and compress all the data into a single matrix $\tilde{\mathbf{M}}$ from $\tilde{\mathbf{M}}_i = \mathbf{N}_i^\top \mathbf{C}_i \mathbf{N}_i \in \mathbb{R}^{13 \times 13}$

$$f(\mathbf{T}) = \sum_{i=1}^N d_{P_i}(\mathbf{x}_i, \mathbf{T}) = \tilde{\tau}^\top \left(\sum_{i=1}^N \tilde{\mathbf{M}}_i \right) \tilde{\tau} = \tilde{\tau}^\top \tilde{\mathbf{M}} \tilde{\tau}. \quad (6.22)$$

From this expression, it can now be seen that the problem has been made independent of N . By then applying marginalization to the unconstrained parts of the known \mathbf{T} i.e. the translation t , further compression of the problem is achieved, such that

$$f^\star = \min_{\mathbf{R} \in \text{SE}(3)} \tilde{\mathbf{r}}^\top \tilde{\mathbf{Q}} \tilde{\mathbf{r}} \quad , \quad \tilde{\mathbf{r}} = [\text{vec}(\mathbf{R})^\top, 1]^\top \quad (6.23)$$

Here $\tilde{\mathbf{Q}}$ is the Schur complement of the block matrix $\tilde{\mathbf{M}}_{t,t}$ in $\tilde{\mathbf{M}}$. Here the t subscript indicates the indexes of the corresponding to translation variables and

$$\mathbf{Q} = \tilde{\mathbf{M}}_{t,t} - \tilde{\mathbf{M}}_{t,t} \tilde{\mathbf{M}}_{t,t}^{-1} \tilde{\mathbf{M}}_{t,t} \quad (6.24)$$

with $!t$ being the complement of t .

Although the problem is originally non-convex, it is approached by applying a convex relaxation technique to facilitate its solution. Although a formal proof is not presented, empirical evidence from [118] demonstrates

that this relaxation method consistently produces results that are close to the globally optimal solution for the marginalized problem.

This convex relaxation is achieved by applying Lagrangian duality to define two problems, a primary problem \mathcal{P} and a dual problem \mathcal{D} . The primary problem is an extension of (6.23), such that the necessary constraints for legal rotation matrices solutions are enforced, while the dual problem will be corresponding to a homogeneous version of the primal problem \mathcal{P} , which makes \mathcal{D} a Semidefinite Program (SDP), meaning the problem is convex and can be solved using off the shelf solvers.

To apply Lagrangian duality, strong duality must hold between \mathcal{P} and \mathcal{D} , meaning the solution to each of the problems are equal and their objective function values coincide. While this is not proven to hold, empirically this relaxation appears always to be tight, meaning strong duality holds, even under extreme conditions as asserted by [118]. This project will continue under the assumption that strong duality holds.

To formulate \mathcal{P} , the constraints of $\mathbf{R} \in \text{SE}(3)$ state that orthonormality and positive unit determinant must hold i.e.

$$\mathbf{R}^\top \mathbf{R} = \mathbf{I}_3 \quad \text{and} \quad \det(\mathbf{R}) = +1 \quad (6.25)$$

While it is appealing to formulate \mathcal{P} as a QCQP, the determinant constraint is cubic and thus does not allow this formulation. In other solutions to this problem, it is not uncommon to discard the determinant constraint [137, 138] resulting in the problem only being constrained by the orthonormality constraint. This amounts to optimizing in $O(3)$ rather than in $SO(3)$.

Instead, by introducing additional constraints, the duality of the problem can be enhanced. Each time a new scalar constraint $c_{k+1}(\cdot)$ is incorporated into the Lagrangian, a corresponding dual variable λ_{k+1} is introduced, and the dimension of the dual problem increases by one. This causes the new \mathcal{D} bound d_{k+1}^* to be at least as good as the previous problem's bound i.e.

$$d_k^* \leq d_{k+1}^* \leq f^*. \quad (6.26)$$

Since this change in \mathcal{P} causes direct changes to \mathcal{D} , \mathcal{D} is not intrinsic, instead it is dependant on the feasible region of \mathcal{P} . By utilizing this property, adding more valid quadratic constraints has been shown to improve the quality of the dual relaxation [139, Chapter 13].

Thus additional linearly independent quadratic constraints are added such as column and row-based orthonormality, along with additional quadratic constraints, which enforce the positive unit determinant, referred to as the rotation matrices handedness. This constraint states that a positive unit determinant is guaranteed if the column space of \mathbf{R} respects the right-hand rule i.e.

$$\mathbf{R}^{(1)} \times \mathbf{R}^{(2)} = \mathbf{R}^{(3)}, \quad (6.27)$$

where $\mathbf{R}^{(k)}$ is the k -th column of \mathbf{R} . Utilizing the three possible cyclic permutations of this equation provides exactly three independent quadratic constraints, which strengthens the duality between \mathcal{P} and \mathcal{D} . A final constraint can be added by homogenizing \mathcal{P} by introducing an auxiliary variable y with the constraint $y^2 = 1$. The primary problem \mathcal{P} can thus be expressed as

$$\begin{aligned} & \min_{\mathbf{R} \in \text{SE}(3)} \tilde{\mathbf{r}}^\top \tilde{\mathbf{Q}} \tilde{\mathbf{r}} \quad , \quad \tilde{\mathbf{r}} = [\text{vec}(\mathbf{R})^\top, y]^\top, \\ & \text{s.t.} \\ & \mathbf{R}^\top \mathbf{R} = y^2 \mathbf{I}_3, \\ & \mathbf{R} \mathbf{R}^\top = y^2 \mathbf{I}_3, \\ & \mathbf{R}^{(i)} \times \mathbf{R}^{(j)} = y \mathbf{R}^{(k)} \quad , \quad i, j, k = \text{cyclic}(1, 2, 3), \\ & y^2 = 1. \end{aligned} \quad (\mathcal{P})$$

To derive the dual problem \mathcal{D} , the QCQP nature of \mathcal{P} is utilized to express its Lagrangian as

$$\mathcal{L}(\tilde{\mathbf{r}}, \tilde{\lambda}) = \gamma + \tilde{\mathbf{r}}^\top \tilde{\mathbf{Z}} \tilde{\mathbf{r}}. \quad (6.28)$$

Here $\tilde{\lambda} = [\lambda^\top, \gamma]^\top \in \mathbb{R}^{22}$, where 22 is the number of constraints of \mathcal{P} , $\tilde{\mathbf{Z}} = \tilde{\mathbf{Q}} + \tilde{\mathbf{P}}(\tilde{\lambda})$, which is a penalization matrix as the sum of $\tilde{\mathbf{Q}}$, which contains all the data from \mathcal{P} , and $\tilde{\mathbf{P}}(\tilde{\lambda})$ is the accumulation of all the penalization terms corresponding to different constrain types. $\tilde{\mathbf{P}}(\tilde{\lambda})$ can be computed as

$$\tilde{\mathbf{P}}(\tilde{\lambda}) = \tilde{\mathbf{P}}_r(\Lambda_r) + \tilde{\mathbf{P}}_c(\Lambda_c) + \tilde{\mathbf{P}}_d(\{\lambda_{d_{ijk}}\}) + \tilde{\mathbf{P}}_h(\gamma), \quad (6.29)$$

which by definition is a linear function of the dual variables, where the structural pattern of the involved matrices can be found in [118]. Using this formulation of the Lagrangian, its relaxation can be solved in closed form as

$$d(\tilde{\lambda}) = \min_{\tilde{\mathbf{r}}} \mathcal{L}(\tilde{\mathbf{r}}, \tilde{\lambda}) = \min_{\tilde{\mathbf{r}}} \gamma + \tilde{\mathbf{r}}^\top \tilde{\mathbf{Z}} \tilde{\mathbf{r}} \quad (6.30)$$

$$= \begin{cases} \gamma & \text{if } \tilde{\mathbf{Z}} \succeq \mathbf{0}, \\ -\infty & \text{otherwise.} \end{cases} \quad (6.31)$$

In cases where $\tilde{\mathbf{Z}}$ is not Positive Semidefinite (PSD) no lower bound exists for this problem, and thus no optimal solution can be found. But by restricting all $\tilde{\lambda}$, to the solutions of $d(\tilde{\lambda})$ which satisfy $\tilde{\mathbf{Z}} \succeq \mathbf{0}$, the dual problem \mathcal{D} to the homogeneous primal problem \mathcal{P} is a Semidefinite Program on the form

$$\begin{aligned} d^* &= \max_{\tilde{\lambda}} \gamma, \\ \text{s.t.} \\ \tilde{\mathbf{Z}}(\tilde{\lambda}) &= \tilde{\mathbf{Q}} + \tilde{\mathbf{P}}(\tilde{\lambda}) \succeq 0. \end{aligned} \quad (\mathcal{D})$$

Which is a semidefinite program i.e. a convex problem that can be solved by out-of-the-box solvers.

From the now defined primal problem \mathcal{P} and dual problem \mathcal{D} , and under the assumption that strong duality holds $f^* = d^*$, by duality theory $\tilde{\mathbf{r}}^*$ must be a minimizer of the Lagrangian 6.28 evaluated at $\tilde{\lambda}^*$, such that

$$\mathbf{r}^* = \arg \min_{\mathbf{r}} \mathcal{L}(\mathbf{r}, \lambda^*) \Rightarrow (\tilde{\mathbf{r}}^*)^\top \tilde{\mathbf{Z}}^* \tilde{\mathbf{r}}^* = 0. \quad (6.32)$$

Assuming $\tilde{\mathbf{Z}}^*$ is PSD i.e. $\tilde{\mathbf{Z}}^* \succeq 0$, then the optimal solution $\tilde{\mathbf{r}}^*$ must lie in the nullspace of $\tilde{\mathbf{Z}}^*$ i.e. $\tilde{\mathbf{r}}^* \in \text{null}(\tilde{\mathbf{Z}}^*)$. If this was not the case, either $\text{null}(\tilde{\mathbf{Z}}^*) = \emptyset$ or $\tilde{\mathbf{r}}^* \notin \text{null}(\tilde{\mathbf{Z}}^*)$, as a direct consequence of $\tilde{\mathbf{Z}}^*$ being PSD.

Here the nullspace basis \mathbf{V} of $\tilde{\mathbf{Z}}^*$ i.e. $\mathbf{V} = \text{null}(\tilde{\mathbf{Z}}^*)$ can be computed using QR decomposition.

If it here is the case that $\text{rank}(\mathbf{V}) = 1$ then the optimal solution $\tilde{\mathbf{r}}^*$ is achieved up to a scaling factor of $1/y$, due to \mathcal{P} being homogenous. By simply dehomogenizing $\tilde{\mathbf{r}}^*$, the optimal rotation \mathbf{r}^* is found.

Verifying the legitimacy of this solution is simply done by evaluating the nullspace determinant to be unit, and the difference between the optimal value of \mathcal{P} and \mathcal{D} being 0 i.e.

$$\text{rank}(\text{null}(\tilde{\mathbf{Z}}^*)) = 1 \quad \text{and} \quad d^* - f^*(\mathbf{r}^*) = 0 \quad (6.33)$$

where $\mathbf{R}^* = \text{reshape}(\mathbf{r}^*)$.

To summarize, the RCQP algorithm can be seen in Algo. 2.

6.3 Experimental Setup

To Test the performance of the algorithms presented in 6.2 Method synthetic source data is generated based on the target data sampled from CAD model of the object of interest i.e. the Stanford bunny. The mesh is sampled uniformly with 1000 data points and with corresponding normals making up the target data, while the source data

Algorithm 2 RCQP algorithm for determining \mathbf{R}^* from $\tilde{\mathbf{r}}^\top \tilde{\mathbf{Q}} \tilde{\mathbf{r}}$

Input: Marginalized quadratic form of the primary problem, \mathcal{P} i.e. $\tilde{\mathbf{r}}^\top \tilde{\mathbf{Q}} \tilde{\mathbf{r}}$

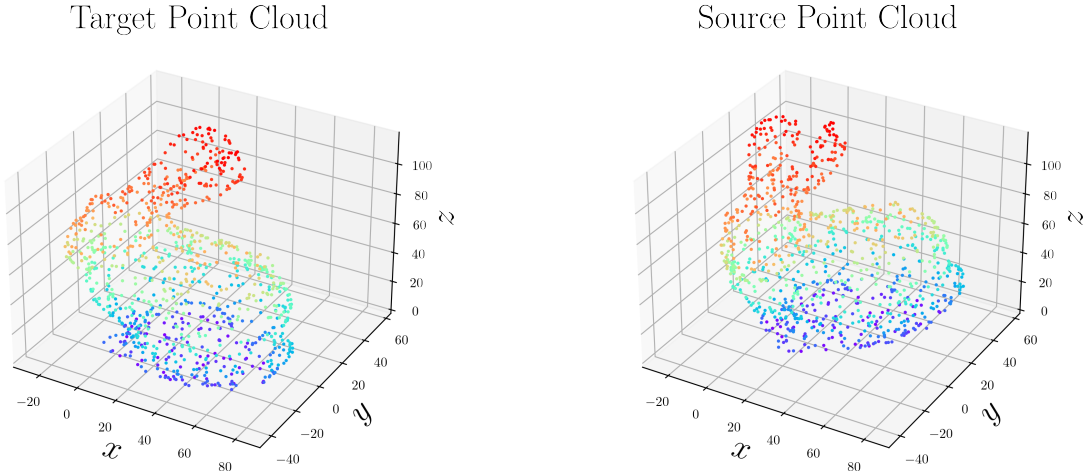
Output: Globally optimal \mathbf{R}^* , if strong duality holds

- 1: $\tilde{\mathbf{Z}}(\tilde{\lambda}) \leftarrow \text{build}(\tilde{\mathbf{Q}} + \tilde{\mathbf{P}}(\tilde{\lambda}))$ based on 6.29
 - 2: $(\tilde{\lambda}^*, \tilde{\mathbf{Z}}^*) \leftarrow \text{cvx}(\mathcal{D}(\tilde{\lambda}, \tilde{\mathbf{Z}}))$ i.e. solve the Semidefinite Program using optimization tools such as **cvx**
 - 3: $\mathbf{V} \leftarrow \text{null}(\tilde{\mathbf{Z}}^*)$, from methods such as QR decomposition.
 - 4: **ASSERT** ($\text{rank}(\mathbf{V}) == 1$), ensure the nullspace rank is unit
 - 5: **ASSERT** $((\tilde{\mathbf{r}}^*)^\top \tilde{\mathbf{Q}} \tilde{\mathbf{r}}^* - d^* < \epsilon)$, where ϵ is some threshold close to 0, to ensure strong duality
 - 6: $\mathbf{r}^* \leftarrow \tilde{\mathbf{r}}^*$, dehomogenize $\tilde{\mathbf{r}}^*$
 - 7: $\mathbf{R}^* \leftarrow \text{reshape}(\mathbf{r}^*)$, reshape $\mathbf{r}^* \in \mathbb{R}^9$ to $\mathbf{R}^* \in \mathbb{R}^{3 \times 3}$
 - 8: **return** \mathbf{R}^* , return the globally optimal rotation
-

is made from a homogeneous transformation matrix applied to a copy of the target data. This will ensure the index i of each point in each point cloud will be true correspondences even when transformation. The homogeneous transformation matrix chosen is

$$\mathbf{T}_{\text{Source}}^{\text{Target}} = \begin{bmatrix} \mathbf{R}_z(\pi/4) & \mathbf{t}_x(1) \\ \mathbf{0}_{1 \times 3} & 1 \end{bmatrix} \in \mathbb{R}^{4 \times 4} \quad (6.34)$$

where $\mathbf{R}_z(\pi/4) \in \mathbb{R}^{3 \times 3}$ is the rotation matrix for a rotation of $\pi/4 = 45$ deg about the z -axis, $\mathbf{t}_x(1) \in \mathbb{R}^3$ is a translation along the x -axis of 1 and $\mathbf{0}_{1 \times 3} = [0, 0, 0]$. The target and synthetic source data can be seen in Fig. 6.3(b) and Fig. 6.3(a) respectively.



(a) The target PC generated from sampling 1000 points from the CAD model.

(b) The synthetic source data based on the target data, but transformed $\mathbf{T}_{\text{Source}}^{\text{Target}}$.

Fig. 6.3: 3D plots showing the synthetic source data and target data.

On these points clouds GNC+RCQP are applied over 20 experiments with varying outlier percentages $\alpha = [10\%, 20\%, \dots, 90\%]$.

Once results are found, the method is applied to the sampled data shown in Fig. 6.1(a). This however includes the solving of the CP by finding feature correspondences between the point cloud. Due to self-collisions during

the sampling process, a statistical outlier filter was applied with the number of neighbors n_{nb} being 1.000 and the standard deviation ratio σ being 0.5.

Using FPFH it was unfortunately found that the source data did not contain enough information to find a satisfactory number of feature matches with the target data for GNC+RCQP to function. This was found by sampling target data with a varying number of data points uniformly distributed while computing the number of feature matches with the sampled source data. These results can be seen in Fig. 6.4, where the number of target data points sampled are $\gamma = [100, 200, \dots, 900, 1000, 2000, \dots, 50000]$ and the largest number of feature matches show to be two, which is far from sufficient. Filtering the sampled source data did not increase the number of feature matches as shown in the figure.

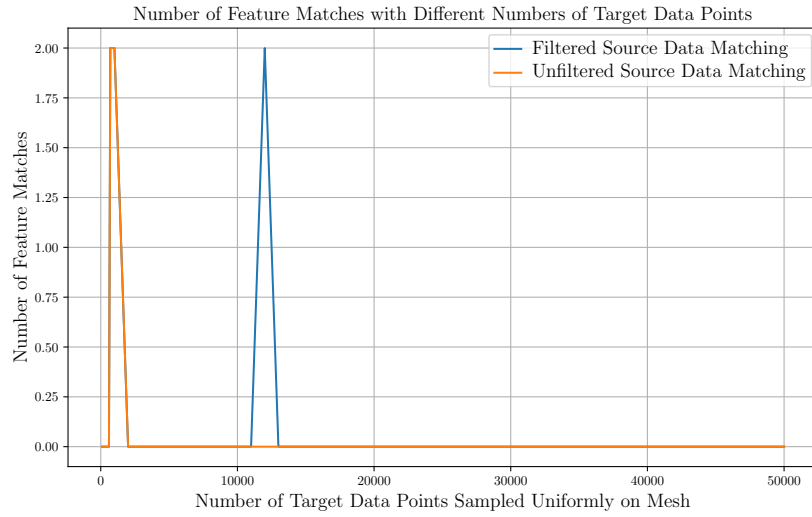


Fig. 6.4: Number of feature matches between target data containing γ data points and the sampled source data, both filtered and unfiltered.

6.4 Results

6.4.1 Pose Estimation Performance Data

Using the synthetic data source data, the number of iterations for each outlier percentage can be seen in Fig. 6.5, Fig. 6.6 shows the execution times for each outlier percentage, Fig. 6.7 shows the estimated orientation error as the angle θ_e being the angle in Equivalent Angle Axis (EAA) format. Finally in Fig. 6.8 the translational error is shown in.

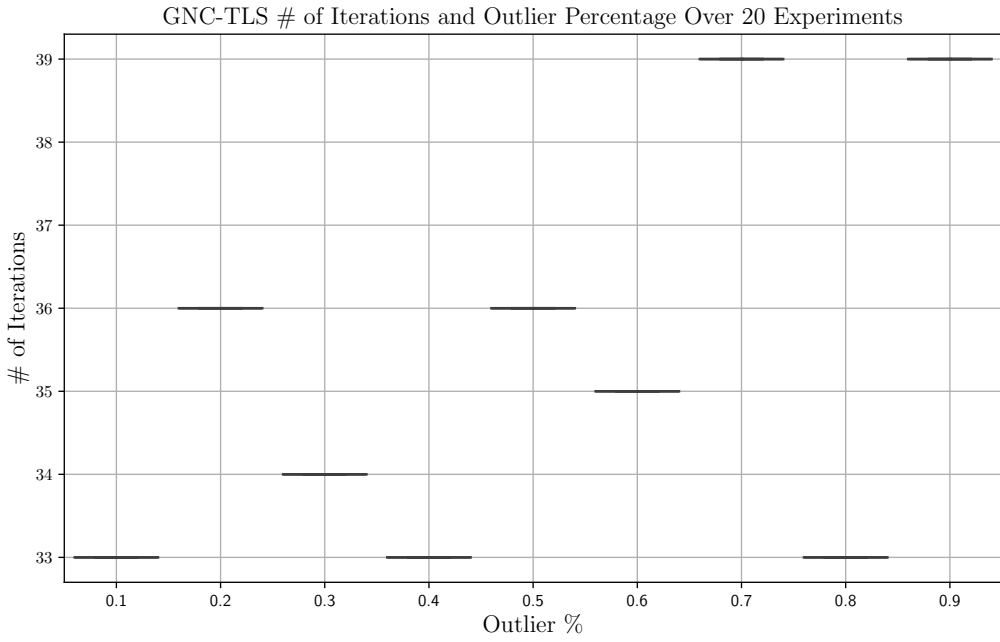


Fig. 6.5: Cost function for the TLS with

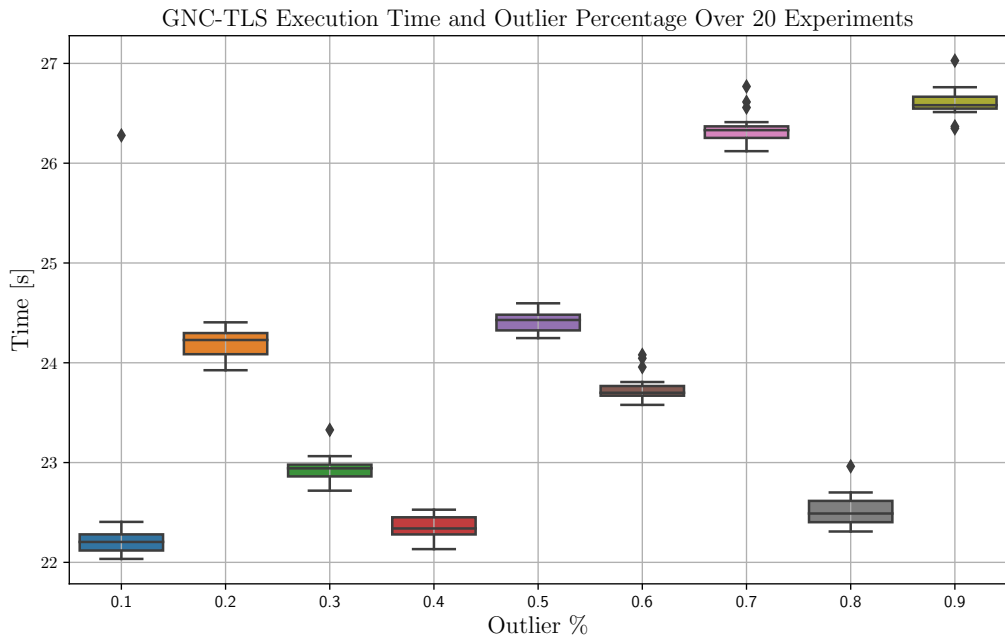


Fig. 6.6: Cost function for the TLS with

6.4.2 Weight Convergence Data

In Fig. 6.9 the weight history is shown for a single run with 10 % outliers, meaning how each weight entry changes value for each outer loop iteration. It can here be seen that the weight tends to converge either to 0 or 1 as one

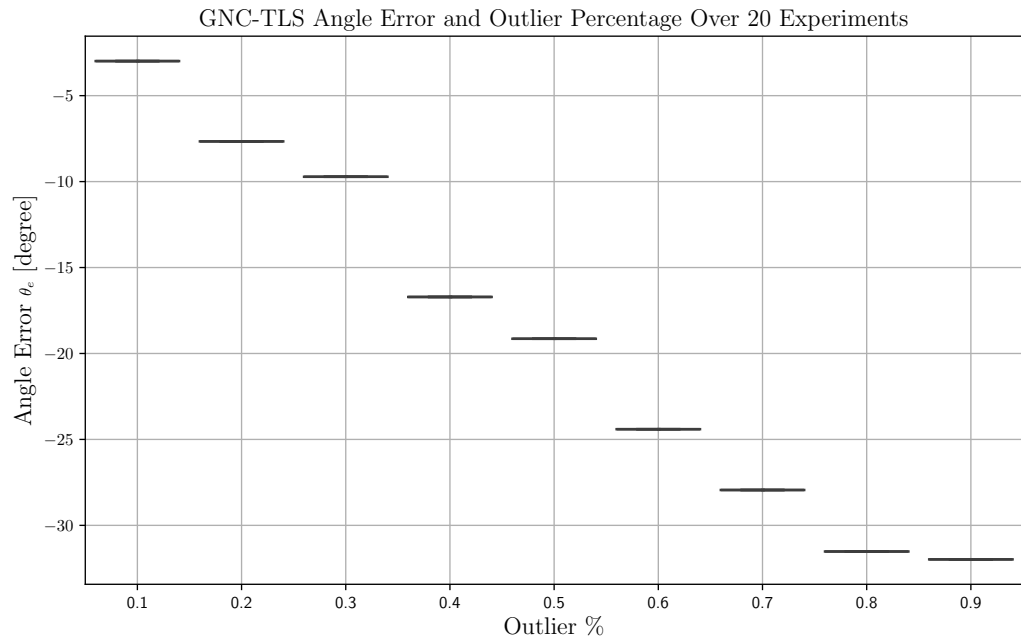


Fig. 6.7: Cost function for the TLS with

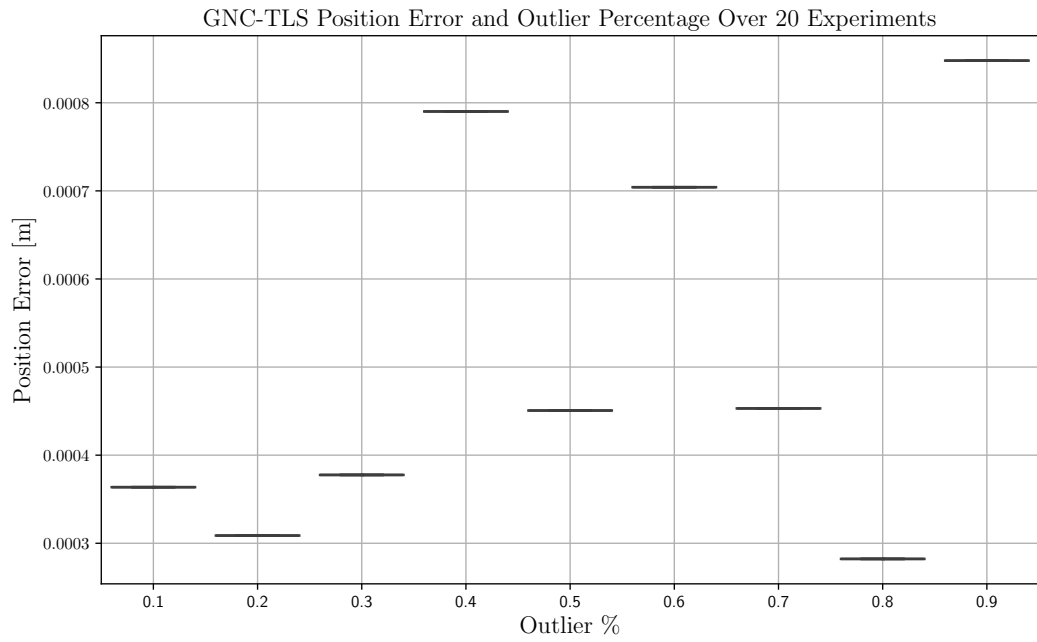


Fig. 6.8: Cost function for the TLS with

would come to expect.

Fig. 6.10 show the number of non-zero entries for 20 experiments with 10 % outliers.

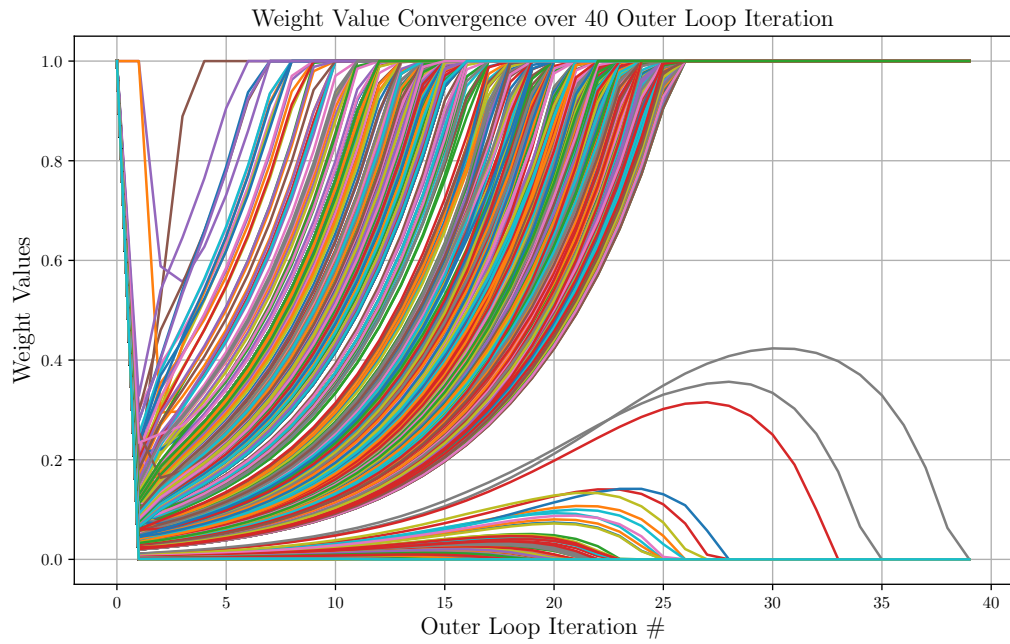


Fig. 6.9: Cost function for the TLS with

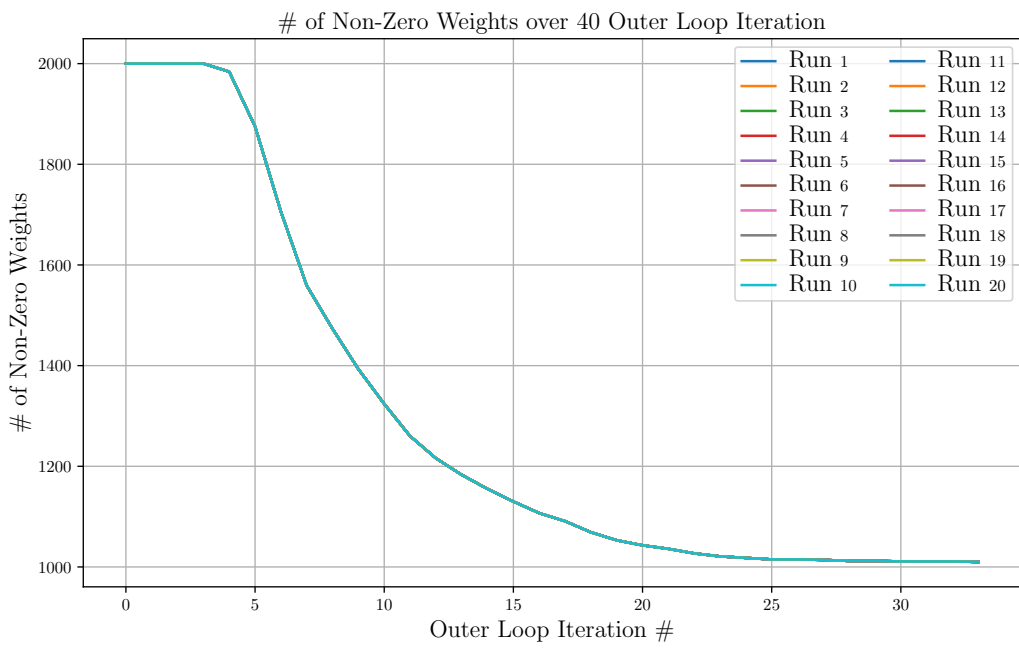


Fig. 6.10: Cost function for the TLS with

6.5 Discussion & Conclusion

The obtained results demonstrate the effectiveness of the GNC+RCQP method for pose estimation when applied to synthetic data. However, when dealing with sampled data, the methods faced challenges due to the lack of discernible features. One of the main difficulties encountered was the inability to identify a sufficient number of feature correspondences. This limitation can be attributed to the sparsity of the point cloud, indicating the need for intelligent probing techniques to enhance feature detection.

In the case of synthetic data, the pose estimation problem was successfully solved with satisfactory results for orientation estimation, even in the presence of a 10 % outlier percentage. However, as the outlier percentage increased to 20 %, the angle error reached -7.66° , failing to meet the desired success criteria. This trend persisted for higher outlier ratios as well.

The weight convergence analysis revealed an expected trend of convergence towards 0 and 1. However, the specific values at which the weights converged require further investigation and explanation. For example, in the case of a 10 % outlier scenario, the expected outcome would be the convergence of the number of non-zero weights to 900. Detailed graphs illustrating the weight convergence results can be found in Appendix C.

In summary, the GNC+RCQP method exhibited promising performance in pose estimation for synthetic data. However, challenges arose when working with sampled data, emphasizing the need for improved feature detection techniques. The angle error increased with higher outlier percentages, suggesting the importance of robustness in handling outliers. Further analysis is required to understand the convergence values of the weights and refine the pose estimation algorithm accordingly.

Chapter 7

In-Hand Manipulation

The goal of this chapter is to analyze the performance of the reinforcement learning-based manipulation algorithm Demo Augmented Policy Gradient (DAPG), which employs IL to constrain the algorithm's search space when solving the relocation task. The relocation task requires the robot hand to pick up an object and move it to a target location.

The analysis will focus on the relevant metrics from the training process as well as the final models performance.

DAPG was chosen as the algorithm from [124], due to it showing the best performance when solving the relocation task.

Firstly, the DAPG method is presented and described, followed by the setup for collecting the data used for training. The results are then presented and finally, the findings are discussed and concluded.

The simulation is done using a Adroit Hand (AH) [140] in the dynamic simulator MuJoCo [141]. The hand is thus equipped with 30 controllable parameters, 24 for the hand's joints and 6 for the hand's position $\mathbf{p}_{hnd} = [p_x, p_y, p_z]$ and orientation $\mathbf{o} = [\phi, \theta, \psi]$ in Roll-Pitch-Yaw (RPY) format. These make up the agent's actions a , while the states s also include the position of the prop when performing the relocation task.

7.1 Method

7.1.1 Demo Augmented Policy Gradient

The DAPG is an approach that expands on the Natural Policy Gradient (NPG) by introducing a demonstration term to weigh the gradient by λ_0 and λ_1 , which are hyperparameters to determine the advantage of state-action pair in demonstrations.

The parameter update rule to gain θ_{k+1} can be written as

$$\theta_{k+1} = \theta_k + \sqrt{\frac{\delta}{g^\top F_{\theta_k}^{-1} g}} F_{\theta_k}^{-1} g, \quad (7.1)$$

where F_{θ_k} is the Fisher Information Matrix (FIM), g is the gradient, δ is the step size, and θ_k is the previous weights.

The objective function is thus formulated as

$$g_{aug} = \sum_{(s,a) \in \rho_{\pi_\theta}} \nabla_\theta \ln \pi_\theta(a|s) A^{\pi_\theta}(s,a) + \sum_{(s,a) \in \rho_{\pi_D}} \nabla_\theta \ln \pi_\theta(a|s) \lambda_0 \lambda_1^k \quad (7.2)$$

Here ρ_{π_θ} is the occupancy measure, which is the probability of ending up in a state action tuple i.e. (s,a) , ∇_θ is the derivative operator in terms of θ , π_θ is the policy under the parameters θ , A^{π_θ} is the advantage function which tells the advantage gained by performing each action $\{a_1, a_2, \dots, a_{n_a}\}$, where n_a is the number of actions in the current state, compared to the expected return from taking the currently best action [142]. Finally, ρ_{π_D} is the occupancy function from the demonstrations.

7.1.2 Data Collection Procedure

To train DAPG, raw video data of expert demonstrations of the relocation task is collected. While [124] provides data for additional tasks i.e. *pour* and *place inside*, these are not of interest in this chapter. The objects used are from the YCB dataset [143] and the demonstrations were recorded by two RGBD cameras.

The collected data are then parsed to a multi-state pipeline including 3D pose estimation, that being for both the object of interest and the hand and demonstration translation.

Object Pose Estimation

The 6-DOF object poses in the physical setup is found using the PVN3D model, which is a deep learning-based pose estimation model, trained on the YCB data set.

The 6-DOF object pose is afterward optimized by minimizing the Perspective-n-Point (PnP) matching error.

Hand Pose Estimation

The hand pose is found using the deep learning-based pose estimation model MANO [144], which produces three parameters to represent the hand's pose: θ_t, β_t and r_t . θ_t refers to the 3D rotations of 15 joints, β_t is the shape parameters and r_t is the hand root's global pose. These can be combined through hand kinematics to compute the 3D angle of each hand joint

$$\mathbf{q}_t^{3d} = \mathbf{J}(\theta_t, \beta_t, r_t) \quad (7.3)$$

By utilizing off-the-shelf skin segmentation techniques such as Combinatorial Color Space Models [145] and hand detection models on video data, a hand mask M_t is extracted. M_t is overlayed the depth channel of the recorded data and the center of which is the used estimate of r_t . From the video data, the RGB channels are additionally parsed to a MANO which estimates 2D hand joint angles \mathbf{q}_t^{2D} , along with the hand parameters (θ_t, β_t, r_t) . Having the cameras poses $\mathbf{\Pi}$ enables the formulation of an optimization problem to determine the optimal (θ_t, β_t, r_t) i.e. $(\theta_t^*, \beta_t^*, r_t^*)$

$$\theta_t^*, \beta_t^*, r_t^* = \arg \min_{\theta_t, \beta_t, r_t} \|\mathbf{\Pi}\mathbf{J}(\theta_t, \beta_t, r_t) - \mathbf{q}_t^{2d}\|^2 + \lambda \|M_t (\mathbf{R}(\theta_t, \beta_t, r_t) - D_t)\|^2 \quad (7.4)$$

Here $\lambda = 0.001$ is a hyperparameter, \mathbf{R} is a depth rendering function and D_t is the corresponding depth map in frame t .

Demonstration Translation

Demonstration translation involves transforming the actions performed by the expert agent with one kinematic structure to a ML agent with some other set of actions. This is essential as, while the kinematic structure between the biological human hand and the anthropomorphic robot hand is similar, they are not identical. The similarity can be seen in the hands' kinematic trees in Appendix A.1 with their ROMs in Appendix A.1 and Appendix A.2.

This process requires two components: hand motion retargeting and Predicting robot action. The hand motion retargeting attempts to align the human hand motion to the robot hand motion, which due to the difference in kinematics is non-trivial as mentioned above. The prediction robot action attempts to estimate the torque necessary for each robot motor to recover the action from only pose estimation results.

The hand motion retargeting is solved using Task Space Vector (TSV)s to describe the optimization problem

$$\mathbf{q}_t^* = \min_{\mathbf{q}_t} \sum_{i=1}^N \|\mathbf{v}_i^{hum}(\theta_t, \beta_t, r_t) - \mathbf{v}_i^{rob}(\mathbf{q}_t)\|^2 + \alpha \|\mathbf{q}_t - \mathbf{q}_{t-1}\|^2. \quad (7.5)$$

Here $v_i^{hum}(\theta_t, \beta_t, r_t)$ computes the i 'th TSV to the finger tip and middle of the human hand, and the robot's forward kinematics function $v_i^{rob}(\mathbf{q})$ computes the i 'th TSV to the fingertip and middle of the robot hand. The TSVs can be seen illustrated in Fig. 7.1 from the hand root (marked with red) to the finger middle (marked with blue) and tip (marked with green) on the anthropomorphic robot hand.

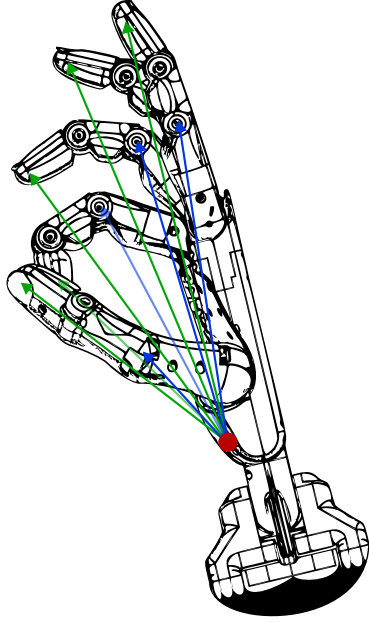


Fig. 7.1: The TSVs from the hand root (marked with red) to the finger middle (marked with blue) and tip (marked with green) on the anthropomorphic robot hand.

The optimization problem was solved using Sequential Least-Squares Quadratic Programming (SLSQP) with $\alpha = 8e - 3$.

The robot action estimation is achieved through the model $\mathbf{q}(t)$ presented in [146], which fulfills the criteria of zero jerk i.e. $\mathbf{q}'''(t) \approx 0$. The model enables $\mathbf{q}'(t)$ and $\mathbf{q}''(t)$ which through inverse dynamics can be converted to torques τ

$$\tau = f_{inv}(\mathbf{q}(t), \mathbf{q}'(t), \mathbf{q}''(t)) \quad (7.6)$$

The zero jerk here enables behavior similar to that of a human, which in turn leads to more natural robot motion, as well as ensuring low joint position errors for motors and limiting excessive wear on the physical robot.

7.2 Experimental Setup

To train and test the DAPG algorithm, the mug shown in Fig. ?? is chosen as the prop. Additionally, to remain consistent with the original paper [124] the number of training iterations was 2.000 with demonstration hyper parameters λ_0 and λ_1 being 0.1 and 0.99 respectively. Furthermore, the learning rate α_{lr} was set to 1.0, the step size δ was set to 0.1 and the discount factor γ was 0.995.

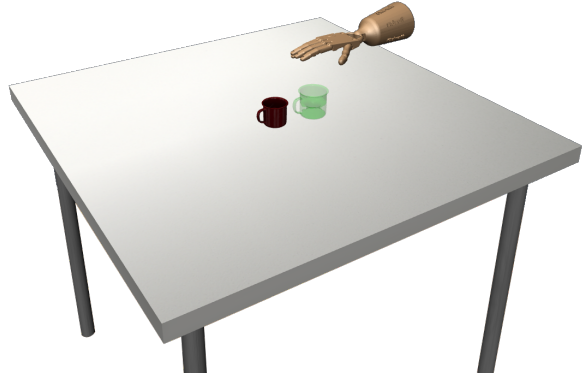
To execute the relocation task, the object is placed on a table and a goal is defined at a random location marked with green silhouette. The experimental setup can be seen in Fig. 7.2(b).

7.3 Results

The improvement in the surrogate objective function after the policy update



(a) The mug prop from YCB [143] chosen for training.



(b) The experimental setup used when training the DAPG algorithm. The figure contains the table platform, the mug prop, the simulated anthropomorphic hand and the goal mug position marked as a green silhouette.

Fig. 7.2: The mug prop used for training and the experimental setup.

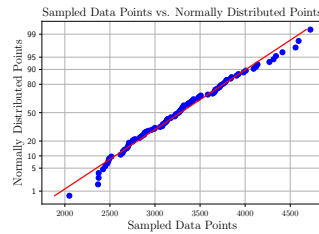


Fig. 7.3: The TSVs from the hand root (marked with red) to the finger middle (marked with blue) and tip (marked with green) on the anthropomorphic robot hand.

7.4 Discussion & Conclusion

Chapter 8

Discussion

Chapter 9

Conclusion

this is the conclusion

Bibliography

- [1] El Zaatari, Shirine et al. “Cobot programming for collaborative industrial tasks: An overview”. In: *Robotics and Autonomous Systems* 116 (June 2019), pp. 162–180. doi: [10.1016/j.robot.2019.03.003](https://doi.org/10.1016/j.robot.2019.03.003).
- [2] *What is computer vision?* <https://www.ibm.com/topics/computer-vision>. Accessed: 2022-11-02.
- [3] Zimmer, Henning. “Correspondence problems in computer vision”. PhD thesis. Jan. 2012.
- [4] LeCun, Yann, Bengio, Yoshua, and Hinton, Geoffrey. “Deep learning”. In: *Nature* 521.7553 (May 2015), pp. 436–444. issn: 1476-4687. doi: [10.1038/nature14539](https://doi.org/10.1038/nature14539). url: <https://doi.org/10.1038/nature14539>.
- [5] Monkman, Gareth J. et al. “Robot Grippers”. PhD thesis. Jan. 2004, pp. 5–6.
- [6] Mihelj, Matjaž et al. “Robotics Second Edition”. PhD thesis. Jan. 2019, p. 1.
- [7] Szeliski, Richard. *Computer vision: algorithms and applications*. Springer Nature, 2022, p. 284.
- [8] Quigley, Morgan et al. “ROS: an open-source Robot Operating System”. In: *ICRA Workshop on Open Source Software* 3 (Jan. 2009).
- [9] Publications, United Nations. “Inequality in Asia and the Pacific in the Era of the 2030 Agenda for Sustainable Development”. In: 2018. url: <https://www.unescap.org/publications/inequality-asia-and-pacific-era-2030-agenda-sustainable-development>.
- [10] Wenwen, Shi et al. “Analysis and Control of Human Error”. In: *Procedia Engineering* 26 (Dec. 2011), pp. 2126–2132. doi: [10.1016/j.proeng.2011.11.2415](https://doi.org/10.1016/j.proeng.2011.11.2415).
- [11] Galin, Rinat et al. “Cobots and the benefits of their implementation in intelligent manufacturing”. In: *IOP Conference Series: Materials Science and Engineering* 862 (May 2020), p. 032075. doi: [10.1088/1757-899X/862/3/032075](https://doi.org/10.1088/1757-899X/862/3/032075).
- [12] Raptopoulos, Fredy, Koskinopoulou, Maria, and Maniadakis, Michail. “Robotic Pick-and-Toss Facilitates Urban Waste Sorting”. In: *2020 IEEE 16th International Conference on Automation Science and Engineering (CASE)*. 2020, pp. 1149–1154. doi: [10.1109/CASE48305.2020.9216746](https://doi.org/10.1109/CASE48305.2020.9216746).
- [13] Talpur, Mir Sajjad Hussain and Shaikh, Murtaza Hussain. *Automation of Mobile Pick and Place Robotic System for Small Food Industry*. 2012. doi: [10.48550/ARXIV.1203.4475](https://arxiv.org/abs/1203.4475). url: <https://arxiv.org/abs/1203.4475>.
- [14] Yamanaka, Yuta et al. “Development of a Food Handling Soft Robot Hand Considering a High-speed Pick-and-place Task”. In: *2020 IEEE/SICE International Symposium on System Integration (SII)*. 2020, pp. 87–92. doi: [10.1109/SII46433.2020.9026282](https://doi.org/10.1109/SII46433.2020.9026282).
- [15] Lee, Sukhan and Lee, Yeonho. “Real-Time Industrial Bin-Picking with a Hybrid Deep Learning-Engineering Approach”. In: *2020 IEEE International Conference on Big Data and Smart Computing (BigComp)*. 2020, pp. 584–588. doi: [10.1109/BigComp48618.2020.00015](https://doi.org/10.1109/BigComp48618.2020.00015).
- [16] Mnyusiwalla, Hussein et al. “A Bin-Picking Benchmark for Systematic Evaluation of Robotic Pick-and-Place Systems”. In: *IEEE Robotics and Automation Letters* 5.2 (2020), pp. 1389–1396. doi: [10.1109/LRA.2020.2965076](https://doi.org/10.1109/LRA.2020.2965076).
- [17] Wong, Ching-Chang et al. “Generic Development of Bin Pick-and-Place System Based on Robot Operating System”. In: *IEEE Access* 10 (2022), pp. 65257–65270. doi: [10.1109/ACCESS.2022.3182114](https://doi.org/10.1109/ACCESS.2022.3182114).

- [18] He, Zaixing et al. “6D Pose Estimation of Objects: Recent Technologies and Challenges”. In: *Applied Sciences* 11.1 (2021). ISSN: 2076-3417. doi: 10.3390/app11010228. URL: <https://www.mdpi.com/2076-3417/11/1/228>.
- [19] .., Taryudi and Wang, Ming-Shyan. “3D object pose estimation using stereo vision for object manipulation system”. In: May 2017, pp. 1532–1535. doi: 10.1109/ICASI.2017.7988217.
- [20] Oh, Jong-Kyu, Lee, Sukhan, and Lee, Chan-Ho. “Stereo vision based automation for a bin-picking solution”. In: *International Journal of Control, Automation and Systems* 10.2 (Apr. 2012), pp. 362–373. ISSN: 2005-4092. doi: 10.1007/s12555-012-0216-9. URL: <https://doi.org/10.1007/s12555-012-0216-9>.
- [21] Abdelaal, Mahmoud et al. “Uncalibrated stereo vision with deep learning for 6-DOF pose estimation for a robot arm system”. In: *Robotics and Autonomous Systems* 145 (2021), p. 103847. ISSN: 0921-8890. doi: <https://doi.org/10.1016/j.robot.2021.103847>. URL: <https://www.sciencedirect.com/science/article/pii/S0921889021001329>.
- [22] Nakano, Yoshihiro. “Stereo Vision Based Single-Shot 6D Object Pose Estimation for Bin-Picking by a Robot Manipulator”. In: *CoRR* abs/2005.13759 (2020). arXiv: 2005.13759. URL: <https://arxiv.org/abs/2005.13759>.
- [23] Kozák, Viktor et al. “Data-Driven Object Pose Estimation in a Practical Bin-Picking Application”. In: *Sensors* 21.18 (2021). ISSN: 1424-8220. doi: 10.3390/s21186093. URL: <https://www.mdpi.com/1424-8220/21/18/6093>.
- [24] Xu, Chi et al. “6DoF Pose Estimation of Transparent Object from a Single RGB-D Image”. In: *Sensors* 20.23 (2020). ISSN: 1424-8220. doi: 10.3390/s20236790. URL: <https://www.mdpi.com/1424-8220/20/23/6790>.
- [25] Straszheim, Troy et al. *Shadow Robot*. URL: <https://www.shadowrobot.com/dexterous-hand-series/>. (accessed: 29.07.2022).
- [26] Koenig, N. and Howard, A. “Design and use paradigms for Gazebo, an open-source multi-robot simulator”. In: 3 (2004), 2149–2154 vol.3. doi: 10.1109/IROS.2004.1389727.
- [27] Robotics, Shadow. *Shadow Robotics*. URL: <https://www.shadowrobot.com/>.
- [28] Robotics, Shadow. *The Shadow Robot Company*. URL: <https://github.com/shadow-robot>.
- [29] Dimensions. https://shadow-robot-company-dexterous-hand.readthedocs-hosted.com/en/latest/user_guide/md_dimensions.html. Accessed: 2023-04-26.
- [30] Rahman, Akhlaqur and Al-Jumaily, Adel. “Design and Development of a Bilateral Therapeutic Hand Device for Stroke Rehabilitation”. In: *International Journal of Advanced Robotic Systems* 10.12 (2013), p. 405. doi: 10.5772/56809. eprint: <https://doi.org/10.5772/56809>. URL: <https://doi.org/10.5772/56809>.
- [31] Bones Of The Hand. <https://freesvg.org/bones-of-the-hand>. Accessed: 2023-04-26.
- [32] Robotics, Shadow. *Gazebo*. URL: %5Curl%7Bhttps://shadow-robot-company-dexterous-hand.readthedocs-hosted.com/en/latest/user_guide/sim_gazebo.html%7D.
- [33] docker. *What is a container*. URL: <https://www.docker.com/resources/what-container/>.
- [34] First time users. https://shadow-robot-company-dexterous-hand.readthedocs-hosted.com/en/latest/user_guide/sd_first_time_users.html. Accessed: 2023-04-26.
- [35] Straszheim, Troy et al. *Conceptual overview of ROS catkin*. URL: %5Curl%7Bhttp://wiki.ros.org/catkin/conceptual_overview%7D
- [36] Beek, Bas van et al. *About Us*. URL: %5Curl%7B<https://numpy.org/%7D>

- [37] team, OpenCV. *OpenCV*. URL: %5Curl%7Bhttps://opencv.org/%7D.
- [38] Carroll, Michael. *dynamic-reconfigure*. URL: %5Curl%7Bhttp://google.com%7D.
- [39] Coleman, David et al. *Reducing the Barrier to Entry of Complex Robotic Software: a MoveIt! Case Study*. 2014. arXiv: 1404.3785 [cs.RO].
- [40] Sucan, Ioan A., Moll, Mark, and Kavraki, Lydia E. “The Open Motion Planning Library”. In: *IEEE Robotics & Automation Magazine* 19.4 (Dec. 2012). <https://ompl.kavrakilab.org>, pp. 72–82. doi: 10.1109/MRA.2012.2205651.
- [41] Chitta, Sachin et al. “ros_control: A generic and simple control framework for ROS”. In: *The Journal of Open Source Software* (2017). doi: 10.21105/joss.00456. URL: <http://www.theoj.org/joss-papers/joss.00456/10.21105.joss.00456.pdf>.
- [42] Robotics, Shadow. *Control Description*. URL: %5Curl%7Bhttps://shadow-robot-company-dexterous-hand.readthedocs-hosted.com/en/latest/user_guide/ed_control_description.html%7D.
- [43] Robotics, Shadow. *Firmware*. URL: %5Curl%7Bhttps://shadow-robot-company-dexterous-hand.readthedocs-hosted.com/en/latest/user_guide/sd_firmware.html%7D.
- [44] Robotics, Shadow. *Controlling the Hand 2*. URL: %5Curl%7Bhttps://shadow-robot-company-dexterous-hand.readthedocs-hosted.com/en/latest/user_guide/sd_controloing_hand.html%7D.
- [45] Staven, Victor Melbye. *in_hand_pose_estimation*. URL: %5Curl%7Bhttps://github.com/vmstavens/in_hand_pose_estimation%7D.
- [46] Staven, Victor Melbye. *ros_utils*. URL: %5Curl%7Bhttps://github.com/vmstavens/ros_utils%7D.
- [47] Pérez-González, Antonio et al. “A modified elastic foundation contact model for application in 3D models of the prosthetic knee”. In: *Medical Engineering & Physics* 30.3 (2008), pp. 387–398. ISSN: 1350-4533. doi: <https://doi.org/10.1016/j.medengphy.2007.04.001>. URL: <https://www.sciencedirect.com/science/article/pii/S1350453307000616>.
- [48] Hertz, H. “On the Contact of Rigid Elastic Solids and on Hardness”. In: *Ch 6: Assorted Papers* (1882).
- [49] Bruno Siciliano, Oussama Khatib, ed. *Springer Handbook of Robotics*. Springer Berlin, Heidelberg, 2016.
- [50] Xydas, Nicholas and Kao, Imin. “Modeling of Contact Mechanics and Friction Limit Surfaces for Soft Fingers in Robotics, with Experimental Results”. In: *The International Journal of Robotics Research* 18.9 (1999), pp. 941–950. doi: 10.1177/02783649922066673. eprint: <https://doi.org/10.1177/02783649922066673>. URL: <https://doi.org/10.1177/02783649922066673>.
- [51] Yuvaraj, S., Malayalamurthi, R., and Raja, K. Venkatesh. “The haptic and perceptual characteristics of an anthropomorphic curved soft finger structure”. In: *Curved and Layered Structures* 6.1 (2019), pp. 161–168. doi: [doi:10.1515/cls-2019-0013](https://doi.org/10.1515/cls-2019-0013). URL: <https://doi.org/10.1515/cls-2019-0013>.
- [52] Howe, R.D., Kao, I., and Cutkosky, M.R. “The sliding of robot fingers under combined torsion and shear loading”. In: *Proceedings. 1988 IEEE International Conference on Robotics and Automation*. 1988, 103–105 vol.1. doi: 10.1109/ROBOT.1988.12032.
- [53] Flugge, Wilhelm. *Viscoelasticity*. Blaisdell Publishing Company, Waltham, MA, 1967.
- [54] Maxwell, James Clerk. *On the dynamical theory of gases*. Royal Society, 1867.
- [55] Fung, Yuan-Cheng. “Mechanical properties and active remodeling of blood vessels”. In: *Biomechanics*. Springer, 1993.

- [56] Tiezzi, Paolo and Kao, Imin. “Modeling of Viscoelastic Contacts and Evolution of Limit Surface for Robotic Contact Interface”. In: *Robotics, IEEE Transactions on* 23 (May 2007), pp. 206–217. doi: [10.1109/TRO.2006.889494](https://doi.org/10.1109/TRO.2006.889494).
- [57] Tiezzi, P. and Kao, I. “Characteristics of contact and limit surface for viscoelastic fingers”. In: *Proceedings 2006 IEEE International Conference on Robotics and Automation, 2006. ICRA 2006.* 2006, pp. 1365–1370. doi: [10.1109/ROBOT.2006.1641899](https://doi.org/10.1109/ROBOT.2006.1641899).
- [58] Tiezzi, Paolo, Kao, Imin, and Vassura, G. “Effect of layer compliance on frictional behavior of soft robotic fingers”. In: *Advanced Robotics* 21 (Oct. 2007), pp. 1653–1670. doi: [10.1163/156855307782227390](https://doi.org/10.1163/156855307782227390).
- [59] Kalker, J. J. “On the Contact Problem in Elastostatics”. In: *Unilateral Problems in Structural Analysis*. Ed. by Del Piero, Gianpietro and Maceri, Franco. Vienna: Springer Vienna, 1985, pp. 81–85. ISBN: 978-3-7091-2632-.
- [60] Kozhevnikov, I.F. et al. “A new algorithm for computing the indentation of a rigid body of arbitrary shape on a viscoelastic half-space”. In: *International Journal of Mechanical Sciences* 50.7 (2008), pp. 1194–1202. ISSN: 0020-7403. doi: <https://doi.org/10.1016/j.ijmecsci.2008.04.003>. URL: <https://www.sciencedirect.com/science/article/pii/S0020740308000623>.
- [61] Marmo, Francesco and Rosati, Luciano. “A General Approach to the Solution of Boussinesq’s Problem for Polynomial Pressures Acting over Polygonal Domains”. In: *Journal of Elasticity* 122.1 (Jan. 2016), pp. 75–112. ISSN: 1573-2681. doi: [10.1007/s10659-015-9534-5](https://doi.org/10.1007/s10659-015-9534-5). URL: <https://doi.org/10.1007/s10659-015-9534-5>.
- [62] Li, Junshan and Berger, Edward J. “A Boussinesq–Cerruti Solution Set for Constant and Linear Distribution of Normal and Tangential Load over a Triangular Area”. In: *Journal of elasticity and the physical science of solids* 63.2 (May 2001), pp. 137–151. ISSN: 1573-2681. doi: [10.1023/A:1014013425423](https://doi.org/10.1023/A:1014013425423). URL: <https://doi.org/10.1023/A:1014013425423>.
- [63] Wasko, Wojciech et al. “Contact Modelling and Tactile Data Processing for Robot Skins”. In: *Sensors* 19.4 (2019). ISSN: 1424-8220. doi: [10.3390/s19040814](https://doi.org/10.3390/s19040814). URL: <https://www.mdpi.com/1424-8220/19/4/814>.
- [64] Slaughter, William S. *The Linearized Theory of Elasticity*. Springer, 2012.
- [65] Hills, D., Nowell, D., and Barber, James. “KL Johnson and contact mechanics”. In: *Proceedings of the Institution of Mechanical Engineers, Part C: Journal of Mechanical Engineering Science* 231 (Feb. 2016). doi: [10.1177/0954406216634121](https://doi.org/10.1177/0954406216634121).
- [66] Lee, S.Y., Kuo, Y.H., and Lin, F.Y. “Stability of a Timoshenko beam resting on a Winkler elastic foundation”. In: *Journal of Sound and Vibration* 153.2 (1992), pp. 193–202. ISSN: 0022-460X. doi: [https://doi.org/10.1016/S0022-460X\(05\)80001-X](https://doi.org/10.1016/S0022-460X(05)80001-X). URL: <https://www.sciencedirect.com/science/article/pii/S0022460X0580001X>.
- [67] Eisenberger, M. and Clastornik, J. “Vibrations and buckling of a beam on a variable winkle elastic foundation”. In: *Journal of Sound and Vibration* 115.2 (1987), pp. 233–241. ISSN: 0022-460X. doi: [https://doi.org/10.1016/0022-460X\(87\)90469-X](https://doi.org/10.1016/0022-460X(87)90469-X). URL: <https://www.sciencedirect.com/science/article/pii/0022460X8790469X>.
- [68] Fregly, Benjamin J., Bei, Yanhong, and Sylvester, Mark E. “Experimental evaluation of an elastic foundation model to predict contact pressures in knee replacements”. In: *Journal of Biomechanics* 36.11 (2003), pp. 1659–1668. ISSN: 0021-9290. doi: [https://doi.org/10.1016/S0021-9290\(03\)00176-3](https://doi.org/10.1016/S0021-9290(03)00176-3). URL: <https://www.sciencedirect.com/science/article/pii/S0021929003001763>.

- [69] Kao, Imin and Cutkosky, Mark R. “Quasistatic Manipulation with Compliance and Sliding”. In: *The International Journal of Robotics Research* 11.1 (1992), pp. 20–40. doi: 10.1177/027836499201100102. eprint: <https://doi.org/10.1177/027836499201100102>. url: <https://doi.org/10.1177/027836499201100102>.
- [70] Howe, Robert D. and Cutkosky, Mark R. “Practical Force-Motion Models for Sliding Manipulation”. In: *The International Journal of Robotics Research* 15.6 (1996), pp. 557–572. doi: 10.1177/027836499601500603. eprint: <https://doi.org/10.1177/027836499601500603>. url: <https://doi.org/10.1177/027836499601500603>.
- [71] Kao, Imin and Yang, Fuqian. “Stiffness and Contact Mechanics for Soft Fingers in Grasping and Manipulation”. In: *Robotics and Automation, IEEE Transactions on* 20 (Mar. 2004), pp. 132–135. doi: 10.1109/TRA.2003.820868.
- [72] Ciocarlie, Matei, Lackner, Claire, and Allen, Peter. “Soft Finger Model with Adaptive Contact Geometry for Grasping and Manipulation Tasks”. In: *Second Joint EuroHaptics Conference and Symposium on Haptic Interfaces for Virtual Environment and Teleoperator Systems (WHC'07)*. 2007, pp. 219–224. doi: 10.1109/WHC.2007.103.
- [73] Sabat, Lovely and Kundu, Chinmay Kumar. “History of Finite Element Method: A Review”. In: *Recent Developments in Sustainable Infrastructure*. Ed. by Das, Bibhuti Bhushan et al. Singapore: Springer Singapore, 2021, pp. 395–404. ISBN: 978-981-15-4577-1.
- [74] Klocke, Fritz et al. “Examples of FEM application in manufacturing technology”. In: *Journal of Materials Processing Technology* 120.1 (2002), pp. 450–457. issn: 0924-0136. doi: [https://doi.org/10.1016/S0924-0136\(01\)01210-9](https://doi.org/10.1016/S0924-0136(01)01210-9). url: <https://www.sciencedirect.com/science/article/pii/S0924013601012109>.
- [75] Telliskivi, T and Olofsson, U. “Contact mechanics analysis of measured wheel-rail profiles using the finite element method”. In: *Proceedings of the Institution of Mechanical Engineers, Part F: Journal of Rail and Rapid Transit* 215.2 (2001), pp. 65–72. doi: 10.1243/0954409011531404. eprint: <https://doi.org/10.1243/0954409011531404>. url: <https://doi.org/10.1243/0954409011531404>.
- [76] Põdra, Priit and Andersson, Sören. “Simulating sliding wear with finite element method”. In: *Tribology International* 32.2 (1999), pp. 71–81. issn: 0301-679X. doi: [https://doi.org/10.1016/S0301-679X\(99\)00012-2](https://doi.org/10.1016/S0301-679X(99)00012-2). url: <https://www.sciencedirect.com/science/article/pii/S0301679X99000122>.
- [77] Pantuso, Daniel, Bathe, Klaus-Jürgen, and Bouzinov, Pavel A. “A finite element procedure for the analysis of thermo-mechanical solids in contact”. In: *Computers & Structures* 75.6 (2000), pp. 551–573. issn: 0045-7949. doi: [https://doi.org/10.1016/S0045-7949\(99\)00212-6](https://doi.org/10.1016/S0045-7949(99)00212-6). url: <https://www.sciencedirect.com/science/article/pii/S0045794999002126>.
- [78] Liang, Xiaodong, Ali, Mohammad Zawad, and Zhang, Huaguang. “Induction Motors Fault Diagnosis Using Finite Element Method: A Review”. In: *IEEE Transactions on Industry Applications* 56.2 (2020), pp. 1205–1217. doi: 10.1109/TIA.2019.2958908.
- [79] Ye, Zhiqiu et al. “Soft Robot Skin With Conformal Adaptability for On-Body Tactile Perception of Collaborative Robots”. In: *IEEE Robotics and Automation Letters* (Mar. 2022), pp. 1–1. doi: 10.1109/LRA.2022.3155225.
- [80] Lu, Guan, Fu, Shiwen, and Xu, Yiming. “Design and Experimental Research of Robot Finger Sliding Tactile Sensor Based on FBG”. In: *Sensors* 22.21 (2022). issn: 1424-8220. doi: 10.3390/s22218390. url: <https://www.mdpi.com/1424-8220/22/21/8390>.

- [81] Ciocarlie, M., Miller, A., and Allen, P. “Grasp analysis using deformable fingers”. In: *2005 IEEE/RSJ International Conference on Intelligent Robots and Systems*. 2005, pp. 4122–4128. doi: [10.1109/IROS.2005.1545525](https://doi.org/10.1109/IROS.2005.1545525).
- [82] Narang, Yashraj S. et al. “Sim-to-Real for Robotic Tactile Sensing via Physics-Based Simulation and Learned Latent Projections”. In: *CoRR* abs/2103.16747 (2021). arXiv: [2103.16747](https://arxiv.org/abs/2103.16747). URL: <https://arxiv.org/abs/2103.16747>.
- [83] Narang, Yashraj S. et al. “Interpreting and Predicting Tactile Signals via a Physics-Based and Data-Driven Framework”. In: *CoRR* abs/2006.03777 (2020). arXiv: [2006.03777](https://arxiv.org/abs/2006.03777). URL: <https://arxiv.org/abs/2006.03777>.
- [84] Sferrazza, Carmelo et al. “Ground Truth Force Distribution for Learning-Based Tactile Sensing: A Finite Element Approach”. In: *IEEE Access* PP (Nov. 2019), pp. 1–1. doi: [10.1109/ACCESS.2019.2956882](https://doi.org/10.1109/ACCESS.2019.2956882).
- [85] Calandra, Roberto et al. “More Than a Feeling: Learning to Grasp and Regrasp using Vision and Touch”. In: *CoRR* abs/1805.11085 (2018). arXiv: [1805.11085](https://arxiv.org/abs/1805.11085). URL: [http://arxiv.org/abs/1805.11085](https://arxiv.org/abs/1805.11085).
- [86] Spiers, Adam et al. “Single-Grasp Object Classification and Feature Extraction with Simple Robot Hands and Tactile Sensors”. In: *IEEE Transactions on Haptics* 9 (Jan. 2016), pp. 60–71. doi: [10.1109/TOH.2016.2521378](https://doi.org/10.1109/TOH.2016.2521378).
- [87] Higuera, Carolina, Boots, Byron, and Mukadam, Mustafa. *Learning to Read Braille: Bridging the Tactile Reality Gap with Diffusion Models*. 2023. arXiv: [2304.01182](https://arxiv.org/abs/2304.01182) [cs.R0].
- [88] Ruppel, Philipp et al. “Simulation of the SynTouch BioTac Sensor”. In: (2019). Ed. by Strand, Marcus et al., pp. 374–387.
- [89] Huang, Xiaoshui et al. *A comprehensive survey on point cloud registration*. 2021. arXiv: [2103.02690](https://arxiv.org/abs/2103.02690) [cs.CV].
- [90] Oberweger, Markus, Wohlhart, Paul, and Lepetit, Vincent. *Hands Deep in Deep Learning for Hand Pose Estimation*. 2016. arXiv: [1502.06807](https://arxiv.org/abs/1502.06807) [cs.CV].
- [91] Toshev, Alexander and Szegedy, Christian. “DeepPose: Human Pose Estimation via Deep Neural Networks”. In: *Computer Vision and Pattern Recognition*. 2014.
- [92] Mathis, Alexander et al. “DeepLabCut: markerless pose estimation of user-defined body parts with deep learning”. In: *Nature Neuroscience* 21.9 (Sept. 2018), pp. 1281–1289. ISSN: 1546-1726. doi: [10.1038/s41593-018-0209-y](https://doi.org/10.1038/s41593-018-0209-y). URL: <https://doi.org/10.1038/s41593-018-0209-y>.
- [93] Huang, Xiaoshui et al. “A Systematic Approach for Cross-Source Point Cloud Registration by Preserving Macro and Micro Structures”. In: *IEEE Transactions on Image Processing* 26.7 (2017), pp. 3261–3276. doi: [10.1109/TIP.2017.2695888](https://doi.org/10.1109/TIP.2017.2695888).
- [94] Huang, Xiaoshui et al. “A Coarse-to-Fine Algorithm for Matching and Registration in 3D Cross-Source Point Clouds”. In: *IEEE Transactions on Circuits and Systems for Video Technology* 28.10 (2018), pp. 2965–2977. doi: [10.1109/TCSVT.2017.2730232](https://doi.org/10.1109/TCSVT.2017.2730232).
- [95] Yang, Zhenpei et al. “Extreme Relative Pose Estimation for RGB-D Scans via Scene Completion”. In: June 2019, pp. 4526–4535. doi: [10.1109/CVPR.2019.00466](https://doi.org/10.1109/CVPR.2019.00466).
- [96] Wang, Lingjing et al. *Non-Rigid Point Set Registration Networks*. 2019. arXiv: [1904.01428](https://arxiv.org/abs/1904.01428) [cs.GR].
- [97] Huang, Xiaoshui, Mei, Guofeng, and Zhang, Jian. *Feature-metric Registration: A Fast Semi-supervised Approach for Robust Point Cloud Registration without Correspondences*. 2020. arXiv: [2005.01014](https://arxiv.org/abs/2005.01014) [cs.CV].
- [98] Zeng, Andy et al. *3DMatch: Learning Local Geometric Descriptors from RGB-D Reconstructions*. 2017. arXiv: [1603.08182](https://arxiv.org/abs/1603.08182) [cs.CV].

- [99] Deng, Haowen, Birdal, Tolga, and Ilic, Slobodan. *PPFNet: Global Context Aware Local Features for Robust 3D Point Matching*. 2018. arXiv: 1802.02669 [cs.CV].
- [100] Gojcic, Zan et al. *The Perfect Match: 3D Point Cloud Matching with Smoothed Densities*. 2019. arXiv: 1811.06879 [cs.CV].
- [101] Besl, Paul J. and McKay, Neil D. “A Method for Registration of 3-D Shapes”. In: *IEEE Trans. Pattern Anal. Mach. Intell.* 14 (1992), pp. 239–256.
- [102] Chen, Yang and Medioni, Gérard. “Object modelling by registration of multiple range images”. In: *Image and Vision Computing* 10.3 (1992). Range Image Understanding, pp. 145–155. issn: 0262-8856. doi: [https://doi.org/10.1016/0262-8856\(92\)90066-C](https://doi.org/10.1016/0262-8856(92)90066-C). url: <https://www.sciencedirect.com/science/article/pii/026288569290066C>.
- [103] Segal, Aleksandr, Hähnel, Dirk, and Thrun, Sebastian. “Generalized-ICP”. In: June 2009. doi: 10.15607/RSS.2009.V.021.
- [104] Shi, Xiaojing, Liu, Tao, and Han, Xie. “Improved Iterative Closest Point(ICP) 3D point cloud registration algorithm based on point cloud filtering and adaptive fireworks for coarse registration”. In: *International Journal of Remote Sensing* 41.8 (2020), pp. 3197–3220. doi: 10.1080/01431161.2019.1701211. eprint: <https://doi.org/10.1080/01431161.2019.1701211>. url: <https://doi.org/10.1080/01431161.2019.1701211>.
- [105] Zhu, Hao et al. “A Review of Point Set Registration: From Pairwise Registration to Groupwise Registration”. en. In: *Sensors (Basel)* 19.5 (Mar. 2019).
- [106] Livi, Lorenzo and Rizzi, Antonello. “The Graph Matching Problem”. In: *Pattern Anal. Appl.* 16.3 (Aug. 2013), pp. 253–283. issn: 1433-7541. doi: 10.1007/s10044-012-0284-8. url: <https://doi.org/10.1007/s10044-012-0284-8>.
- [107] Zhou, Feng and De la Torre, Fernando. “Factorized Graph Matching”. In: *IEEE Transactions on Pattern Analysis and Machine Intelligence* 38.9 (2016), pp. 1774–1789. doi: 10.1109/TPAMI.2015.2501802.
- [108] Leordeanu, Marius and Hebert, Martial. “A spectral technique for correspondence problems using pairwise constraints”. In: *Tenth IEEE International Conference on Computer Vision (ICCV'05) Volume 1 2* (2005), 1482–1489 Vol. 2.
- [109] Zass, Ron and Shashua, Amnon. “Probabilistic graph and hypergraph matching”. In: *2008 IEEE Conference on Computer Vision and Pattern Recognition*. 2008, pp. 1–8. doi: 10.1109/CVPR.2008.4587500.
- [110] Duchenne, Olivier et al. “A Tensor-Based Algorithm for High-Order Graph Matching”. In: *IEEE Transactions on Pattern Analysis and Machine Intelligence* 33.12 (2011), pp. 2383–2395. doi: 10.1109/TPAMI.2011.110.
- [111] Zhu, Hu et al. “Elastic Net Constraint-Based Tensor Model for High-Order Graph Matching”. In: *IEEE Transactions on Cybernetics* 51.8 (2021), pp. 4062–4074. doi: 10.1109/TCYB.2019.2936176.
- [112] Müller, Meinard. *Information Retrieval for Music and Motion*. Jan. 2007. isbn: 978-3-540-74047-6. doi: 10.1007/978-3-540-74048-3.
- [113] Fan, Jingfan et al. “Convex hull indexed Gaussian mixture model (CH-GMM) for 3D point set registration”. In: *Pattern Recognition* 59 (2016). Compositional Models and Structured Learning for Visual Recognition, pp. 126–141. issn: 0031-3203. doi: <https://doi.org/10.1016/j.patcog.2016.02.023>. url: <https://www.sciencedirect.com/science/article/pii/S0031320316000947>.
- [114] Evangelidis, Georgios D. et al. “A Generative Model for the Joint Registration of Multiple Point Sets”. In: *Computer Vision – ECCV 2014*. Ed. by Fleet, David et al. Cham: Springer International Publishing, 2014, pp. 109–122. isbn: 978-3-319-10584-0.

- [115] Yuan, Wentao et al. *DeepGMR: Learning Latent Gaussian Mixture Models for Registration*. 2020. arXiv: 2008.09088 [cs.CV].
- [116] Yang, Heng, Shi, Jingnan, and Carlone, Luca. “TEASER: Fast and Certifiable Point Cloud Registration”. In: *IEEE Transactions on Robotics* 37.2 (2021), pp. 314–333. doi: 10.1109/TRO.2020.3033695.
- [117] Sun, Lei. *IRON: Invariant-based Highly Robust Point Cloud Registration*. 2021. arXiv: 2103.04357 [cs.CV].
- [118] Briales, Jesus and Gonzalez-Jimenez, Javier. “Convex Global 3D Registration With Lagrangian Duality”. In: *Proceedings of the IEEE Conference on Computer Vision and Pattern Recognition (CVPR)*. July 2017.
- [119] Yang, Heng et al. “Graduated Non-Convexity for Robust Spatial Perception: From Non-Minimal Solvers to Global Outlier Rejection”. In: *IEEE Robotics and Automation Letters* 5.2 (Apr. 2020), pp. 1127–1134. doi: 10.1109/LRA.2020.2965893. URL: <https://doi.org/10.1109/LRA.2020.2965893>.
- [120] LaValle, Steven M. *Planning Algorithms*. Cambridge University Press, 2006. doi: 10.1017/CBO9780511546877.
- [121] Li, Yanbo, Littlefield, Zakary, and Bekris, Kostas E. *Asymptotically Optimal Sampling-based Kinodynamic Planning*. 2016. arXiv: 1407.2896 [cs.RO].
- [122] Li, Linjun et al. “MPC-MPNet: Model-Predictive Motion Planning Networks for Fast, Near-Optimal Planning under Kinodynamic Constraints”. In: *CoRR* abs/2101.06798 (2021). arXiv: 2101.06798. URL: <https://arxiv.org/abs/2101.06798>.
- [123] Khandate, Gagan et al. *Sampling-based Exploration for Reinforcement Learning of Dexterous Manipulation*. 2023. arXiv: 2303.03486 [cs.RO].
- [124] Qin, Yuzhe et al. *DexMV: Imitation Learning for Dexterous Manipulation from Human Videos*. 2021.
- [125] Salisbury, J. Kenneth and Craig, John J. “Articulated Hands: Force Control and Kinematic Issues”. In: *The International Journal of Robotics Research* 1.1 (1982), pp. 4–17. doi: 10.1177/027836498200100102. eprint: <https://doi.org/10.1177/027836498200100102>. URL: <https://doi.org/10.1177/027836498200100102>.
- [126] Jonker, Ben, Waiboer, Rob, and Aarts, Ronald. “Modelling of joint friction in robotic manipulators with gear transmissions”. In: Jan. 2007, pp. 221–243. ISBN: 10-1-4020-5683-4.
- [127] Lynch, Kevin M and Park, Frank C. *Modern Robotics: Mechanics, Planning, and Control*. English (US). Cambridge Univeristy Press, 2017. ISBN: 978-1107156302.
- [128] Ghaednia, Hamed et al. “Contact Mechanics”. In: Nov. 2013, pp. 93–140. ISBN: 978-1-4614-1944-0. doi: 10.1007/978-1-4614-1945-7_3.
- [129] Gazebo. *Control Description*. URL: %5Curl%7Bhttps://classic.gazebosim.org/tutorials?tut=plugins_hello_world&cat=write_plugin%7D.
- [130] Vries, Maarten de. *Switch to libb64 for base64 encoding/decoding*. URL: %5Curl%7Bhttps://github.com/ros/ros_comm/pull/1046%7D.
- [131] Görner, Michael and Ruppel, Philipp. *biotac_gazebo_plugin*. Version 1.0.0. URL: https://github.com/TAMS-Group/biotac_gazebo_plugin.
- [132] Melbye Staven, Victor. *biotac_sim_plugin*. Version 1.0.0. URL: https://github.com/vmstavens/biotac_sim_plugin.
- [133] Görner, Michael and Ruppel, Philipp. *Biotac Single Contact Response*. URL: %5Curl%7Bhttps://tams.informatik.uni-hamburg.de/research/datasets/index.php#biotac_single_contact_response%7D.

- [134] E-MOTION. *ATI: 6-Axis Force and Torque Sensor (Nano17 Series) 9105-TW-NANO17-E-1.8*. URL: %5Curl%7Bhttps://www.e-motionsupply.com/product_p/9105-tw-nano17-e-1.8.htm%7D.
- [135] Olson, Edwin. “AprilTag: A robust and flexible visual fiducial system”. In: *2011 IEEE International Conference on Robotics and Automation*. 2011, pp. 3400–3407. doi: [10.1109/ICRA.2011.5979561](https://doi.org/10.1109/ICRA.2011.5979561).
- [136] University, Stanford. *The Stanford 3D Scanning Repository*. <http://graphics.stanford.edu/data/3Dscanrep/>.
- [137] Carlone, Luca et al. *Lagrangian Duality in 3D SLAM: Verification Techniques and Optimal Solutions*. 2015. arXiv: [1506.00746](https://arxiv.org/abs/1506.00746) [cs.RO].
- [138] Carlone, Luca et al. “Planar Pose Graph Optimization: Duality, Optimal Solutions, and Verification”. In: *IEEE Transactions on Robotics* 32 (May 2016), pp. 1–21. doi: [10.1109/TRO.2016.2544304](https://doi.org/10.1109/TRO.2016.2544304).
- [139] Nesterov, Yuri, Wolkowicz, Henry, and Ye, Yinyu. “Semidefinite Programming Relaxations of Nonconvex Quadratic Optimization”. In: *Handbook of Semidefinite Programming: Theory, Algorithms, and Applications*. Ed. by Wolkowicz, Henry, Saigal, Romesh, and Vandenberghe, Lieven. Boston, MA: Springer US, 2000, pp. 361–419. ISBN: 978-1-4615-4381-7. doi: [10.1007/978-1-4615-4381-7_13](https://doi.org/10.1007/978-1-4615-4381-7_13). URL: https://doi.org/10.1007/978-1-4615-4381-7_13.
- [140] Rajeswaran, Aravind et al. “Learning complex dexterous manipulation with deep reinforcement learning and demonstrations”. In: *arXiv preprint arXiv:1709.10087* (2017).
- [141] Todorov, Emanuel, Erez, Tom, and Tassa, Yuval. “MuJoCo: A physics engine for model-based control”. In: *2012 IEEE/RSJ International Conference on Intelligent Robots and Systems*. IEEE. 2012, pp. 5026–5033. doi: [10.1109/IROS.2012.6386109](https://doi.org/10.1109/IROS.2012.6386109).
- [142] Baird III, Leemon C. *Advantage updating*. Tech. rep. WRIGHT LAB WRIGHT-PATTERSON AFB OH, 1993.
- [143] Çalli, Berk et al. “Benchmarking in Manipulation Research: The YCB Object and Model Set and Benchmarking Protocols”. In: *CoRR* abs/1502.03143 (2015). arXiv: [1502.03143](https://arxiv.org/abs/1502.03143). URL: <http://arxiv.org/abs/1502.03143>.
- [144] Romero, Javier, Tzionas, Dimitrios, and Black, Michael J. “Embodied hands”. In: *ACM Transactions on Graphics* 36.6 (Nov. 2017), pp. 1–17. doi: [10.1145/3130800.3130883](https://doi.org/10.1145/3130800.3130883). URL: <https://doi.org/10.1145/3130800.3130883>.
- [145] Shah, Khaled et al. “Combinatorial Color Space Models for Skin Detection in Sub-continental Human Images”. In: Nov. 2009, pp. 532–542. ISBN: 978-3-642-05035-0. doi: [10.1007/978-3-642-05036-7_50](https://doi.org/10.1007/978-3-642-05036-7_50).
- [146] Todorov, Emanuel and Jordan, Michael I. “Smoothness Maximization Along a Predefined Path Accurately Predicts the Speed Profiles of Complex Arm Movements”. In: *Journal of Neurophysiology* 80.2 (1998). PMID: 9705462, pp. 696–714. doi: [10.1152/jn.1998.80.2.696](https://doi.org/10.1152/jn.1998.80.2.696). eprint: <https://doi.org/10.1152/jn.1998.80.2.696>. URL: <https://doi.org/10.1152/jn.1998.80.2.696>.
- [147] Ranges. https://shadow-robot-company-dexterous-hand.readthedocs-hosted.com/en/latest/user_guide/md_ranges.html. Accessed: 2023-04-26.
- [148] Ngeo, Jimson, Tamei, Tomoya, and Shibata, Tomohiro. “Continuous and simultaneous estimation of finger kinematics using inputs from an EMG-to-muscle activation model”. In: *Journal of neuroengineering and rehabilitation* 11 (Aug. 2014), p. 122. doi: [10.1186/1743-0003-11-122](https://doi.org/10.1186/1743-0003-11-122).
- [149] Palmer, A K et al. “Functional wrist motion: a biomechanical study”. en. In: *J Hand Surg Am* 10.1 (Jan. 1985), pp. 39–46.

- [150] *Finger*. https://shadow-robot-company-dexterous-hand.readthedocs-hosted.com/en/latest/user_guide/md_finger.html. Accessed: 2023-04-26.
- [151] Mavrogiannis, Christoforos. “Grasp Synthesis Algorithms for Multifingered Robot Hands”. PhD thesis. Mar. 2013.
- [152] *Kinematics*. https://shadow-robot-company-dexterous-hand.readthedocs-hosted.com/en/latest/user_guide/md_kinematics.html. Accessed: 2023-04-26.

Appendix A

Shadow Dexterous Hand - Technical Specifications

Table A.1 shows the ROM for the SDH and Table A.2 show the ROM for a human hand. The shorthand abbreviations used in these tables can be seen listed in Table A.3. The joints are numbered from fingertip to base and thus FF1 refers to the first joint after the fingertip on the first finger i.e. the index finger.

ROM - SDH					
Joint(s)	Min deg	Max deg	Min rad	Max rad	Notes
FF1, MF1, RF1, LF1	0	90	0	1.571	Coupled
FF2, MF2, RF2, LF2	0	90	0	1.571	
FF3, MF3, RF3, LF3	-15	90	-0.262	1.571	
FF4, MF4, RF4, LF4	-20	20	-0.349	0.349	
LF5	0	45	0	0.785	
TH1	-15	90	-0.262	1.571	
TH2	-40	40	-0.698	0.698	
TH3	-12	12	-0.209	0.209	
TH4	0	70	0	1.222	
TH5	-60	60	-1.047	1.047	
WR1	-40	28	-0.698	0.489	
WR2	-28	10	-0.489	0.174	

Table A.1: The ranges of motion for each joint in the SDH [147].

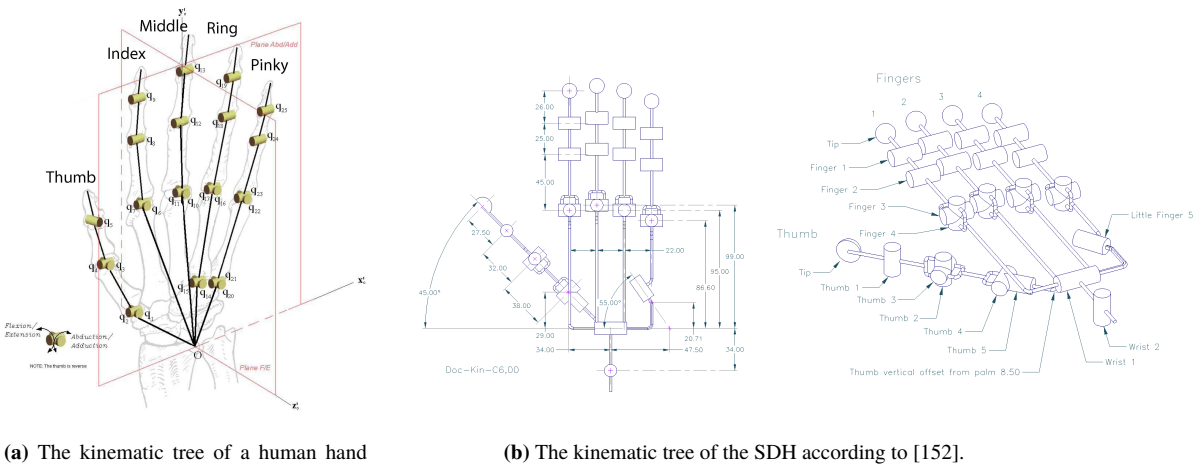
ROM - Human Hand					
Joint(s)	Min deg	Max deg	Min rad	Max rad	Latin Name
TH1	-15	80	-0.262	1.396	Interphalangeal (IP)
TH2 + TH3	-10	55	-0.175	0.96	Metacarpophalangeal (MCP)
TH4 + TH5	-10	55	-0.175	0.96	Carpometacarpal (CMC)
FF1, MF1, RF1, LF1	0	80	0.0	1.396	Distal interphalangeal (DIP)
FF2, MF2, RF2, LF2	0	100	0.0	1.745	Proximal interphalangeal (PIP)
FF3, MF3, RF3, LF3	-45	90	-0.785	1.571	Metacarpophalangeal (MCP)
WR1	-80	80	-1.396	1.396	Radiocarpal
WR2	-28	20	-0.489	0.349	Radiocarpal

Table A.2: The theoretical ROM for each finger joint in human hand [148] and found ROM for the wrist joints [149].

To compare the kinematic structure of the Shadow Dexterous Hand and a human hand, see Fig. A.1.

Joint Name Abbreviation	
Abbreviation	Full Name
FF	First Finger
MF	Middle Finger
RF	Ring Finger
LF	Little Finger
WR	Wrist

Table A.3: The abbreviations used to reference [150].



Appendix B

Tactile Perception - Simulated Electrode Activations

Below three figures are found showing the DL model inputs and outputs as described in 5.1 Methods. Fig. B.1 shows the input and output graphs for the case when the SDH index finger in contact with an edge. Fig. B.2 shows the same graph but for contact with a smooth surface and Fig. B.3 shows the graph but for contact with a corner.

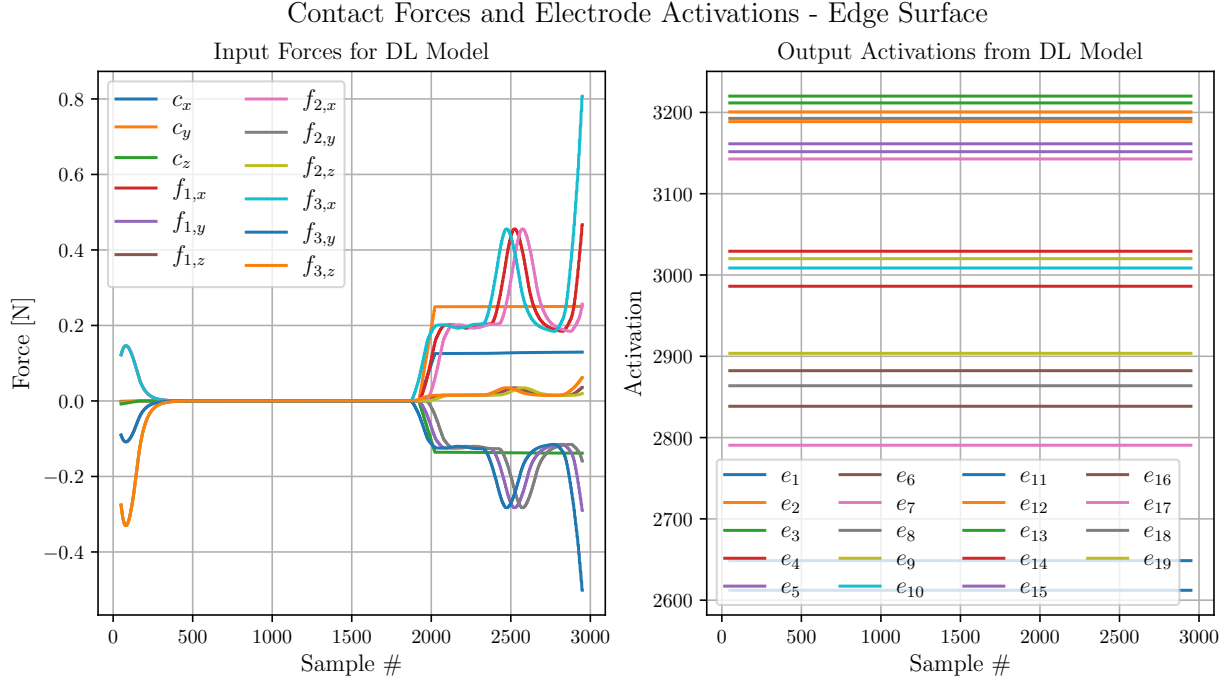


Fig. B.1: he simulated tactile electrode activations when the simulated Shadow Dexterous hand's index finger is in contact with an edge.

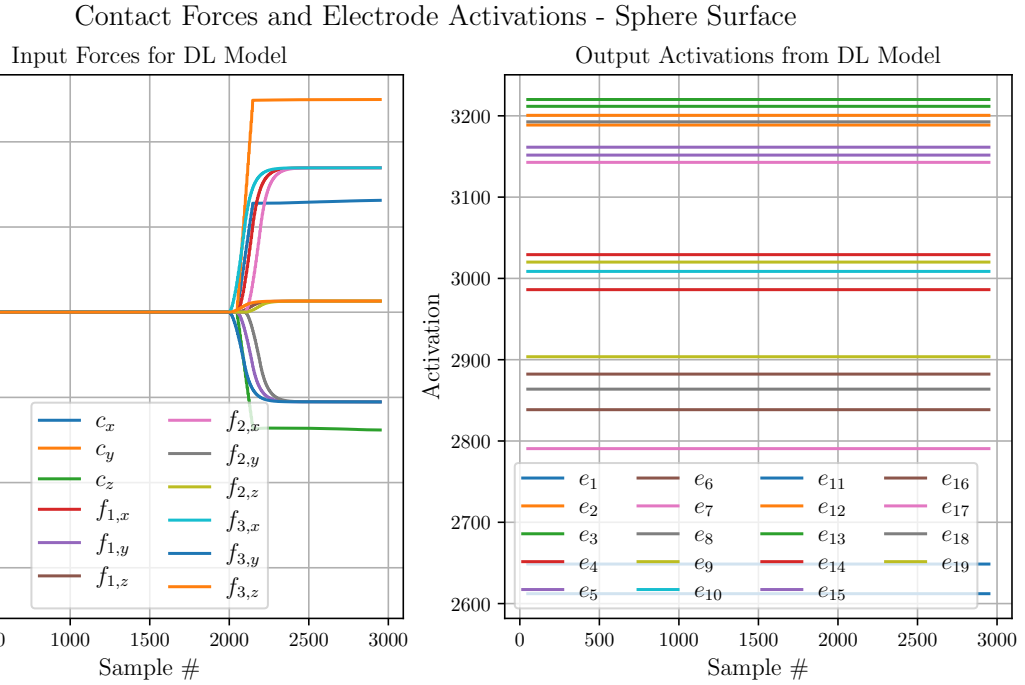


Fig. B.2: The simulated tactile electrode activations when the simulated Shadow Dexterous hand's index finger is in contact with a smooth surface.

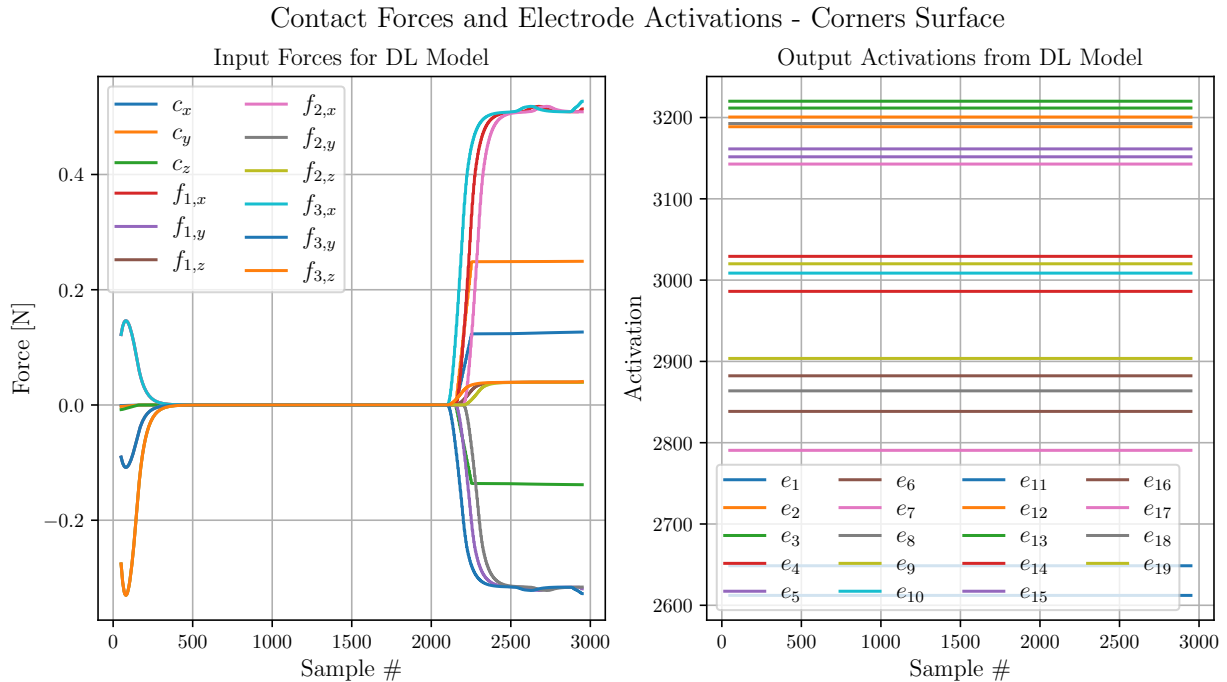


Fig. B.3: The simulated tactile electrode activations when the simulated Shadow Dexterous hand's index finger is in contact with a corner.

Appendix C

Pose Estimation Weight Convergence

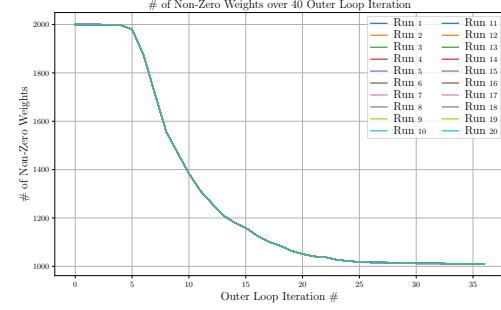
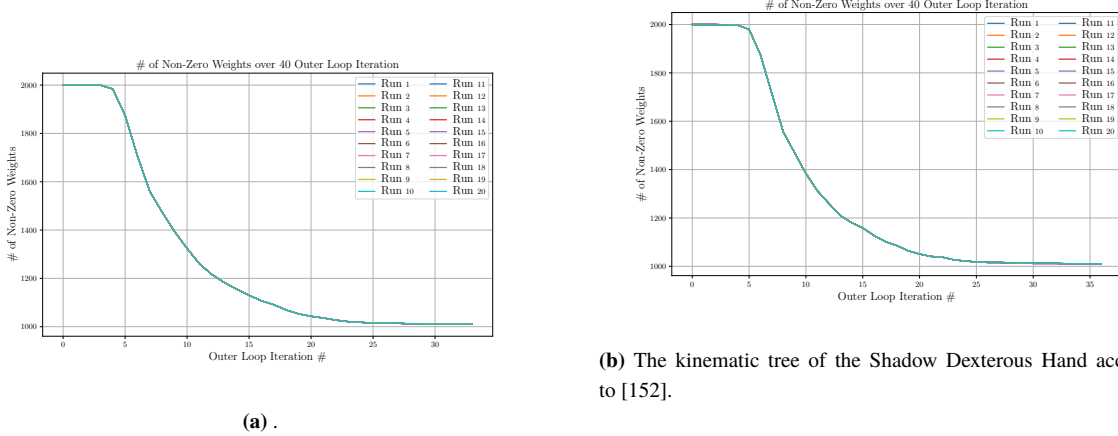


Fig. C.1: The kinematic trees of a human hand and the Shadow Dexterous hand.

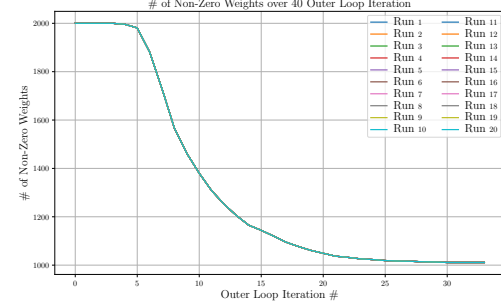
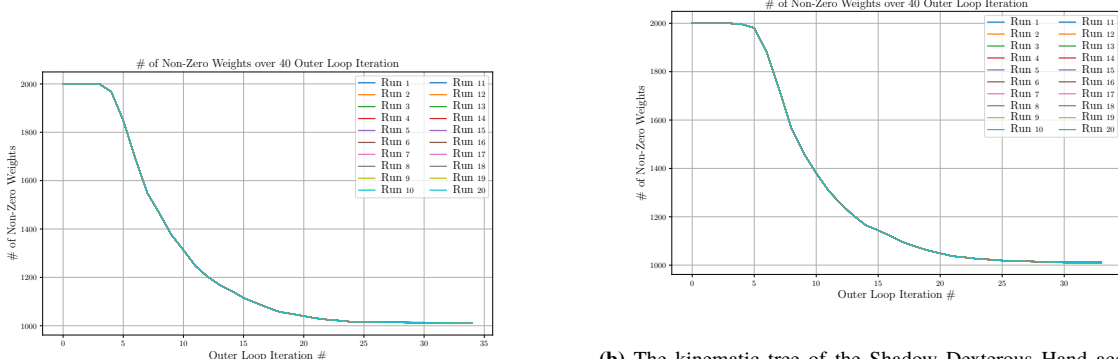
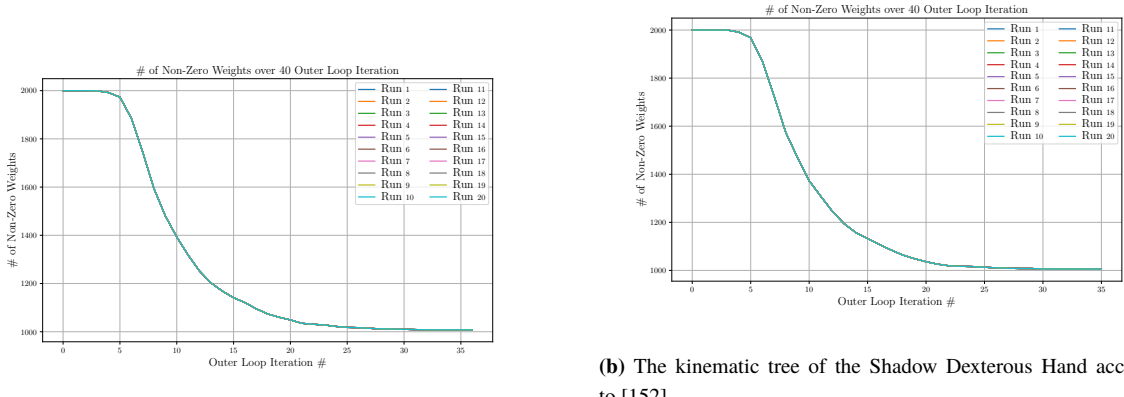
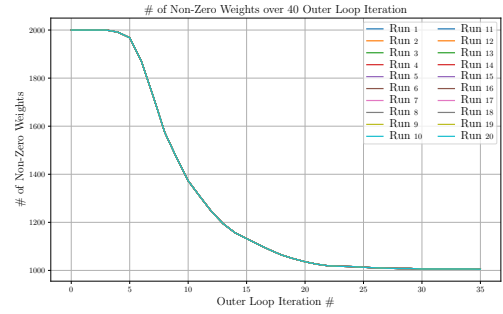


Fig. C.2: The kinematic trees of a human hand and the Shadow Dexterous hand.

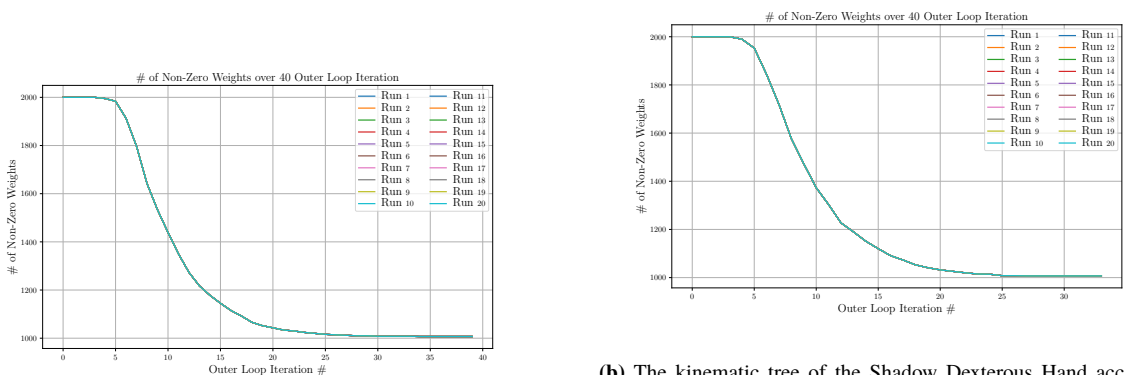


(a) The kinematic tree of a human hand according to [151].

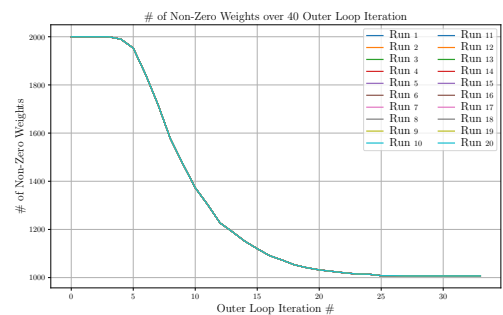


(b) The kinematic tree of the Shadow Dexterous Hand according to [152].

Fig. C.3: The kinematic trees of a human hand and the Shadow Dexterous hand.



(a) The kinematic tree of a human hand according to [151].



(b) The kinematic tree of the Shadow Dexterous Hand according to [152].

Fig. C.4: The kinematic trees of a human hand and the Shadow Dexterous hand.

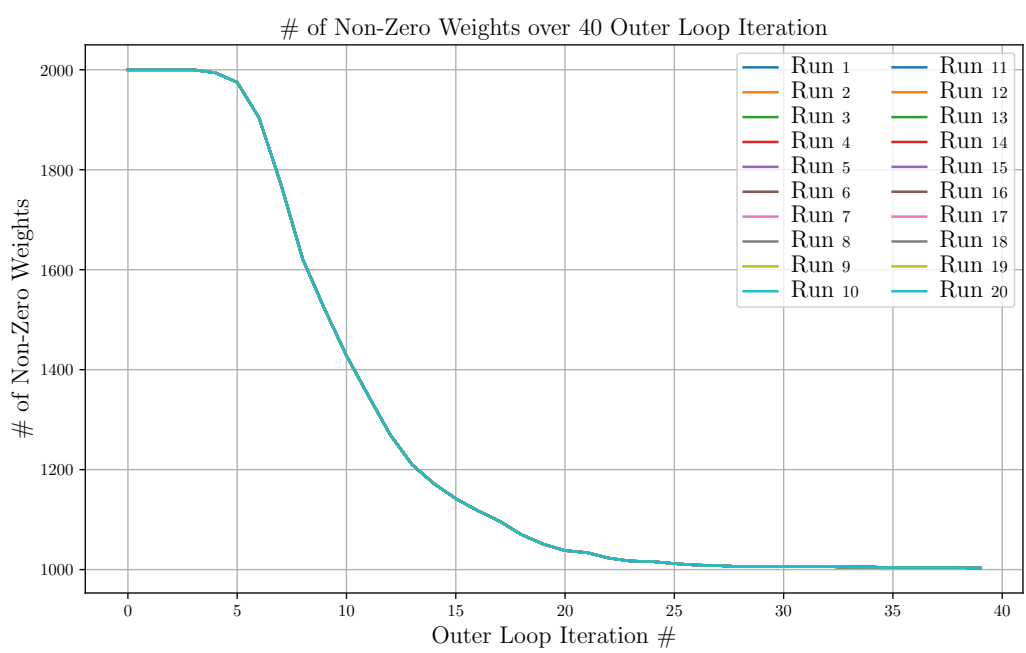


Fig. C.5: The simulated tactile electrode activations when the simulated Shadow Dexterous hand's index finger is in contact with a corner.